

**CHARACTERIZATIONS OF TRANSITION METALS DOPED  $\text{SnO}_2$   
NANOPARTICLE PREPARED BY AUTOCOMBUSTION TECHNIQUE**

**MALEE PRAJUABSUK**

**A THESIS SUBMITTED IN PARTIAL FULFILLMENT OF THE REQUIREMENTS**

**FOR THE DEGREE OF MASTER OF SCIENCE**

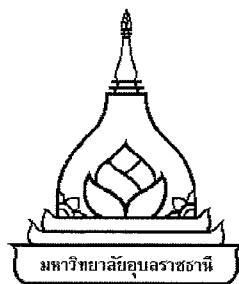
**MAJOR IN CHEMISTRY**

**FACULTY OF SCIENCE**

**UBON RAJATHANEE UNIVERSITY**

**YEAR 2008**

**COPYRIGHT OF UBON RAJATHANEE UNIVERSITY**



**THESIS APPROVAL**

**UBON RAJATHANEE UNIVERSITY**

**MASTER OF SCIENCE**

**MAJOR IN CHEMISTRY FACULTY OF SCIENCE**

**TITLE** CHARACTERIZATIONS OF TRANSITION METALS DOPED  $\text{SnO}_2$   
NANOPARTICLE PREPARED BY AUTOCOMBUSTION TECHNIQUE

**NAME** MISS MALEE PRAJUABSUK

**THIS THESIS HAS BEEN ACCEPTED BY**

.....  
(DR.TAWEESAK SUDYOADSUK) CHAIR

.....  
(DR.SUPAKORN BOONYUEN) COMMITTEE

.....  
(ASST.PROF.DR.JUTHAMAS JITCHAROEN) COMMITTEE

.....  
(ASST.PROF.DR.SAYANT SAENG SUWAN) COMMITTEE

.....  
(ASST.PROF.DR.JANPEN INTARAPRASERT) DEAN

**APPROVAL BY UBON RAJATHANEE UNIVERSITY**

.....  
(ASST.PROF.DR.UTITH INPRASIT)

VICE PRESIDENT FOR ACADEMIC AFFAIRS

FOR THE PRESIDENT OF UBON RAJATHANEE UNIVERSITY

ACADEMIC YEAR 2008

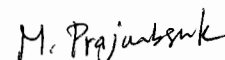
## ACKNOWLEDGEMENT

I would like to begin by expressing my sincere gratitude and grate appreciation to my advisor Dr. Taweesak Sudyoadsuk. His understanding, guidance, encouragement and support during the pursuit of my master degree are greatly appreciated. I have been deeply impressed by his wisdom, insight, knowledge and enthusiasm.

I am grateful to Dr. Supakorn Boonyuen, Asst. Prof. Dr. Juthamas Jitcharoen and Asst. Prof. Dr. Sayant Saengsuwan for their helpful suggestions, comments of completion of this thesis and taking time from their busy schedules to serve on my committee.

I am also thankful to Department of Chemistry, Faculty of Science, Ubon Rajathanee University and staff for providing laboratory facilities. In addition, I would like to thank to Asst. Prof. Dr. Sujitra Youngmee from Department of Chemistry, Faculty of Science, Khon Kaen University and her assistant researcher for educating and entertaining me during our magnetic discussions. Thanks also to Department of Biological Science, Faculty of Science, Ubon Rajathanee University and Mrs. Pathoomthip Ponyon for taking me everything that I know about scanning electron microscopy. Moreover, I express my gratitude to Mr. Wuttisak Prachamorn from Department of Physics, Faculty of Science, Ubon Rajathanee University for administrative help, educating and training me on X-ray Powder Diffractometer.

I would like to thank my friends and my co-workers for making graduate school an exciting and memorable experience. Finally, I am deeply grateful to my parents and all of my aunts and uncles for their love, kindness, encouragement and support throughout my life and educational career.



(Miss Malee Prajuabsuk)

Researcher

## บทคัดย่อ

ชื่อเรื่อง : การศึกษาสมบัติของสารประกอบอนุภาคนาโนทินออกไซด์ ที่มีโลหะทรานสิชันเป็นตัวเติม เตรียมโดยเทคนิคอโตคอมบัสชัน

โดย : มาลี ประจวบสุข

ชื่อปริญญา : ปริญญาวิทยาศาสตรมหาบัณฑิต

สาขาวิชา : เคมี

ประธานกรรมการที่ปรึกษา : ดร.ทวีศักดิ์ สุธยอดสุข

ศัพท์สำคัญ : สารกึ่งตัวนำแม่เหล็กแบบเจือจาง / อโตคอมบัสชัน / โลหะทรานสิชัน / ทินออกไซด์ / อนุภาคนาโน

ได้เตรียมอนุภาคนาโน  $\text{Sn}_{1-x}\text{TM}_x\text{O}_{2.8}$  เมื่อ  $\text{TM} = \text{Cr}$  และ  $\text{Co}$  โดย  $x \leq 0.015$  และ  $\text{Fe}$  โดย  $x \leq 0.300$  โดยเทคนิคอโตคอมบัสชัน ผลจากการเลี้ยวเบนรังสีเอกซ์แสดงให้เห็นว่ามีโครงสร้างผลึกเป็นแบบเพระโกนออร์โธไทล์ มีขนาดอนุภาคเฉลี่ยอยู่ในช่วง 5 - 20 นาโนเมตร และจากสเปกตรัมการสะท้อนแสงแสดงแถบการดูดกลืนของการทรานสิชัน  $d-d$  ที่ยืนยันได้ว่าการแทนที่ของไอออนโลหะทรานสิชัน มีค่าพลังงานแถบช่องว่างอยู่ในช่วง 3.2 - 3.8 อิเล็กตรอนโวลต์ อนุภาคนาโน  $\text{Sn}_{1-x}\text{TM}_x\text{O}_{2.8}$  ที่  $x \leq 0.015$  แสดงสมบัติเฟอร์โรแมกเนติกอย่างอ่อนที่อุณหภูมิห้อง ขณะที่แสดงสมบัติซูเปอร์พาราแมกเนติกเมื่อตัวเติม  $\text{Fe}$  มีปริมาณสูง ( $0.100 \leq x \leq 0.300$ )

**ABSTRACT**

TITLE : CHARACTERIZATIONS OF TRANSITION METALS DOPED  $\text{SnO}_2$   
NANOPARTICLE PREPARED BY AUTOCOMBUSTION TECHNIQUE  
BY : MALEE PRAJUABSUK  
DEGREE : MASTER OF SCIENCE  
MAJOR : CHEMISTRY  
CHAIR : TAWEESEK SUDYOADSUK, Ph.D.  
KEYWORDS : DILUTED MAGNETIC SEMICONDUCTOR / AUTOCOMBUSTION /  
TRANSITION METAL / TIN OXIDE / NANOPRTICLES

The  $\text{Sn}_{1-x}\text{TM}_x\text{O}_{2.8}$  nanoparticles samples (TM = Cr and Co with  $x \leq 0.015$  and Fe with  $x \leq 0.300$ ) were prepared by the autocombustion technique. The XRD patterns of all samples exhibit a single tetragonal rutile phase without any trace of an impurity phase. The particle size is in the range of 5 - 20 nm. The diffuse reflectance spectra show the  $d-d$  band transition of the substituted transition metal ions. The band gap energies are in the range of 3.2 - 3.8 eV. The  $\text{Sn}_{1-x}\text{TM}_x\text{O}_{2.8}$  nanoparticles samples with  $x \leq 0.015$  exhibit the weak ferromagnetic-like behavior at room temperature, while the high level dope Fe ( $0.100 \leq x \leq 0.300$ ) the samples show a superparamagnetic characteristic.

## CONTENTS

|  | Page        |
|--|-------------|
| <b>ACKNOWLEDGEMENT</b>                           | <b>I</b>    |
| <b>ABSTRACT IN THAI</b>                          | <b>II</b>   |
| <b>ABSTRACT IN ENGLISH</b>                       | <b>III</b>  |
| <b>CONTENTS</b>                                  | <b>IV</b>   |
| <b>LIST OF TABLES</b>                            | <b>VII</b>  |
| <b>LIST OF FIGURES</b>                           | <b>VIII</b> |
| <b>ABBREVIATIONS</b>                             | <b>XII</b>  |
| <b>CHAPTER</b>                                   |             |
| <b>1 INTRODUCTION</b>                            | <b>1</b>    |
| <b>2 LITERATURE REVIEW</b>                       |             |
| 2.1 Diluted Magnetic Semiconductors (DMS)        | 4           |
| 2.2 Ferromagnetism in DMS                        | 5           |
| 2.3 DMS Materials                                | 8           |
| 2.3.1 DMS Based on $\text{TiO}_2$                | 8           |
| 2.3.2 DMS Based on $\text{ZnO}$                  | 11          |
| 2.3.3 DMS Based on $\text{SnO}_2$                | 13          |
| 2.4 The Autocombustion Technique                 | 15          |
| <b>3 EXPERIMENTAL TECHNIQUES</b>                 |             |
| 3.1 Schematic Diagram of the Experiment          | 19          |
| 3.2 Nanoparticles Preparation                    | 20          |
| 3.3 Physical Characterization                    | 21          |
| 3.3.1 X-ray Diffraction (XRD) Measurements       | 21          |
| 3.3.1.1 Structure Refinement                     | 21          |
| 3.3.1.2 Crystallite Size Determination           | 24          |
| 3.3.2 Optical Measurement                        | 27          |
| 3.3.2.1 Calculation of Band Gap Energy ( $E_g$ ) | 27          |
| 3.3.3 Microstructure                             | 28          |
| 3.4 Magnetic Measurement                         | 28          |

## CONTENTS (CONTINUED)

|   | Page |
|---|------|
| <b>4 RESULTS AND DISCUSSION</b>   |      |
| 4.1 Chromium-doped Tin Oxide ( $\text{Sn}_{1-x}\text{Cr}_x\text{O}_{2.8}$ ) | 30   |
| 4.1.1 X-ray Diffraction Studies   | 30   |
| 4.1.2 The Rietveld Refinement   | 32   |
| 4.1.3 Crystallite Sizes   | 35   |
| 4.1.4 Microstructure  | 37   |
| 4.1.5 Optical Properties  | 39   |
| 4.1.6 Magnetic Measurement  | 42   |
| 4.2 Cobalt-doped Tin Oxide ( $\text{Sn}_{1-x}\text{Co}_x\text{O}_{2.8}$ )   | 49   |
| 4.2.1 X-ray Diffraction Studies   | 49   |
| 4.2.2 The Rietveld Refinement   | 51   |
| 4.2.3 Crystallite Sizes   | 55   |
| 4.2.4 Microstructure  | 56   |
| 4.2.5 Optical Properties  | 57   |
| 4.2.6 Magnetic Measurement  | 60   |
| 4.3 Iron-doped Tin Oxide ( $\text{Sn}_{1-x}\text{Fe}_x\text{O}_{2.8}$ )     | 64   |
| 4.3.1 X-ray Diffraction Studies   | 64   |
| 4.3.2 The Rietveld Refinement   | 66   |
| 4.3.3 Crystallite Sizes   | 70   |
| 4.3.4 Microstructure  | 73   |
| 4.3.5 Optical Properties  | 74   |
| 4.3.6 Magnetic Measurement  | 77   |
| <b>5 CONCLUSIONS</b>  | 83   |
| <b>REFERENCES</b>   | 86   |

## CONTENTS (CONTINUED)

|   | Page       |
|---|------------|
| <b>APPENDICES</b>   | <b>96</b>  |
| <b>APPENDIX</b>   |            |
| A X-ray Diffraction patterns  | 97         |
| B Atomic Scattering Factors   | 100        |
| C The Database of Some Ionic Radii  | 102        |
| D The Crystallite Sizes Calculations for $\text{Sn}_{0.700}\text{Fe}_{0.300}\text{O}_{2.8}$ calcined at 973 K | 104        |
| E Crystallite sizes calculated by Scherrer's equation and Williamson-Hall Plot<br>method                      | 106        |
| F Kubelka-Munk Spectra  | 108        |
| G X-ray Diffractograms of $\text{Sn}_{1-x}\text{TM}_x\text{O}_{2.8}$ from Rietveld Refinement                 | 113        |
| H Magnetic Data Analysis  | 125        |
| I The Full Width at Half Maximum (FWHM) of the XRD Plane (110)  | 127        |
| <b>VITAE</b>  | <b>131</b> |



## LIST OF TABLES

| Table |   | Page |
|-------|---|------|
| 2.1   | List of transition metals (1 <sup>st</sup> series) doped TiO <sub>2</sub> -based DMS recently reported.   | 10   |
| 2.2   | List of transition metals (1 <sup>st</sup> series) doped ZnO-based DMS recently reported.   | 12   |
| 4.1   | The Rietveld refinement crystallographic data of the Sn <sub>1-x</sub> Cr <sub>x</sub> O <sub>2-δ</sub> (x = 0.005, 0.010 and 0.015) samples calcined at 773, 873 and 973 K. The space group P42/mnm was used for all samples. Sn/Cr was occupied at (0, 0, 0) and O <sup>2-</sup> was occupied at (x, y, 0) while x was equal to y. The numbers in the parenthesis were estimated standard deviations to the last significant digit. | 34   |
| 4.2   | Crystallite sizes of the Sn <sub>1-x</sub> Cr <sub>x</sub> O <sub>2-δ</sub> samples obtained from TEM images.   | 38   |
| 4.3   | Band Gap Energy, $E_g$ (eV) of the Sn <sub>1-x</sub> Cr <sub>x</sub> O <sub>2-δ</sub> samples.  | 41   |
| 4.4   | The Rietveld refinement crystallographic data of the Sn <sub>1-x</sub> Co <sub>x</sub> O <sub>2-δ</sub> (x = 0.005, 0.010 and 0.015) samples calcined at 773, 873 and 973 K. The space group P42/mnm was used for all samples. Sn/Cr was occupied at (0, 0, 0) and O <sup>2-</sup> was occupied at (x, y, 0) while x was equal to y. The numbers in the parenthesis were estimated standard deviations to the last significant digit. | 53   |
| 4.5   | Band Gap Energy, $E_g$ (eV) of the Sn <sub>1-x</sub> Co <sub>x</sub> O <sub>2-δ</sub> samples.  | 59   |
| 4.6   | The Rietveld refinement crystallographic data of the Sn <sub>1-x</sub> Fe <sub>x</sub> O <sub>2-δ</sub> (x = 0.005, 0.010 and 0.015) samples calcined at 773, 873 and 973 K. The space group P42/mnm was used for all samples. Sn/Cr was occupied at (0, 0, 0) and O <sup>2-</sup> was occupied at (x, y, 0) while x was equal to y. The numbers in the parenthesis were estimated standard deviations to the last significant digit. | 68   |
| 4.7   | The Rietveld refinement crystallographic data of the Sn <sub>1-x</sub> Fe <sub>x</sub> O <sub>2-δ</sub> (x = 0.100, 0.200 and 0.300) samples calcined at 773, 873 and 973 K. The space group P42/mnm was used for all samples. Sn/Cr was occupied at (0, 0, 0) and O <sup>2-</sup> was occupied at (x, y, 0) while x was equal to y. The numbers in the parenthesis were estimated standard deviations to the last significant digit. | 69   |
| 4.8   | Band Gap Energy, $E_g$ (eV) of the Sn <sub>1-x</sub> Fe <sub>x</sub> O <sub>2-δ</sub> samples.  | 75   |

## LIST OF FIGURES

| Figure  | Page |
|---|------|
| 2.1 Schematic illustration of (a) a magnetic semiconductor, which has a periodic array of a magnetic element, (b) a diluted magnetic semiconductor (DMS), an alloy between a nonmagnetic semiconductor and a magnetic element and (c) a non-magnetic semiconductor, which contains no magnetic ions.  | 5    |
| 2.2 The magnetization direction of the single domain.   | 6    |
| 2.3 The relationship between the magnetization ( $M$ ) and the magnetic field ( $H$ ) hysteresis loop.  | 7    |
| 3.1 Schematic diagram of the experimental process in this study.  | 19   |
| 3.2 A typical hysteresis loop for ferromagnetic materials.  | 29   |
| 4.1 X-ray Diffraction patterns of the $\text{Sn}_{1-x}\text{Cr}_x\text{O}_{2-\delta}$ ( $x \leq 0.015$ ) samples calcined at 773 K.   | 31   |
| 4.2 Changes in the plane (110) of the $\text{Sn}_{1-x}\text{Cr}_x\text{O}_{2-\delta}$ samples calcined at 773, 873 and 973 K.   | 31   |
| 4.3 X-ray Diffraction patterns of the $\text{Sn}_{0.985}\text{Cr}_{0.015}\text{O}_{2-\delta}$ samples with the variation of calcined temperatures.  | 32   |
| 4.4 X-ray diffractograms of (a) $\text{Sn}_{0.995}\text{Cr}_{0.005}\text{O}_{2-\delta}$ (b) $\text{Sn}_{0.990}\text{Cr}_{0.010}\text{O}_{2-\delta}$ and (c) $\text{Sn}_{0.985}\text{Cr}_{0.015}\text{O}_{2-\delta}$ calcined at 973 K. Data points were indicated by solid cycles, while the calculated patterns were shown as a continuous line. The positions of the reflections were indicated with the vertical lines below the patterns. | 33   |
| 4.5 Crystallite sizes of the $\text{Sn}_{1-x}\text{Cr}_x\text{O}_{2-\delta}$ ( $x \leq 0.015$ ) samples with the various calcinations temperatures calculated by Scherrer's equation.   | 36   |
| 4.6 Crystallite sizes of the $\text{Sn}_{1-x}\text{Cr}_x\text{O}_{2-\delta}$ ( $x \leq 0.015$ ) samples with the various calcinations temperatures calculated by Williamson-Hall Plot method.   | 37   |
| 4.7 (a) TEM images of $\text{Sn}_{0.995}\text{Cr}_{0.015}\text{O}_{2-\delta}$ calcined at 973 K and (b) measured Cr nanoparticle size distribution corresponding to the TEM image shown in (a).   | 38   |
| 4.8 Kubelka-Munk spectra of the $\text{Sn}_{1-x}\text{Cr}_x\text{O}_{2-\delta}$ samples calcined at 873 K with the different Cr concentration.  | 39   |

## LIST OF FIGURES (CONTINUED)

| Figure   | Page |
|--|------|
| 4.9 Plot of $(f(R)h\nu)^2$ as a function of $h\nu$ for the $\text{Sn}_{1-x}\text{Cr}_x\text{O}_{2-\delta}$ samples calcined at 873 K with varying Cr concentration.  | 40   |
| 4.10 Band gap energy ( $E_g$ ) of the $\text{Sn}_{1-x}\text{Cr}_x\text{O}_{2-\delta}$ samples calcined at different temperatures and with varying Cr concentrations.   | 42   |
| 4.11 Magnetization ( $M$ ) at room temperature of $\text{Sn}_{0.995}\text{Cr}_{0.005}\text{O}_{2-\delta}$ calcined at 773, 873 and 973 K. Inset: diamagnetic background hysteresis loop.   | 43   |
| 4.12 Magnetization ( $M$ ) at room temperature of $\text{Sn}_{0.990}\text{Cr}_{0.010}\text{O}_{2-\delta}$ calcined at 773, 873 and 973 K.  | 45   |
| 4.13 Magnetization ( $M$ ) at room temperature of $\text{Sn}_{0.985}\text{Cr}_{0.015}\text{O}_{2-\delta}$ calcined at 773, 873 and 973 K.  | 46   |
| 4.14 Magnetization ( $M$ ) at room temperature of the $\text{Sn}_{1-x}\text{Cr}_x\text{O}_{2-\delta}$ ( $x \leq 0.015$ ) samples calcined at 873 K.  | 47   |
| 4.15 Magnetization ( $M$ ) at room temperature of the $\text{Sn}_{1-x}\text{Cr}_x\text{O}_{2-\delta}$ ( $x \leq 0.015$ ) samples calcined at 773 K. Inset: enlarge for $\text{Sn}_{0.990}\text{Cr}_{0.010}\text{O}_{2-\delta}$ calcined at 773 K.  | 48   |
| 4.16 Magnetization ( $M$ ) at room temperature of the $\text{Sn}_{1-x}\text{Cr}_x\text{O}_{2-\delta}$ ( $x \leq 0.015$ ) samples calcined at 973 K.  | 48   |
| 4.17 X-ray Diffraction patterns of the $\text{Sn}_{1-x}\text{Co}_x\text{O}_{2-\delta}$ ( $x \leq 0.015$ ) samples calcined at 873 K.   | 49   |
| 4.18 X-ray Diffraction patterns of the $\text{Sn}_{0.990}\text{Co}_{0.010}\text{O}_{2-\delta}$ samples with the variation of calcined temperatures.  | 50   |
| 4.19 Maximum intensities in the (110) of the $\text{Sn}_{1-x}\text{Co}_x\text{O}_{2-\delta}$ ( $x \leq 0.015$ ) samples calcined at 773, 873 and 973 K.  | 51   |
| 4.20 X-ray diffractograms of (a) $\text{Sn}_{0.995}\text{Co}_{0.005}\text{O}_{2-\delta}$ , (b) $\text{Sn}_{0.990}\text{Co}_{0.010}\text{O}_{2-\delta}$ and (c) $\text{Sn}_{0.985}\text{Co}_{0.015}\text{O}_{2-\delta}$ calcined at 973 K. Data points were indicated by solid cycles, while the calculated patterns were shown as a continuous line. The positions of the reflections were indicated with the vertical lines below the patterns. | 52   |
| 4.21 Crystallite sizes of the $\text{Sn}_{1-x}\text{Co}_x\text{O}_{2-\delta}$ ( $x \leq 0.015$ ) samples with the various calcinations temperatures calculated by Scherrer's equation.   | 55   |

# LIST OF FIGURES (CONTINUED)

| Figure |   | Page |
|--------|---|------|
| 4.22   | Crystallite sizes of the $\text{Sn}_{1-x}\text{Co}_x\text{O}_{2-\delta}$ ( $x \leq 0.015$ ) samples calcined at 773, 873 and 973 K calculated by Williamson-Hall Plot method.   | 56   |
| 4.23   | (a) TEM images of $\text{Sn}_{0.990}\text{Co}_{0.010}\text{O}_{2-\delta}$ calcined at 973 K and (b) measured Co nanoparticle size distribution corresponding to the TEM image shown in (a).   | 57   |
| 4.24   | Kubelka-Munk spectra of the $\text{Sn}_{1-x}\text{Co}_x\text{O}_{2-\delta}$ samples calcined at 873 K with the different Cr concentrations.   | 58   |
| 4.25   | Band gap energy ( $E_g$ ) of the $\text{Sn}_{1-x}\text{Co}_x\text{O}_{2-\delta}$ samples calcined at different temperatures and with varying Co concentrations.   | 59   |
| 4.26   | Magnetization ( $M$ ) at room temperature of $\text{Sn}_{0.995}\text{Co}_{0.005}\text{O}_{2-\delta}$ calcined at 773, 873 and 973 K.  | 60   |
| 4.27   | Magnetization ( $M$ ) at room temperature of $\text{Sn}_{0.990}\text{Co}_{0.010}\text{O}_{2-\delta}$ calcined at 873 and 973 K.   | 61   |
| 4.28   | Magnetization ( $M$ ) at room temperature of $\text{Sn}_{0.985}\text{Co}_{0.015}\text{O}_{2-\delta}$ calcined at 873 and 973 K.   | 62   |
| 4.29   | Magnetization ( $M$ ) at room temperature of the $\text{Sn}_{1-x}\text{Co}_x\text{O}_{2-\delta}$ ( $x \leq 0.015$ ) samples calcined at 973 K.  | 63   |
| 4.30   | X-ray Diffraction (XRD) patterns of the $\text{Sn}_{1-x}\text{Fe}_x\text{O}_{2-\delta}$ ( $x \leq 0.30$ ) samples calcined at 973 K.  | 64   |
| 4.31   | X-ray Diffraction patterns of the $\text{Sn}_{0.990}\text{Fe}_{0.010}\text{O}_{2-\delta}$ samples with the variation of calcined temperatures.  | 65   |
| 4.32   | Maximum intensities in the (110) of the $\text{Sn}_{1-x}\text{Cr}_x\text{O}_{2-\delta}$ samples ( $x \leq 0.30$ ) calcined at 773, 873 and 973 K.   | 66   |
| 4.33   | X-ray diffractograms of (a) $\text{Sn}_{0.990}\text{Fe}_{0.010}\text{O}_{2-\delta}$ , (b) $\text{Sn}_{0.900}\text{Fe}_{0.100}\text{O}_{2-\delta}$ and (c) $\text{Sn}_{0.800}\text{Fe}_{0.200}\text{O}_{2-\delta}$ calcined at 973 K. Data points were indicated by solid cycles, while the calculated patterns were shown as a continuous line. The positions of the reflections were indicated with the vertical lines below the patterns. | 67   |

# LIST OF FIGURES (CONTINUED)

| Figure |  | Page |
|--------|--|------|
| 4.34   | Crystallite sizes of the $\text{Sn}_{1-x}\text{Fe}_x\text{O}_{2-\delta}$ ( $x \leq 0.30$ ) samples calcined at 773, 873 and 973 K calculated by Scherrer's equation. Inset: enlarge for the $\text{Sn}_{1-x}\text{Fe}_x\text{O}_{2-\delta}$ ( $x \leq 0.015$ ) samples.  | 71   |
| 4.35   | Crystallite sizes of the $\text{Sn}_{1-x}\text{Fe}_x\text{O}_{2-\delta}$ ( $x \leq 0.30$ ) samples calcined at 773, 873 and 973 K calculated by Williamson-Hall plot. Inset: enlarge for the $\text{Sn}_{1-x}\text{Fe}_x\text{O}_{2-\delta}$ ( $x \leq 0.015$ ) samples. | 72   |
| 4.36   | (a) TEM images of $\text{Sn}_{0.900}\text{Fe}_{0.100}\text{O}_{2-\delta}$ calcined at 973 K and (b) measured Fe nanoparticle size distribution corresponding to the TEM image shown in (a).  | 73   |
| 4.37   | Kubelka-Munk spectra of the $\text{Sn}_{1-x}\text{Fe}_x\text{O}_{2-\delta}$ samples calcined at 873 with different Fe concentration.   | 74   |
| 4.38   | Band gap energy ( $E_g$ ) of the $\text{Sn}_{1-x}\text{Fe}_x\text{O}_{2-\delta}$ samples calcined at different temperatures and with varying Fe concentrations   | 76   |
| 4.39   | Magnetization ( $M$ ) at room temperature of $\text{Sn}_{0.995}\text{Fe}_{0.005}\text{O}_{2-\delta}$ calcined at 773, 873 and 973 K. Inset: enlarge the loops of $\text{Sn}_{0.995}\text{Fe}_{0.005}\text{O}_{2-\delta}$ calcined at 873 and 973 K.                      | 77   |
| 4.40   | Magnetization ( $M$ ) at room temperature of $\text{Sn}_{0.990}\text{Fe}_{0.010}\text{O}_{2-\delta}$ calcined at 773, 873 and 973 K.   | 78   |
| 4.41   | Magnetization ( $M$ ) at room temperature of $\text{Sn}_{0.985}\text{Fe}_{0.015}\text{O}_{2-\delta}$ calcined at 773, 873 and 973 K.   | 79   |
| 4.42   | Magnetization ( $M$ ) at room temperature of the $\text{Sn}_{1-x}\text{Fe}_x\text{O}_{2-\delta}$ ( $0.100 \leq x \leq 0.300$ ) samples calcined at 773 K. Inset: enlarge the loop of $\text{Sn}_{0.700}\text{Fe}_{0.300}\text{O}_{2-\delta}$ .                           | 80   |
| 4.43   | Magnetization ( $M$ ) at room temperature of the $\text{Sn}_{1-x}\text{Fe}_x\text{O}_{2-\delta}$ ( $0.100 \leq x \leq 0.300$ ) samples calcined at 873 K.  | 81   |
| 4.44   | Magnetization ( $M$ ) at room temperature of the $\text{Sn}_{1-x}\text{Fe}_x\text{O}_{2-\delta}$ ( $0.100 \leq x \leq 0.300$ ) samples calcined at 973 K.  | 82   |

## ABBREVIATIONS

|                        |   |   |
|------------------------|---|---|
| a.u.                   | = | Arbitrary units                                     |
| $D, \langle D \rangle$ | = | Average crystallite size                            |
| DMS                    | = | Diluted magnetic semiconductor                      |
| DW–stat                | = | Durbin–Watson statistic                             |
| EDS                    | = | Energy dispersive X-ray spectroscopy                |
| $E_g$                  | = | Band gap energy                                     |
| eV                     | = | Electron volt                                       |
| FWHM                   | = | Full width at the half maximum                      |
| $H_c$                  | = | Coercive field                                      |
| $H$                    | = | Magnetic field                                      |
| JCPDS                  | = | the Joint Committee on Powder Diffraction Standards |
| K                      | = | Kelvin  |
| $M$                    | = | Magnetization                                       |
| MBE                    | = | Molecular beam epitaxy                              |
| MOCVD                  | = | Metalorganic chemical vapor deposition              |
| $M_R$                  | = | Magnetic remanence                                  |
| $M_s$                  | = | Saturation magnetization                            |
| NIR                    | = | Near Infrared                                       |
| Oe                     | = | Oersted   |
| OPA-MBE                | = | Oxygen-plasma-assisted molecular-beam epitaxy       |
| PLD                    | = | Pulsed laser deposition                             |
| $R_B$                  | = | Bragg Factor  |
| $R_{exp}$              | = | Expected R value                                    |
| $R_F$                  | = | Crystallographic Factor                             |
| $R_p$                  | = | Profile Factor                                      |
| $R_{WP}$               | = | Weighted Profile Factor                             |
| SEM                    | = | Scanning electron microscopy                        |
| SQUID                  | = | Superconducting quantum interference device         |

## ABBREVIATIONS (CONTINUED)

|                |   |  |
|----------------|---|--|
| $T$            | = | Absolute temperature                             |
| T              | = | Tesla  |
| $T_c$          | = | Currie temperature                               |
| TEM            | = | Transmission electron microscopy                 |
| Temp.          | = | Temperature                                      |
| TM             | = | Transition metals                                |
| $T_N$          | = | Néel temperature                                 |
| UV             | = | Ultra violet                                     |
| VIS            | = | Visible  |
| VSM            | = | vibrating sample magnetometer                    |
| WHP            | = | Williamson–Hall Plot                             |
| XPS            | = | X-ray photoelectron spectroscopy                 |
| XRD            | = | X-ray diffraction                                |
| $y_i (calc)$   | = | The net intensity calculated at point $i$        |
| $y_i (bgnd)$   | = | The background intensity calculated at point $i$ |
| $y_i (obs)$    | = | The observed intensity at point $i$              |
| $\chi$         | = | Magnetic susceptibility                          |
| $\mu_B$ / f.u. | = | Bohr magnetons per formula unit                  |

# CHAPTER 1

## INTRODUCTION

Diluted magnetic semiconductors (DMS) are semiconducting materials in which a fraction of the host cations can be substitutionally replaced by magnetic ions or appropriate rare earths. Much of the attention on DMS materials is due to its potential application in what is now called “Spintronics” devices, which exploit spin in magnetic materials along with charge of electrons in semiconductors [1]. The magnetism in DMS is due to the finite magnetic moments localized at impurity ions. Consequently, in order to fabricate a DMS, one can choose a certain atom to incorporate into the host materials in such a way that the finite magnetic moments appear at lattice sites or other places in the host and an impurity band is formed in the band gap. Another approach to driving a semiconductor ferromagnetic is to introduce magnetic ions into non-magnetic semiconductors [2]. In these ferromagnetic semiconductors, a part of the lattice is made up of substitution magnetic atoms. Transition metals that have partially filled  $d$  states (Ti, V, Cr, Mn, Fe, Co, Ni and Cu) and rare earth elements that have partially filled  $f$  states (e.g. Eu, Gd, Er) have been used as magnetic atoms in DMS. The partially filled  $d$  states or  $f$  states contain unpaired electrons, in terms of their spins, which are responsible to exhibit magnetic their behavior. In DMS materials, the delocalized conduction band electrons and valence band holes interact with the localized magnetic moments associated with the magnetic atoms. Generally, when  $3d$  transition metal ions are substituted for the cations in the host, the resultant electronic structure is influenced by strong hybridizations of the  $3d$  orbitals of the magnetic ion and mainly the  $p$  orbitals of the neighboring host anions. Those hybridizations give rise to the strong magnetic interaction between the localized  $3d$  spins and the carriers in the host valence bands. Due to the necessity that the DMS materials must exhibit ferromagnetism with a critical temperature above room temperature in order to have practical applications in spintronics devices, so that the Curie temperature ( $T_C$ ), is naturally deemed to be the bottleneck issue.

There are two major criteria for selecting the most promising materials for semiconductor spintronics. First, the ferromagnetism should be retained to above room temperature (high Curie temperature i.e.  $>300$  K). Second, the electrical and optical properties of



ferromagnetic semiconductors should allow for spin manipulation. An essential task is to find a DMS with the Curie point above room temperature. Theoretical developments are rekindled hope for a possibility of ferromagnetism in DMS above room temperature [3].

Many promising applications of ferromagnetic semiconductors have been already demonstrated for amorphous III – V semiconductors such as (Ga,Mn)As [4]. When divalent transition metal ions substitute for trivalent cations in a III – V host, holes are also introduced, which are believed to mediate the observed ferromagnetic ordering in these systems. The Curie temperature ( $T_C$ ) are generated, but have not reached the room temperature values. The new DMS having  $T_C$  beyond room temperature is desired for future devices. A possible scenario of increasing  $T_C$  of ferromagnetic semiconductors is theoretically proposed to use wide band gap semiconductors and can be doped heavily with  $n$ -type carrier as host materials. This feature serves an important role as the transparent conductor that is used for various applications. Among them, oxide semiconductors are one of the promising candidates to realize high  $T_C$  ferromagnetic semiconductors.

Generally, oxide semiconductors have wide band gaps, i.e. transparent for visible light, and can be doped heavily with  $n$ -type carrier. This feature serves an important role as the transparent conductor that is used for various applications. Recently several oxide-based DMSs have been reported to be robust, room temperature ferromagnetism. In 2001, Matsumoto *et al.* [5] first experimentally reported about room temperature ferromagnetic in Co-doped  $\text{TiO}_2$  thin films, but the obtained magnetic moment is still very modest. Since then, a lot of competitions have been going on in the field, where to look for a new simply ferromagnetic compound at room temperature, or to find large magnetic moment materials. Since the mechanism that governs the magnetism in this kind of systems is still not clear, and actually rather controversial, many research groups have been trying to elucidate these issues. With the aim to verify somehow these debating issues, systematic investigations on magnetism of transition metals (TM)-doped oxide semiconductor such as  $\text{TiO}_2$ ,  $\text{SnO}_2$ ,  $\text{In}_2\text{O}_3$  and  $\text{ZnO}$  have been done. Many researchers on TM-doped oxide semiconductors have been reports. However, there still has been a little report on TM-doped  $\text{SnO}_2$ .

Tin oxide ( $\text{SnO}_2$ ), an  $n$ -type semiconductor with a wide band gap, is an attractive host lattice for the investigation of DMS ferromagnetism. It is natively  $n$ -type because of oxygen vacancies, a high carrier density, and a structure similar to that of  $\text{TiO}_2$ , the lattice in which high

Curie temperature ( $T_C$ ) oxide DMS ferromagnetism was first discovered [5]. Its high optical transparency, electrical conductivity, and chemical sensitivity make it a very attractive material for several applications. In addition, it can be easily synthesized at low cost with excellent quality.

In this work, the optical and magnetic properties of transition metals doped  $\text{SnO}_2$  were studied. In order to avoid the formation of transition metal particles, a wet chemical route was chosen to prepare the samples. Therefore, transition metal doped  $\text{SnO}_2$  nanoparticle samples ( $\text{Sn}_{1-x}\text{TM}_x\text{O}_{2-\delta}$ ), which TM = Cr and Co with  $x \leq 0.015$  and Fe with  $x \leq 0.30$ , were synthesized by the autocombustion technique. The novel autocombustion method could be initiated at low temperature, self-propagating and gas producing. In such situation, the auto-combustion method was a simple, fast and energetically attractive method that could be adopted for the bulk production of high purity metal oxides. In addition, there was a control over stoichiometry, homogeneity and purity. It was easy to dope desired amount of impurity ions. The fine powder samples were then characterized in several techniques such as XRD, SEM and TEM. Moreover, band gap energies and magnetic properties of these nanoparticles were investigated.

In summary, the scopes of this work were:

- (1) To prepare the transition metals doped  $\text{SnO}_2$  nanoparticles ( $\text{Sn}_{1-x}\text{TM}_x\text{O}_{2-\delta}$ , where TM = Cr and Co with  $x \leq 0.015$  and Fe with  $x \leq 0.30$ ) by using the autocombustion technique;
- (2) To characterize the physical, optical and magnetic properties of these nanoparticles.

## **CHAPTER 2**

### **LITERATURE REVIEW**

The purpose of this Chapter is to introduce the essential background knowledge in order to understand the diluted magnetic semiconductor (DMS) material. It was divided into four sections. Firstly, the DMS phenomena are described in Section 2.1. Ferromagnetism in the DMS is defined in Section 2.2. In Section 2.3, the history of the early works on the DMS materials is reviewed either the DMS based on  $\text{TiO}_2$  and  $\text{ZnO}$  or the DMS based on  $\text{SnO}_2$ . Finally, the preparation method, especially autocombustion technique is given.

#### **2.1 Diluted Magnetic Semiconductors (DMS)**

Semiconductors with magnetic elements as dopants are interesting in semiconducting and magnetic properties, and they are known as magnetic semiconductors. These compounds exhibit various magnetic properties such as ferromagnetism and antiferromagnetism depending on the amount and identity of magnetic elements present. The Diluted Magnetic Semiconductors (DMS), as shown in Figure 2.1, are alloys between a non-magnetic semiconductor and a lower concentration of magnetic elements. Therefore, semiconducting and ferromagnetic properties coexist in these materials. This leads to important technological applications since the charge and the spin of the electron could be used on the same device. At the same time, the underlying solid state system has an enormous interest for basic science.

The applications of semiconductors mainly depend on the ability to dope them with impurities to change their properties. Thus the enormous success of conventional semiconductor devices is solely based on the charge carried by electrons. The spin of electrons has been used in information storage in magnetic materials. Magnetic semiconductors give both properties of electrons, charges and spins, simultaneously in semiconductors. This field is often referred to as spintronics (spin-based electronics). The ability to manipulate electron spin in semiconductors is expended to lead to the development of remarkable improvements in electronic systems and devices used in photonics, data processing, and communication technology. The predicted

advantages of these new devices are no volatility, increased data processing speed, decreased electric power consumption, and increased integration densities compared with conventional semiconductor devices.

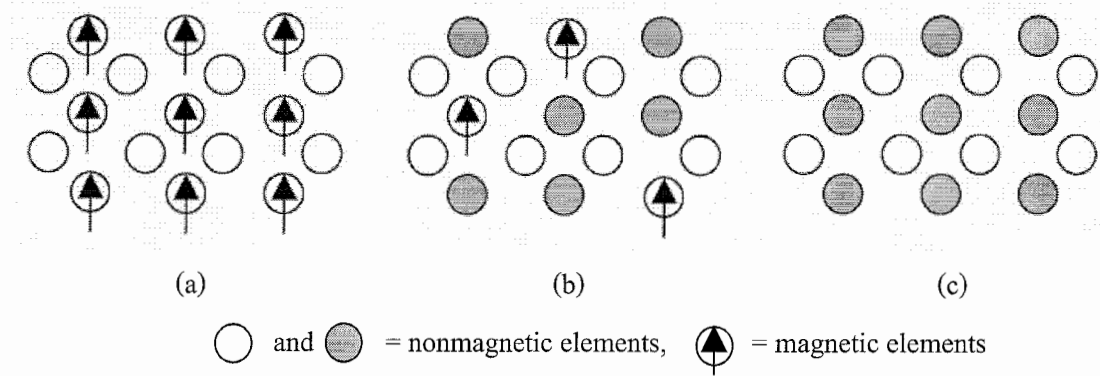


**Figure 2.1** Schematic illustration of (a) a magnetic semiconductor, which has a periodic array of a magnetic element, (b) a diluted magnetic semiconductor (DMS), an alloy between a nonmagnetic semiconductor and a magnetic element and (c) a non-magnetic semiconductor, which contains no magnetic ions. (adapted from Ref. [6])

## 2.2 Ferromagnetism in DMS

Ferromagnetic materials have a large and positive susceptibility to an external magnetic field. They exhibit a strong attraction to magnetic fields and are able to retain their magnetic properties after the external field has been removed. All ferromagnetic materials have atomic magnetic moments that are aligned parallel to each other within small regions, called domains. In these domains, large numbers of atom's moments are aligned parallel so that the magnetic force within the domain is strong. In the absence of an applied field, there is no net magnetic moment or field generated by the material because the magnetization direction of each domain is randomly oriented. When a magnetizing force is applied, the domains become aligned to produce a strong magnetic field within the part.

Ferromagnetism will tend to stay magnetized to some extent after being subjected to an external magnetic field. This tendency to remember their magnetic history is called hysteresis. During magnetization of the materials, domains have a component in the direction of the applied field which will grow at the expense of those that do not. Once all of the unfavorably oriented

domains have been eliminated by domain wall movement, the magnetization direction of the single domain that remains will be rotated to be parallel to that of the applied field as seen in Figure 2.2.

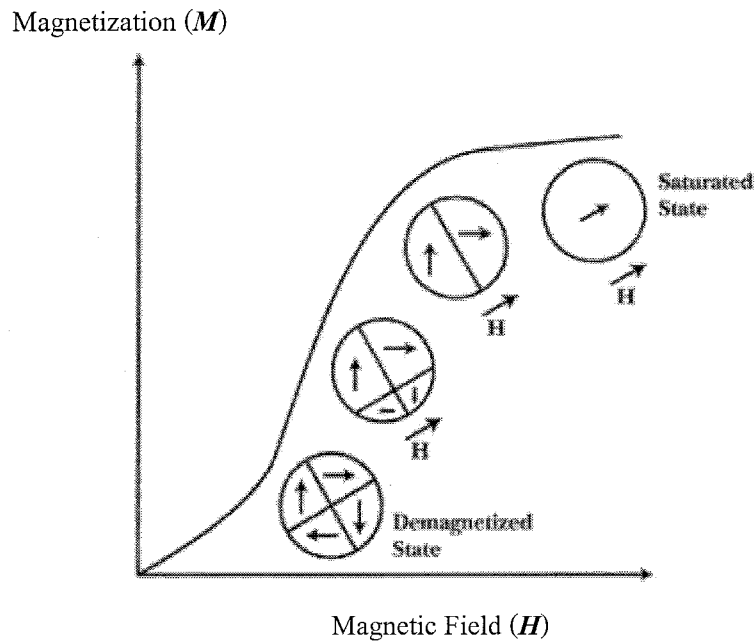


**Figure 2.2** The magnetization directions of the single domain.

During magnetization, an increasing magnetic field is applied to the material until a saturation point is reached. Upon removing this applied field, a permanent magnet material will not follow the same path down to magnetic field = 0, instead, it will retain some of its magnetism. The path is a key tool in the quantitative analysis of permanent magnet performance. A hysteresis loop shows the relationship between the magnetization ( $M$ ) and the magnetic field ( $H$ ). An example hysteresis loop is shown in Figure 2.3.

The loop is generated by measuring the magnetization of a ferromagnetic material while the magnetizing force is changed. The ferromagnetic material that has never been previously magnetized or has been thoroughly demagnetized will follow the dashed line as  $H$  is increased. As the line demonstrates the greater the amount of current applied ( $H+$ ), the stronger the magnetic field in the component ( $M+$ ). At point "a", almost all of the magnetic domains are aligned and an additional increase in the magnetic field will produce very little increase in

magnetization. The materials have reached the point of the saturation magnetization ( $M_s$ ). When  $H$  is reduced to zero, the curve will move from point "a" to point "b". At this point, it can be seen that some magnetizations remain in the materials even though the magnetic field is zero. This is referred to as the point of the remanence magnetization ( $M_R$ ) or level of residual magnetism in the materials. As the magnetic field is reversed, the curve moves to point "c", where the magnetization has been reduced to zero. This point is called the coercivity field ( $H_C$ ) of the materials.

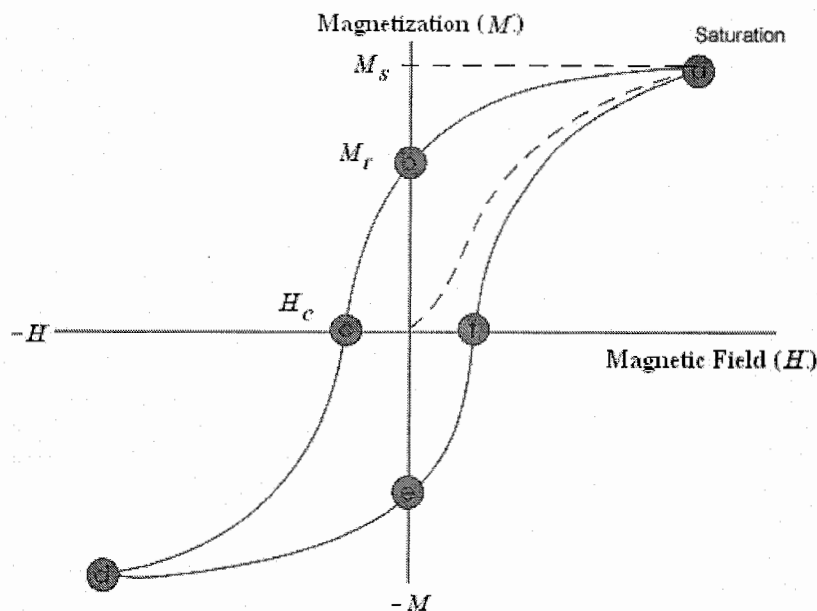


**Figure 2.3** The relationship between the magnetization ( $M$ ) and the magnetic field ( $H$ ) hysteresis loop.

As the magnetic field is increased in the negative direction, the material will again become magnetically saturated but in the opposite direction (point "d"). Reducing  $H$  to zero brings the curve to point "e". It will have a level of residual magnetism which equal to that achieved in the other direction. Increasing  $H$  back in the positive direction will return  $M$  to zero. Notice that the curve do not return to the origin of the graph because some forces are required to remove the residual magnetism. The curve will take a different path from point "f" back to the saturation point to complete the loop.

## 2.3 DMS Materials

A magnetic semiconductor is expected to be a promising candidate material for the next generation spintronics devices utilizing electronically or optically controlled magnetism. In 1992, Ohno *et al.* [7] reported magnetotransport properties of a new diluted magnetic semiconductor based on a III-V semiconductor (*p*-type (In,Mn)As). They showed ferromagnetism in epitaxial films of (In,Mn)As grown by molecular beam epitaxy (MBE). The Curie temperature was ~35 K. Moreover, in 1996 [4], they grew (Ga,Mn)As films by solid source MBE. The lattice constant of the films was found to increase with the increase of Mn concentration. Well-aligned in-plane ferromagnetic order was observed by magnetization measurements. The Curie temperature was ~110 K. However, the highest Curie temperatures in the single phase samples reported for these materials are too low for most practical applications. Moreover, arsenic is the important ion for air pollution. Several researchers have since then reported observation of room temperature ferromagnetism in doped semiconductors. A considerable attention has been paid to semiconductors doped with ferromagnetic metals (Co, Fe, Ni, etc.). Therefore, new DMS having  $T_C$  beyond room temperature is desired for future devices.

Compared to non-oxide semiconductors, the advantages of oxide semiconductors are: (1) wide bandgap suited for applications with short wavelength light, (2) transparency and dyeability with pigments, (3) high *n*-type carrier concentration, (4) capability to be grown at low temperature even on plastic substrate, (5) ecological safety and durability, and (6) low cost, etc. Such their advantages make oxide semiconductors attractive. There have been several reviews on the magnetic oxide semiconductors [8-9]. Various ferromagnetic oxide semiconductors have been reported so far; however, the ferromagnetism has been still a matter for strong debate.

### 2.3.1 DMS Based on TiO<sub>2</sub>

Titanium dioxide (TiO<sub>2</sub>) has been extensively studied for its unique properties, both physical and chemical properties. The TiO<sub>2</sub> is a wide band gap semiconductor. Anatase TiO<sub>2</sub> has been shown by Matsumoto *et al.* [5]. They reported that TiO<sub>2</sub> doped with the concentration of cobalt between 0 and 8% are ferromagnetic at room temperature. Films of Ti<sub>1-x</sub>Co<sub>x</sub>O<sub>2</sub> were made on LaAlO<sub>3</sub> (001) and SrTiO<sub>3</sub> (001) single crystal substrates by combinatorial laser MBE.

No phase segregation was indicated by TEM images. An increase in spontaneous magnetization with the increase of Co content was observed. Presence of hysteresis in the magnetization curve indicated room temperature ferromagnetism, with the magnetic moment of 0.32 Bohr magnetons per cobalt atom ( $\mu_B/\text{Co}$ ). The films were transparent in the visible and infrared region and had a band gap of 3.1 eV. Matsumoto *et al.* [5] agreed that a possibility of Co clusters cannot be completely ruled out though, XRD and TEM showed no sign of metal granules. In a later article, they stated that room temperature ferromagnetism exists in rutile phase of  $\text{Ti}_{1-x}\text{Co}_x\text{O}_2$  with a moment of 1  $\mu_B/\text{Co}$  atom for 3% Co substitution.

Chambers *et al.* [10] had grown  $\text{Ti}_{1-x}\text{Co}_x\text{O}_2$  films by MBE on  $\text{SrTiO}_3$  substrates. They reported a magnetic moment of 1.26  $\mu_B/\text{Co}$  for films with  $x = 0.03$ , significantly higher than the moment reported by Matsumoto *et al.* [5]. Chambers *et al.* [10] also reported that the cobalt distribution in their films depends strongly on growth conditions leading to some of their films being nonmagnetic. Thus a moment of 1  $\mu_B/\text{Co}$  was expected. In nonmagnetic films, they found that cobalt had segregated to the surface of the film. In a later, Chambers *et al.* [11] reported segregation of Co-enriched  $\text{TiO}_2$  anatase clusters nucleate on epitaxial  $\text{TiO}_2$  anatase grown on  $\text{LaAlO}_3$  (001) by oxygen plasma assisted MBE. In extreme case almost all the incident Co segregated to the clusters yielding a nanoscale ferromagnetic phase that was not ferromagnetic in homogeneous films of the same Co concentration. Room temperature ferromagnetism (moment  $\sim 1.7 \mu_B$ ) in  $\text{TiO}_2:\text{Co}$  transparent films grown on both  $\text{LaAlO}_3$  (001) and  $\text{SrTiO}_3$  (001) substrates by Pulsed laser deposition (PLD) was reported by Stampe *et al.* also [12]. In some cases even exceed the value for Co metal (1.76  $\mu_B/\text{Co}$ ) [13] and the different room temperature magnetic moments in Co-doped  $\text{TiO}_2$  were reported  $\sim 1.7 \mu_B/\text{Co}$  [14] and  $0.16 \mu_B/\text{Co}$  [15]. For transition metal dopants other than Co, it is very difficult to derive trends from the available experimental information, since there is much less of it available. However, electronic structures of transition metals-doped  $\text{TiO}_2$  have been investigated [16]. Furthermore, the room temperature ferromagnetism in anatase  $\text{TiO}_2$  has been frequently exploited to claim ferromagnetic oxide-based DMS [17-18]. Actually, many studies on  $\text{TiO}_2$ -based DMS have been reported as summarized in Table 2.1.



**Table 2.1** List of transition metals (1<sup>st</sup> series) doped TiO<sub>2</sub>-based DMS recently reported

| Compound                            | TM content  | Substrate                               | Fabrication method     | Growth temperature (K) | T <sub>c</sub> (K) | Notes                                   | Reference |
|-------------------------------------|-------------|---|------------------------|------------------------|--------------------|---|-----------|
| Anatase TiO <sub>2</sub> :Co        | <0.08       | LaAlO <sub>3</sub> , SrTiO <sub>3</sub> | PLD                    | 950-1000               | >400               | 0.32 $\mu_B$ /Co                        | [5]       |
| Anatase TiO <sub>2</sub> :Co        | 0.01-0.1    | SrTiO <sub>3</sub>                      | OPA-MBE                | 573-1023               | >300               | 1.26 $\mu_B$ /Co                        | [10]      |
| Anatase TiO <sub>2</sub> :Co        | 0.01-0.07   | LaAlO <sub>3</sub> , SrTiO <sub>3</sub> | PLD                    | 1023                   |                    | Co cluster, 1.7 $\mu_B$ /Co             | [12]      |
| Anatase TiO <sub>2</sub> :Co        | <0.15       | LaAlO <sub>3</sub> , SrTiO <sub>3</sub> | PLD                    | 973                    | 650-700            | 1.4 $\mu_B$ /Co                         | [19]      |
| Anatase TiO <sub>2</sub> :Co        | 0-0.1       | LaAlO <sub>3</sub> , SrTiO <sub>3</sub> | OPA-MBE                | 823-873                |                    | 1.2-1.4 $\mu_B$ /Co                     | [20]      |
| Anatase TiO <sub>2</sub> :V         | 0.05        | LaAlO <sub>3</sub>                      | Laser ablation         | 873-973                | >400               | 4.2 $\mu_B$ /V                          | [21]      |
| Anatase TiO <sub>2</sub> :Co        | 0.03-0.12   | SiO <sub>2</sub> /Si                    | MOCVD                  | 673-773                | >RT                | 20-40 emu/cm <sup>3</sup>               | [22]      |
| Anatase TiO <sub>2</sub> :Co        | 0.04        | SrTiO <sub>3</sub>                      | PLD                    | 873                    |                    | Co metal, 1.7-2.3 $\mu_B$ /Co           | [23]      |
| Anatase TiO <sub>2</sub> :Co        | 0.04-0.1    | LaAlO <sub>3</sub>                      | PLD                    | 923                    |                    | Co cluster, 1.55 $\mu_B$ /Co            | [24]      |
| Anatase TiO <sub>2</sub> :Co        | <0.08       | c-Sapphire                              | Spin-coating colloidal | 623 (annealing)        | N/A                | 0.0015-1.9 $\mu_B$ /Co <sup>2+</sup>    | [25]      |
| Anatase TiO <sub>2</sub> :Co        | 0.02, 0.07  | LaAlO <sub>3</sub>                      | Reactive sputtering    |                        | N/A                | 0.7 $\mu_B$ /Co                         | [26]      |
| Anatase TiO <sub>2</sub> :Co        |             | LaAlO <sub>3</sub>                      | Co-sputtering          | 298-1023               | >400               | 1.13 $\mu_B$ /Co                        | [27]      |
| Anatase TiO <sub>2</sub> :Co        | 0.01-0.1    | Si                                      | Sputtering             | 523-723                | >400               | 0.94 $\mu_B$ /Co                        | [28]      |
| Rutile/anatase TiO <sub>2</sub> :Cr | <0.01       | TiO <sub>2</sub>                        | OPA-MBE                | 973                    | N/A                | 0.29 $\mu_B$ /Cr                        | [29]      |
| Rutile/anatase TiO <sub>2</sub> :Cr | 0.02-0.16   | TiO <sub>2</sub> , LaAlO <sub>3</sub>   | OPA-MBE                |                        | N/A                | 0.6 $\mu_B$ /Cr                         | [30]      |
| Rutile TiO <sub>2</sub> :(Fe, Ni)   | 0.043-0.126 | Silicon                                 | Laser ablation         | 973                    | ~400               | 2.22 $\mu_B$ /Fe<br>and 0.6 $\mu_B$ /Co | [31]      |

### 2.3.2 DMS Based on ZnO

ZnO is a II – VI semiconductor with a wide band gap of about 3.35 eV. It is a well-known piezoelectric and electro-optic material, and can be easily deposited in thin film form. There are wide applications in electronic devices such as transparent conductor, thin film gas sensor, varistor, etc. The stable crystal structure of ZnO is a wurtzite, in which each atom of zinc is surrounded by four atoms of oxygen in tetrahedral coordination. Transition metal-doped ZnO has the potential to be a highly multifunctional material with coexisting magnetic, semiconducting, electromechanical, and optical properties. Most of the initial experimental works on transition metal-doped ZnO have focused on thin films with Mn or Co doping.

The first experiment on Mn-doped ZnO was performed by Fukumura *et al.* [32], who prepared  $\text{Zn}_{0.64}\text{Mn}_{0.36}\text{O}$  films using pulsed laser deposition (PLD) on a polished *c*-plane sapphire substrate. The substrate temperature was maintained at 873 K and the oxygen partial pressure at  $10^{-5}$  Torr. X-ray diffraction measurements showed that the films were of the wurtzite structure without any impurity phases. In addition, electron-probe microanalysis confirmed that the Mn in the film was distributed homogeneously. Magnetic properties were measured using a SQUID magnetometer, which indicated spin-glass behaviour with a freezing temperature of ~13 K and a large Curie-Weiss temperature suggesting strong *antiferromagnetic* exchange coupling.

The first report of ferromagnetism in Co-doped ZnO was made by Ueda *et al.* [33], for thin films of  $\text{Zn}_{1-x}\text{Co}_x\text{O}$  ( $x = 0.05 - 0.25$ ) prepared using PLD on sapphire substrates. The films were formed with 1% Al atomic weight added to increase the carrier concentration. Both  $\text{Zn}_{0.95}\text{Co}_{0.05}\text{O}$  and  $\text{Zn}_{0.85}\text{Co}_{0.15}\text{O}$  showed ferromagnetic hysteresis loops with saturation magnetic moments of 1.8 and 2.0  $\mu_B/\text{Zn}$ , respectively. The saturation magnetization and Curie temperature increased with increasing in the carrier concentration. However, the claims concerning the existence of ferromagnetism have diverged. Several researches claimed nonferromagnetic behaviors of ZnO doped with TM, whereas the other groups claimed ferromagnetic behavior of the same compounds. The reported values of  $T_c$  scatter from 30 to 550 K [17-18, 34]. Actually, many studies on ZnO doped with various kinds of transition metals have been reported as summarized in Table 2.2.

**Table 2.2** List of transition metals (1<sup>st</sup> series) doped ZnO-based DMS recently reported

| Compound     | TM content | Substrate                      | Fabrication method   | Growth temperature (K) | $T_c$ (K)          | Notes   | Reference |
|--------------|------------|--------------------------------|----------------------|------------------------|--------------------|---|-----------|
| ZnO:Mn       | 0.36       | c-Sapphire                     | PLD                  | 873                    | N/A                | Spin-glass  | [35]      |
| ZnO:Co       | 0.02-0.5   | c-Sapphire                     | PLD                  | 573-973                | 300                | Paramagnetic (homogeneous),<br>Ferromagnetic, spin glass (x=0.25) | [36]      |
| ZnO:Cr       | 0.05       |                                | Co-precipitation     |                        |                    | Ferromagnetic-like (300 K),<br>spin-glass (77 K)                  | [37]      |
| ZnO:Mn       | 0.01–0.36  | c-Sapphire                     | PLD                  | 883                    | N/A                | Paramagnetic  | [38]      |
| ZnO:(Mn, Co) | 0.03-0.5   |                                |                      | 623                    | 250 (Mn), 300 (Co) |   | [39]      |
| ZnO:Ni       | 0.01–0.25  | c-Sapphire                     | PLD                  | 573-973                | N/A                | Superpara- or Ferro-magnetic                                      | [40]      |
| ZnO:V        | 0.05–0.15  | Al <sub>2</sub> O <sub>3</sub> | PLD                  | 973                    | >350               | 0.5 $\mu_B$ /V  | [41]      |
| ZnO:(Co, Fe) | <0.15      | Si/SiO <sub>2</sub>            | Magnetron sputtering | 873                    | >300               | 12–15 emu/cm <sup>3</sup>   | [42]      |
| ZnO:Co       | 0–0.25     | Al <sub>2</sub> O <sub>3</sub> | Sol-gel              | >350                   | >350               | 0.56 $\mu_B$ /Co  | [43]      |
| ZnO:Mn       | 0–0.3      | Al <sub>2</sub> O <sub>3</sub> | MBE                  |                        | >30–45             | 0.15–0.17 $\mu_B$ /Mn   | [44]      |
| ZnO:(Fe, Cu) | 0–0.1      |                                | Solid state reaction | 1170                   | 550                | 0.75 $\mu_B$ /Fe  | [45]      |
| ZnO:Co       | 0.25       | c-Sapphire                     | PLD                  | 673-973                | N/A                | Co cluster  | [46]      |
| ZnO:Ni       | 0–0.20     |                                | Autocombustion       |                        | N/A                | 0.29 $\mu_B$ /Ni <sup>2+</sup>                                    | [47]      |
| ZnO:Mn       | 0.30       | Al <sub>2</sub> O <sub>3</sub> | PLD                  | 973                    | N/A                |   | [48]      |
| ZnO:Mn       | 0.01–0.10  |                                | Co-precipitation     | 1173                   | N/A                | paramagnetic (x ≤ 0.05 )<br>and no ferromagnetic                  | [49]      |

### 2.3.3 DMS Based on SnO<sub>2</sub>

One of the other wide band gap oxide semiconductors, tin oxide (SnO<sub>2</sub>), has been investigated as the transparent electrode and gas sensor material. SnO<sub>2</sub> crystal has a rutile structure with an octahedral coordination similar to anatase TiO<sub>2</sub>, where the body-centered cation has six neighboring oxygen ions, forming octahedral ligands of oxygen. The octahedral coordination of ligand field creates about 9/4 times larger crystal field than the tetrahedral coordination, hopefully leading to different from the existing DMS. SnO<sub>2</sub> is an *n*-type semiconductor with a wide band gap of ~3.6 eV [50]. Its high optical transparency, electrical conductivity, and chemical sensitivity make it a very attractive material for solar cells, heat mirrors, catalysis, and gas-sensing applications. In addition, it can be easily synthesized at low cost with excellent qualities. This material has once again captured the attention of scientific community due to its application potential in the areas of the spintronics.

The first report of SnO<sub>2</sub> DMS was studied by Kimura *et al.* [50], who prepared the epitaxial thin films of an oxide-DMS with a rutile structure, Sn<sub>1-x</sub>Mn<sub>x</sub>O<sub>2</sub> and Sn<sub>1-x</sub>Mn<sub>x</sub>O<sub>2</sub> : Sb which  $x = 0, 0.05, 0.11$  and  $0.34$ . These films were fabricated by pulsed laser deposition (PLD) method on polished sapphire substrates. The optical properties showed the in-gap absorption and the magnetization measurement exhibited paramagnetic behavior. The first report room temperature ferromagnetism was performed in Co-doped SnO<sub>2</sub> by Ogale *et al.* [51]. The Sn<sub>1-x</sub>Co<sub>x</sub>O<sub>2-δ</sub> which  $x \leq 0.3$  thin films were prepared by PLD. At low dopant concentration, it was seen to be ferromagnetic, with a Curie temperature close to 650 K. Moreover, the strong ferromagnetic behavior at room temperature with a giant magnetic moment as high as  $7.5 \pm 0.5 \mu_B/\text{Co ion}$  was also observed, and it was seen to drop rapidly with increase in the Co content.

Punnoose *et al.* [52] prepared high purity powder samples of Co-doped SnO<sub>2</sub> with  $x \leq 0.05$  using a wet chemical method. The precipitates were annealed in air at temperatures in the range of 623 – 873 K. Interestingly, SnO<sub>2</sub> samples doped with  $\leq 1\%$  Co atomic weight showed room temperature ferromagnetism with significantly high coercivity (~630 Oe), moderate remanance (~31%) from the hysteresis measurements. The saturation magnetization had a lower magnetic moment of  $0.133 \mu_B/\text{Co ion}$  (compared to  $\sim 1.67 \mu_B/\text{Co ion}$  for Co metal). Room temperature ferromagnetism has been observed a detail in Co and Fe-doped SnO<sub>2</sub> powders

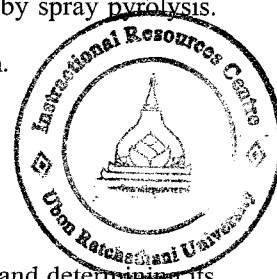
focusing the preparation temperature at 873 K [53]. The high temperature magnetic measurements of  $\text{Sn}_{0.99}\text{Co}_{0.01}\text{O}_2$  obtained a Curie temperature  $T_C$  of 440 K. In addition, the results of a detailed investigation of the structural, optical, and magnetic properties of chemically synthesized pure and Co-doped  $\text{SnO}_2$  powders in several techniques were presented [54]. The  $\text{Sn}_{1-x}\text{Co}_x\text{O}_2$  samples were prepared at 873 K. Increasing the Co doping concentration to  $> 1\%$  led to completely destroy the ferromagnetism.

The magnetism of Fe-doped  $\text{SnO}_2$  was investigated by Coey *et al.* [55]. The powder samples were first prepared by a solid-state reaction of  $\text{SnO}_2$  and FeO at 1423 K. They were ferromagnetic, with magnetic moment of  $\sim 1.2 \mu_B/\text{Fe}$ , and a Curie temperature of 360 K. The thin films were then grown by PLD on *R*-cut sapphire substrates. The Curie temperature was 610 K. The net ferromagnetic moment was  $1.8 \mu_B/\text{Fe}$ , which was greater than that of their oxide powders. The Mössbauer spectra showed that the iron was all high-spin  $\text{Fe}^{3+}$ .

Moreover, Punnoose *et al.* [56] reported the room-temperature ferromagnetism in chemically synthesized powder samples of *p*-type SnO and *n*-type  $\text{SnO}_2$  by doping them with Fe. The precipitated of  $\text{Sn}_{0.95}\text{Fe}_{0.05}\text{O}_2$  was annealed at different temperatures between 473 and 1173 K. The powder samples of  $\text{Sn}_{1-x}\text{Fe}_x\text{O}_2$  with  $0.005 \leq x \leq 0.05$  showed room-temperature ferromagnetism, whereas only paramagnetic behavior was observed in  $\text{Sn}_{1-x}\text{Fe}_x\text{O}$ . The ferromagnetic  $\text{Sn}_{0.99}\text{Fe}_{0.01}\text{O}_2$  showed  $T_C = 850$  K. With increasing Fe doping, the lattice parameters of  $\text{SnO}_2$  decreased and the saturation magnetization increased.

Preparation of grown Cr-doped  $\text{SnO}_2$  thin films on various kinds of substrates showed different ferromagnetism beyond room temperature as confirmed by Hong *et al.* [57]. The  $\text{Sn}_{0.95}\text{Cr}_{0.05}\text{O}_2$  thin films grown on  $\text{LaAlO}_3$  substrates had a giant magnetic moment of  $6 \mu_B/\text{Cr}$ , which was 20 – 30 times larger than that of films grown under the same conditions on  $\text{SrTiO}_3$  and *R*-cut sapphire substrates. Moreover, in  $\text{Sn}_{0.95}\text{V}_{0.05}\text{O}_2$  [58] and  $\text{Sn}_{0.95}\text{Ni}_{0.05}\text{O}_2$  [59] thin films grown by the PLD technique on  $\text{LaAlO}_3$ ,  $\text{SrTiO}_3$  as well as *R*-cut  $\text{Al}_2\text{O}_3$  substrates all showed the different room temperature ferromagnetism. No ferromagnetism was observed in V-doped  $\text{SnO}_2$  thin films grown on  $\text{Al}_2\text{O}_3$  substrates but thin films on either  $\text{LaAlO}_3$  or  $\text{SrTiO}_3$  substrates were all ferromagnetic above a room temperature with  $T_C$  of about 400 K. The V-doped  $\text{SnO}_2$  films grown on  $\text{LaAlO}_3$  substrates had a large magnetic moment of about  $3 \mu_B/\text{V}$ , which was larger than on  $\text{SrTiO}_3$  substrates. In addition, the Ni-doped  $\text{SnO}_2$  films on  $\text{LaAlO}_3$  substrates had a large magnetic moment of about  $2 \mu_B/\text{Ni}$ , also greater than on  $\text{SrTiO}_3$  and  $\text{Al}_2\text{O}_3$  substrates.

Furthermore, Fitzgerald *et al.* [60] reported the room temperature ferromagnetism in  $\text{Sn}_{0.95}\text{TM}_{0.05}\text{O}_2$  (TM = Mn, Fe, Co) polycrystalline samples. The samples were prepared by a solid state reaction method and sintered at 1423 K. The room temperature ferromagnetism was observed in  $\text{Sn}_{0.95}\text{Mn}_{0.05}\text{O}_2$  and  $\text{Sn}_{0.95}\text{Fe}_{0.05}\text{O}_2$  with magnetic moments of  $0.11 \mu_B/\text{Mn}$  and  $0.95 \mu_B/\text{Fe}$  ions, respectively. In addition, Curie temperatures were 340 K and 360 K for 5% Mn and Fe-doped  $\text{SnO}_2$  samples, respectively. The Co-doped samples were paramagnetic at room temperature. Moreover, Cr- and Fe-doped  $\text{SnO}_2$  films still were reported by Wang *et al.* [61].  $\text{Sn}_{1-x}\text{Fe}_x\text{O}_2$  and  $\text{Sn}_{1-x}\text{Cr}_x\text{O}_2$  thin films with  $x = 0, 0.02, 0.06, 0.10, 0.20$  were deposited on  $\text{Al}_2\text{O}_3$  substrates by pulsed-laser deposition. The X-ray diffraction peaks of Cr-doped samples exhibited a systematic shift toward higher angles with increasing Cr concentration. This indicated that Cr dissolved in  $\text{SnO}_2$ . On the other hands, XRD experiments did not show similar results for Fe-doped films. The magnetization curves indicated that the Cr-doped  $\text{SnO}_2$  films were completely paramagnetic. The Fe-doped  $\text{SnO}_2$  samples were ferromagnetic at 300 and 5 K. In addition, a maximum room temperature ferromagnetic was observed by Gopinadhan *et al.* [62]. Thin films of  $\text{Sn}_{1-x}\text{Co}_x\text{O}_{2-\delta}$  with  $x = 0.00, 0.05, 0.10, \text{ and } 0.15$  were prepared by spray pyrolysis. A maximum magnetic moment of  $0.47 \mu_B/\text{Co}$  ion occurred in  $\text{Sn}_{0.9}\text{Co}_{0.1}\text{O}_{2-\delta}$  film.



## 2.4 The Autocombustion Technique

Synthesis routes play a crucial role in preparing the target product and determining its properties. The synthesis of the metal oxide materials is achieved either by solid state reaction or by wet chemical methods. Traditionally, multi-component ceramics have been prepared by solid state methods, which involved physical mixing of hydroxide, oxide, carbonate, nitrate or sulphate raw materials followed by high temperature treatment, approximately 1373 K, for a lengthy period to enable the formation of the target compounds. It is well known that the solid state reaction needs a high calcination temperature and leads to uncontrollable large grain growth, segregation of dopant oxides and possible loss of stoichiometry due to volatilization of reactants at high temperatures. Furthermore, this method has inherent disadvantages as chemical inhomogeneity, coarse grain sizes and entrance of impurities during the milling process.

The wet-chemical processes are also advantageous over a conventional solid-state synthesis in terms of better compositional homogeneity and purity of the final product especially

in case of electro-ceramics for which electrical functions are governed by small amounts of dopants. Usually, the techniques start from the preparation of a precursor solution, in which the ions are well mixed on a molecular scale. The solid precursors may be amorphous or crystalline single phases with a homogeneous or inhomogeneous composition or physical mixtures of such phases that are high value-added inorganic materials with controlled microstructure and properties. Several physical methods have been developed for the preparation of metal oxide nanocrystallines including tin dioxide powders, involving spray pyrolysis [63], sol-gel [64], co-precipitation [65] and hydrothermal [66] methods. However, these methods are quite involved; requirement of long processing time, costly chemicals and special equipment. The co-precipitation is generally preferred because it is easier to be implemented and it has a relatively lower cost compared with the others, but the contaminations of chloride ions cannot be avoided [67], affecting the surface and the electrical properties.

Also when one wants to homogeneously dope a metal ion (2-5%) into the oxide matrix, one has to disperse the dopant using tedious procedures. Therefore, there is a need to look for an alternative to these methods and practices. Recently, several variants of self-sustaining combustion synthesis have been developed. The novel autocombustion method can be initiated at low temperatures, self-propagating and gas producing. The autocombustion technique has recently attracted much attention due to its simplicity and capability to deliver the nanocrystalline powders in a surprisingly short time with improved characteristic such as high surface area and better sinterability. This method has the advantage of inexpensive precursor, facile preparation method, low annealing or calcination temperature, energy-efficiency and a resulting nanosized particle [68]. Moreover, this process has a control over stoichiometry, purity of the final product and excellent chemical homogeneity due to the aqueous solution mixture of initial reagents and, as a result, favors the production of desired phases or ceramics [69]. It enables the preparation of a variety of materials such as intermetallic compounds, metal carbides, oxides, borides and nitrides and is easy to dope desired amount of impurity ions. Tin oxide nanocrystalline powders prepared from this method are also reported [70-72].

Autocombustion is a novel way and a unique combination of the combustion process and the chemical gelation process. A solution containing the oxidizing metal nitrates and fuels such as citric acid, glycine, hydrazine and urea is heated to form a polymeric gel followed by a combustion process due to an exothermic redox reaction between fuel and nitrate anions.

The organic compound acts as fuel for the combustion reaction, and the gelling agent fixes the metallic ion stoichiometry and prevents selective precipitation as the solution is concentrated. Only when the oxidizer and the fuel are intimately mixed in a fixed proportion, they initiate an exothermic chemical reaction that generates plenty of heat. When the heat evolved is more than the heat required for the reaction, the system becomes self-sustained. The precursor powder is further calcined to form the required crystalline ceramic phase. Citric acid is more widely used, since it not only functions as a reductant/fuel agent, but also a chelating agent. The molar ratio of fuel to nitrates in the initial mixture imposes a great influence on calcinations condition and the subsequent characteristics of the synthesized crystallites. Generally, in combustion synthesis large volume of gases are generated during the combustion reaction in a short interval of time which makes the product foamy and soft agglomerate of fine particles. Therefore the product obtained in combustion synthesis can be easily brought down to fine particles by minimum mechanical milling.



## CHAPTER 3

### EXPERIMENTAL TECHNIQUES

In this study, transition metal doped  $\text{SnO}_2$  nanoparticle samples ( $\text{Sn}_{1-x}\text{TM}_x\text{O}_{2-\delta}$ , where  $\text{TM} = \text{Cr}, \text{Co}$  with  $x \leq 0.015$  and  $\text{Fe}$  with  $x \leq 0.30$ ) were synthesized by the autocombustion technique. The autocombustion method can be initiated at a low temperature. This method was a simple, fast and energetically attractive method that can be adopted for the fine bulk production of high purity metal oxides. Moreover, the control over stoichiometry, homogeneity and purity was applied. The desired amount of impurity ions were easily doped in samples.

The fine powder samples were characterized by powder X-ray diffraction (XRD) technique. The diffraction patterns were then analyzed with the Rietveld method [73-74] using the FULLPROF program [75]. Crystallite sizes of the particles were also obtained from diffractograms using both Scherrer's equation and Williamson-Hall Plot (WHP) method. Transmission electron microscopy (TEM) was employed to study the microstructures. Band gap energies that explained conduction property of the compounds were obtained from UV-VIS-NIR-Spectroscopy technique. Moreover, the magnetic properties were investigated by using vibrating sample magnetometer (VSM) at a room temperature.

In the first section in this Chapter (section 3.1), a schematic diagram describing the experimental procedures was presented. Section 3.2 described the preparation of the  $\text{Sn}_{1-x}\text{TM}_x\text{O}_{2-\delta}$  nanoparticle samples by the autocombustion method. The physical characterization methods including structural, optical measurement and microstructure were described in section 3.3. Finally, the magnetic measurement procedure was detailed.

### 3.1 Schematic Diagram of the Experiment

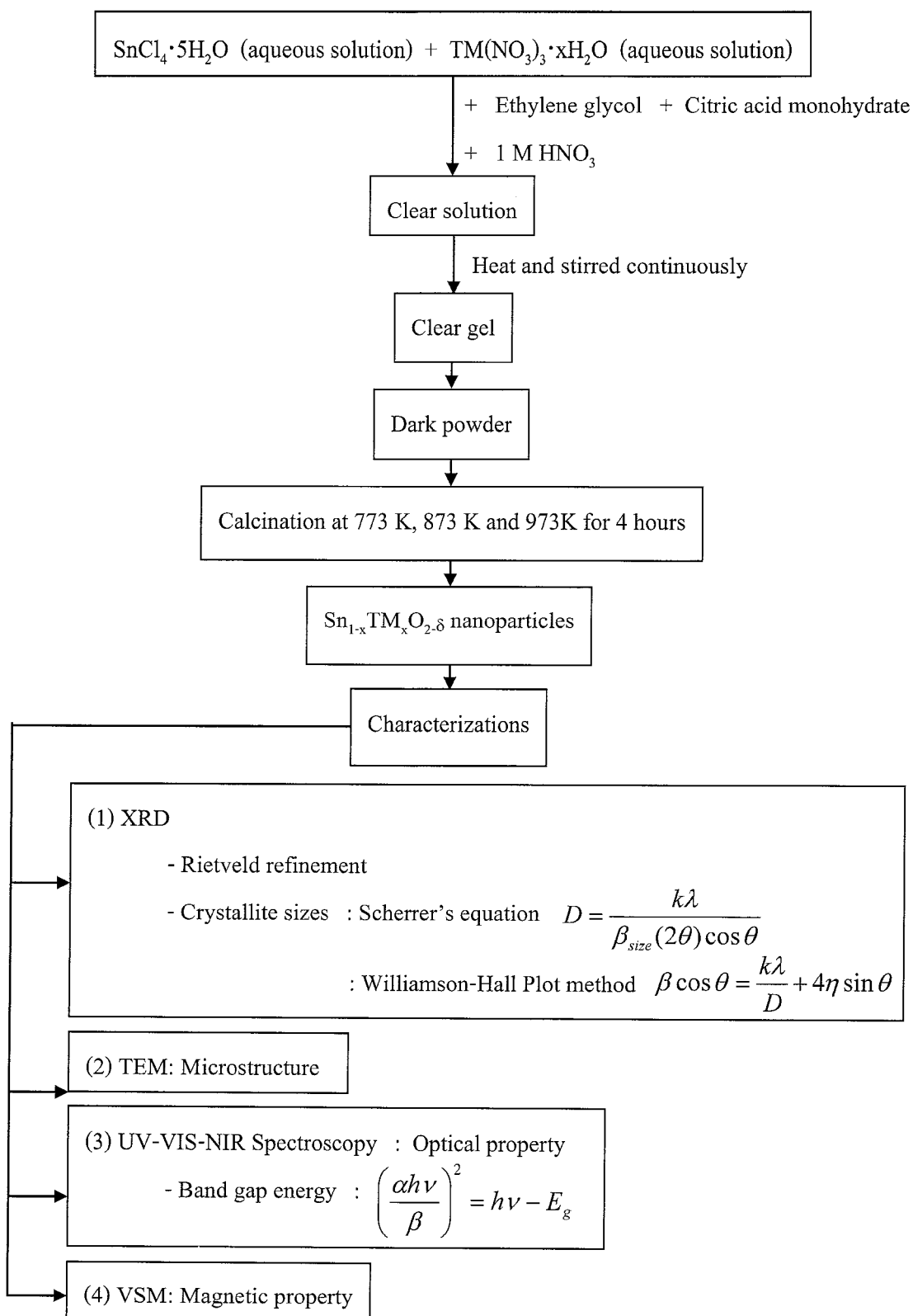


**Figure 3.1** Schematic diagram of the experimental process in this study.

### 3.2 Nanoparticles Preparation

The nanoparticle powders  $\text{Sn}_{1-x}\text{TM}_x\text{O}_{2.8}$  (where TM = Cr and Co with  $x \leq 0.015$ , and Fe with  $x \leq 0.300$ ) were synthesized using the autocombustion method. The starting materials were tin(IV) chloride pentahydrate ( $\text{SnCl}_4 \cdot 5\text{H}_2\text{O}$ , Acros organics, 98%), Cobalt(III) nitrate hexahydrate ( $\text{Co}(\text{NO}_3)_3 \cdot 6\text{H}_2\text{O}$ , Fluka, 99%), Chromium(III) nitrate nonahydrate ( $\text{Cr}(\text{NO}_3)_3 \cdot 9\text{H}_2\text{O}$ , Fluka, 97%), Ferric(III) nitrate nonahydrate ( $\text{Fe}(\text{NO}_3)_3 \cdot 9\text{H}_2\text{O}$ , Fluka, 99%), citric acid monohydrate ( $\text{HOC}(\text{COOH})\text{CH}_2\text{COOH} \cdot \text{H}_2\text{O}$ , Fluka, 99%), ethylene glycol ( $\text{HOCH}_2\text{CH}_2\text{OH}$ , Fluka, 98%) and dilute nitric acid (1 M  $\text{HNO}_3$ , BDH, 69%).

The concrete process was carried out as follows: the appropriate proportion of  $\text{SnCl}_4 \cdot 5\text{H}_2\text{O}$  and metal nitrate salts were first completely dissolved in deionized water to be stock solutions with concentration of 0.4 M and 0.02 M, respectively. These stock solutions were then mixed to form a homogeneous transparent aqueous solution with the stoichiometric ratio of tin and transition metal ions into 300 mL of the mixture of 60% citric acid monohydrate and 40% ethylene glycol aqueous solution. Citric acid monohydrate was added into the prepared aqueous solution to be chelating agent. Dilute nitric acid was then slowly added to this mixed solution to convert all the metal ions into respective nitrates and enhance the combustion process. During this procedure, the aqueous solution was continuously constant stirred in order to homogenize the solution. The solution was then evaporated on a hot plate under constant stirring and kept at a temperature of around 393 K. After the water was completely removed slowly, the solution converted into a black gel. The gel was subsequently swelled into foam and simultaneously burnt in a strong self-propagating combustion reaction to give a dark fine powder. The entire combustion process was over after a few seconds. To complete decomposition of the organic residue, the resulting black ashes were then calcined at three different temperatures (773, 873 and 973 K) for 4 hrs in an ambient atmosphere (Furnace Model CWF 1200, CARBOLITE). The final fine powder was then ground and stored for characterization.

### 3.3 Physical Characterization

#### 3.3.1 X-ray Diffraction (XRD) Measurements

Desired phase formation in the nanoparticle samples was confirmed by the room temperature powder XRD measurement of the well ground powder sample using a Philips X'Pert-MDP X-ray powder Diffractometer (PW 3040/60) using CuK $\alpha$  radiations ( $\lambda_{\text{CuK}\alpha_1} = 1.54056 \text{ \AA}$  and  $\lambda_{\text{CuK}\alpha_2} = 1.54439 \text{ \AA}$ ) with Ni filter. The measurements consisted usually of recording the X-ray diffraction intensities at  $2\theta$  angle from  $20^\circ$  to  $100^\circ$  with a step scan of  $0.02^\circ$  and a counting time of 8 seconds per a step. The diffractometer was operated at 40 kV and 35 mA.

##### 3.3.1.1 Structure Refinement

The X-ray diffraction patterns were then analyzed with the Rietveld method [73-74] using the FULLPROF program [75]. The initial data of  $\text{Sn}_{1-x}\text{TM}_x\text{O}_2$  for analyzing were the tetragonal rutile structure of  $\text{SnO}_2$  (JCPDS File No. 41-1445) with  $a = b = 4.738 \text{ \AA}$ , and  $c = 3.187 \text{ \AA}$ . Space group was P42/mnm (No. 136).

The Rietveld refinement was whole-pattern-fitting structure refinement of diffraction data using a least-squares method. The least-squares procedure used the Newton-Raphson or Marquardt algorithm to minimize the quantity,  $S$ , defined as:

$$S = \sum_i w_i (y_i(\text{obs}) - y_i(\text{calc}))^2 \quad (3.1)$$

where  $y_i(\text{obs})$  was the observed intensity.  $y_i(\text{calc})$  was the net intensity calculated at point  $i$  in the pattern.  $w_i$  was the weight quality which equal to  $1/y_i(\text{obs})$ .

The basis of the Rietveld method was calculated by using the following equation;

$$y_i(\text{calc}) = y_i(\text{bgnd}) + \sum_p \sum_{k=k_1^p}^{k_2^p} G_{ik}^p I_k \quad (3.2)$$

where,  $y_i(\text{bgnd})$  was the background intensity calculated at point  $i$  in the pattern.  $G_{ik}$  was peak profile function of phase  $p$ . The analytic functions including a pseudo-Voigt and modified

pseudo-Voigt have been usefully described XRD peak shape [76].  $I_k$  was the intensity of the  $k$  Bragg reflection and was given by expression

$$I_k = SM_k L_k |F_k|^2 P_k A_k E_k \quad (3.3)$$

where,  $S$  was the scale factor,  $M_k$  was the multiplicity,  $L_k$  was the Lorentz-polarization factor and  $F_k$  was the structure factor which

$$F_k = \sum_{j=1} f_j \exp[2\pi i(h_k^t r_j - h_k^t B_j h_k)] \quad (3.4)$$

where  $f_j$  was the scattering factor of atom  $j$ , and  $h_k$ ,  $r_j$  and  $B_j$  were matrices representing the Miller indices, atomic coordinates and anisotropic thermal vibration parameters, respectively, and the superscript  $j$  indicated matrix transposition. The factor  $P_k$  was intended to describe the effect of preferred orientation. The factors  $A_k$  and  $E_k$  were the adsorption and extinction correction, respectively.

From Equation (3.2),  $y_i(calc)$  was calculated using the following information:

- (1) Lattice parameters to determine peak positions;
- (2) Atomic positions and displacement parameters to determine peak intensities;
- (3)  $2\theta$ -dependent analytic functions to describe the peak shape and peak widths;
- (4) A description of the background intensity

In Rietveld refinement, the calculated powder diffraction pattern was compared, point by point, with the experimental powder diffraction pattern, and selected parameters defining the structural model and describing the profile were adjusted by least-squares method to give the best fit. Several criteria can be used to assess the agreement between the experimental and calculated diffraction patterns. Definitions of the most commonly used agreement factors [77] were

Weighted Profile Factor:

$$R_{wp} = 100 \left( \frac{\sum_i w_i [y_i(obs) - y_i(calc)]^2}{\sum_i w_i [y_i(obs)]^2} \right) \quad (3.5)$$

Ideally, the final  $R_{wp}$  value should approach the statistically the expected  $R$  ( $R_{exp}$ ) value:

$$R_{exp} = 100 \left[ \frac{(N - P)}{\sum w_i y_i(obs)} \right]^{\frac{1}{2}} \quad (3.6)$$

Profile Factor:

$$R_p = 100 \frac{\sum_i |y_i(obs) - y_i(calc)|}{\sum_i y_i(obs)} \quad (3.7)$$

Bragg Factor:

$$R_B = 100 \frac{\sum_h |I_{obs,h} - I_{calc,h}|}{\sum_h |I_{obs,h}|} \quad (3.8)$$

Crystallographic  $R_F$ -Factor:

$$R_F = 100 \frac{\sum_h |F_{obs,h} - F_{calc,h}|}{\sum_h |F_{obs,h}|} \quad (3.9)$$

Goodness of Fit indicator or chi-square ( $\chi^2$ ):

$$\chi^2 = \frac{\sum_i w_i [y_i(obs) - y_i(calc)]^2}{N - P} \quad (3.10)$$

where  $N$  was the number of data points in the experimental powder diffraction pattern and  $P$  was the number of parameters in the refinement. A  $\chi^2$  factor greater than about 2.25 was a strong indication of an inadequate model or a false minimum. A value of  $\chi^2$  factor less than 1.0,

however, was an indicator not of an extremely high quality refinement but of a model that contained more parameters than can be justified by the quality of the data.

Durbin-Watson statistic (DW-stat):

$$\text{DW-stat} = \frac{\sum_{i=2}^N \Delta y_i - \Delta y_{i-1}}{\Delta \left( \prod_{i=1}^N y_i \right)^2} \quad (3.11)$$

where  $\Delta y_i = y_i(\text{obs}) - y_i(\text{calc})$ .

The DW-stat value was used to indicate the quality of the fit of the calculated Bragg reflection profile functions to the actual observed profiles. The ideal value for the DW-stat was 2.0.

The important thing in refinement was to obtain a physically meaningful result rather than the lowest R factors. There were now many academic programs available free for carrying out Rietveld refinement, including FULLPROF [75], GSAS [78-79], DBW [80-81], RIETAN [82] etc.

In this study, the FULLPROF program was used to analyze and refine the XRD data. The pseudo-Voigt function was chosen to generate the line shape of the diffraction peaks. In the Rietveld refinement, the following parameters were refined: scale factors (S), background points, zero-points error, unit cell parameters, atomic positions, pseudo-Voigt corrected for asymmetry parameters and overall thermal displacement (*B*) factors.

### 3.3.1.2 Crystallite Size Determination

A perfect crystal extended in all directions to infinity, so it can say that no crystal was perfect due to its limited sizes. Such a deviation from perfect crystallinity led to broadening of the diffraction peak. However, this type of peak broadening was negligible when the crystallite size was larger than 200 nm. Crystallite size was a measure of the size of a coherently diffracting domain. Due to the presence of polycrystalline diffracting domain aggregates, crystallite size may not be the same thing as particle size.

### Scherrer's Equation

If the crystallites of the powder are very small the peaks of the pattern will be broaden. From the broadening it was possible to determine an average crystallite size by Debye-Scherrer in 1918 [83-84], which used the Scherrer equation as :

$$D = \frac{k\lambda}{\beta_{size}(2\theta)\cos\theta} \quad (3.12)$$

where  $D$  was the averaged dimension of crystallites.  $k$  was the Scherrer constant, somewhat arbitrary value that falls in the range of 0.89-1.39 (it was usually assumed to be 0.89 for sphere crystal).  $\lambda$  was the wavelength of the X-ray radiation.  $\beta_{size}(2\theta)$  was the integral breadth of a full width at half maximum (FWHM) of each peak in radians.  $\theta$  was the position of the maximum of diffraction.

### Williamson-Hall Plot (WHP) method

In 1953 Williamson and Hall [85] proposed a simplified integral breadth method for crystallite size and lattice strain contributions to line broadening as a function of  $2\theta$ . The lattice strain in the material also caused broadening of the diffraction peaks, which can be represented by the relationship

$$\beta_{strain} = 4\eta \tan \theta \quad (3.13)$$

where  $\beta_{strain}$  was the integral breadth of the lattice strain and  $\eta$  was the strain in the material.

The width,  $\beta$ , of the diffraction peak after subtracting the instrumental effect can be considered as the sum of width due to small crystallite size and lattice strain:

$$\beta = \beta_{size} + \beta_{strain} \quad (3.14)$$

and from Equation (3.12) and (3.13) they got

$$\beta = \frac{k\lambda}{D \cos \theta} + 4\eta \tan \theta \quad (3.15)$$



Multiplying Equation (3.15) by  $\cos \theta$ , they got

$$\beta \cos \theta = \frac{k\lambda}{D} + 4\eta \sin \theta \quad (3.16)$$

The Williamson-Hall plot of  $\beta \cos \theta$  (y-axis) against  $4\eta \sin \theta$  (x-axis) which get a straight line with slope  $4\eta$  and intercept  $k\lambda/D$ . The y-intercept can be used to calculate crystallite size ( $\langle D \rangle$ ) by using the appropriate values of  $k$  (generally taken to be = 1.0) and  $\lambda$ , while strain can be calculated from the slope.

Broadening of X-ray diffraction peak was easily apparent in patterns obtained with a diffractometer. There were three factors to arise the broadening of diffraction peaks; instrumental effects, crystallite size and lattice strain. The broadening was evaluated by measuring the width  $\beta$  (in radians), at an intensity equal to half the minimum intensity or full width at half maximum (FWHM). If the observed X-ray peak had a width  $\beta_o$ , and the width due to instrument effects was  $\beta_i$ , then the remaining width  $\beta_r$  was due to the combined effects of crystallite size and lattice strain:

$$\beta_r = \beta_o - \beta_i \quad (3.17)$$

This expression was true only when the peak has a Lorentzian profile [86]. However, if it had a Gaussian profile, a better expression was

$$\beta_r^2 = \beta_o^2 - \beta_i^2 \quad (3.18)$$

In the absence of clear-cut evidence for the exact nature of the peak and in this analysis, the geometric mean was used to get a more nearly correct expression:

$$\beta_r = \sqrt{(\beta_o - \beta_i) \sqrt{(\beta_o^2 - \beta_i^2)}} \quad (3.19)$$

In this work, however, Equation (3.19) was used to subtract the instrumental broadening from the observed broadening.

### 3.3.2 Optical Measurement

The absorption edge was defined as the transition between the strong short-wavelength and the weak long-wavelength absorption in the spectrum of a solid, generally a semiconductor. The spectral position of this edge was determined by the energy separation between the valence and conduction bands of the material. In the case of transparent solids, the absorption edge can be measured using transmittance techniques. Diffuse reflectance measurements provided a more appropriate means of measurement for powdered materials. The present study aimed to directly measure the absorption edge and band-gap energies of these nanostructured materials, based on the onset of UV-Vis diffuse reflectance spectra of the powdered materials.

The diffuse reflectance spectra of the nanoparticle samples were performed at room temperature with a UV-3101PC UV-VIS-NIR spectrophotometer (SHIMADZU, Japan) at Department of Chemistry, Faculty of Science, Khon Kaen University. These diffuse reflection spectra were recorded at the wavelength from 200 nm to 900 nm. The powder samples were analyzed using the standard sampling cup. In each instance, the cup was overfilled using the sample by running along the top surface of the sample cup. Moreover, the absorption spectrum could be calculated from the measured reflection spectrum by a mathematical operation called the Kramers-Kronig transformation.

#### 3.3.2.1 Calculation of Band Gap Energy ( $E_g$ )

Even with all these sample preparation practices, the raw diffuse reflectance spectra would appear different from its transmission equivalent (stronger than expected absorption from weak IR bands). A Kubelka-Munk conversion can be applied to a diffuse reflectance spectrum to compensate for these differences.

The Kubelka-Munk equation was expressed as follows:

$$f(R) = \frac{(1-R)^2}{2R} = \frac{k}{s} \quad (3.20)$$

where  $R$  was the absolute reflectance of the sampled layer,  $k$  was the molar absorption coefficient and  $s$  was the scattering coefficient.

Direct band gap semiconductor mean that the minimum of the conduction band laid directly above the maximum of the valence band in momentum space. The absorption coefficient for direct gap absorption varied as the square-root of energy above the band edge:

$$\alpha_{\text{direct gap}}(h\nu) = \beta(h\nu - E_g)^{1/2} \quad \text{or} \quad \left(\frac{\alpha h\nu}{\beta}\right)^2 = h\nu - E_g \quad (3.21)$$

where  $\alpha$  was the absorption coefficient,  $h\nu$  was the energy of incident photons and  $\beta$  was the constant.

Instead the Kubelka-Munk function from Equation (3.20) as the molar absorption coefficient,  $\alpha$  in Equation (3.21)

$$(f(R)h\nu)^2 = \left(\frac{(1-R)^2 h\nu}{(2R)}\right)^2 = h\nu - E_g \quad (3.23)$$

The plot of  $(f(R)h\nu)^2$  (y-axis) versus the photon energy,  $h\nu$  (x-axis) got a straight line in some region in vicinity of absorption threshold.  $E_g$  was the x-intercept (or  $(f(R)h\nu)^2 = 0$ ) of the straight line.

### 3.3.3 Microstructure

The surface morphology and microstructures of the powder samples were observed by transmission electron microscopy (TEM) using a JEOL JSM 2010, Japan transmission electron microscope at the Science and Technology Service Center, Chiang Mai University (STSC-CMU). The TEM was operated at 200 kV.

## 3.4 Magnetic Measurement

Magnetic measurements were carried out on a vibrating sample magnetometer, VSM (VSM 7403, LakeShore, USA) at Department of Chemistry, Faculty of Science, Khon Kaen University. All samples were prepared by weighing ~40 mg of materials into an acid washed Teflon sample holder. The samples were fixed to a small sample holder located at the end of a sample rod mounted in an electromechanical transducer. The transducer was driven by a power

amplifier which was driven by an oscillator. So, the samples were vibrated along the Z axis perpendicular to the magnetizing field. In addition, an empty sample holder was measured the signal to be the background for subtraction from the sample signal.

The magnetization as function of the applied magnetic field, in order to generate hysteresis loop, were measured at the desired temperatures starting from zero field up to 5 kOe down to -5 kOe by using an oscillating magnetic field. Ferromagnetic materials had non-linear initial magnetization curves, as the changing magnetization with applied field was due to a change in the magnetic domain structure. These materials also showed hysteresis and the magnetization did not return to zero after the application of a magnetic field. A typical hysteresis loop of ferromagnet was displayed Figure 3.2. The various parameters could be determined from it. From the first quadrant the saturation magnetization ( $M_s$ ) could be measured. The field that was produced by the magnet after the magnetizing field has been removed is called the remanence magnetization ( $M_r$ ). The reverse field required to bring the induction to zero was called the coercive field ( $H_c$ ). In addition, the hysteresis shape could also indicate the magnetic interaction in the materials.

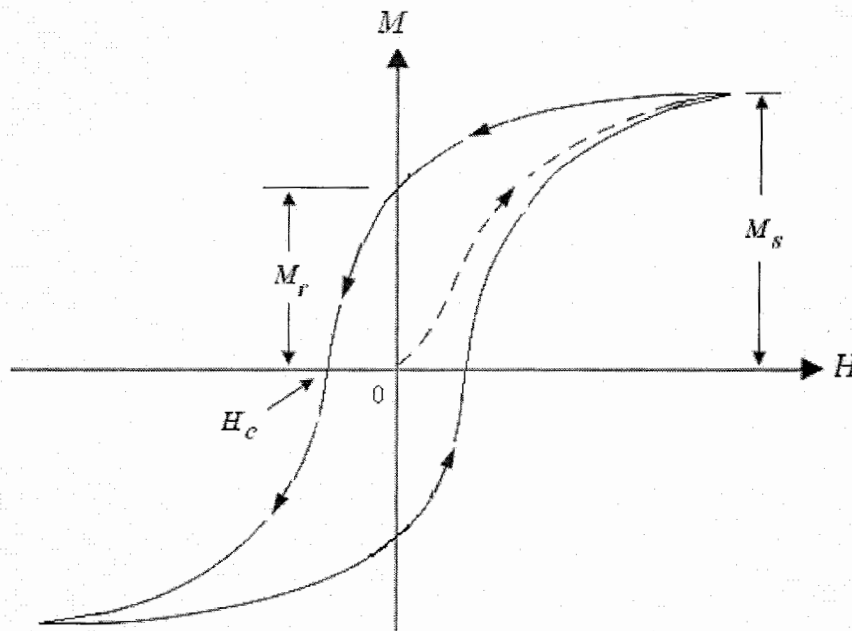


**Figure 3.2** A typical hysteresis loop for ferromagnetic materials.

## CHAPTER 4

### RESULTS AND DISCUSSION

The transition metals doped  $\text{SnO}_2$  nanoparticles were synthesized by the autocombustion technique with three different calcined temperatures (773, 873 and 973 K) for 4 hours. The fine powder samples were then characterized in several techniques. The structures of the samples were obtained from the Rietveld refinement of XRD patterns. The microstructures, the optical properties, and the magnetic properties including of magnetization of these nanoparticles were reported. This Chapter was divided into three sections. In the first section, the results from the Cr-doped  $\text{SnO}_2$  samples ( $\text{Sn}_{1-x}\text{Cr}_x\text{O}_{2.8}$  with  $x \leq 0.015$ ) were given. Following, the properties of Co-doped  $\text{SnO}_2$  samples ( $\text{Sn}_{1-x}\text{Co}_x\text{O}_{2.8}$  with  $x \leq 0.015$ ) were detailed in section 4.2. The last section covered the characterization of Fe-doped  $\text{SnO}_2$  samples ( $\text{Sn}_{1-x}\text{Fe}_x\text{O}_{2.8}$  with  $x \leq 0.30$ ).

#### 4.1 Chromium-doped Tin Oxide ( $\text{Sn}_{1-x}\text{Cr}_x\text{O}_{2.8}$ )

##### 4.1.1 X-ray Diffraction Studies

Powder X-ray diffraction (XRD) patterns of the  $\text{Sn}_{1-x}\text{Cr}_x\text{O}_{2.8}$  samples with  $x \leq 0.015$  calcined at 773 K were shown in Figure 4.1. X-ray diffraction patterns revealed that the structures of all samples were rutile-type cassiterite (tetragonal) phase of  $\text{SnO}_2$ . No additional peaks were observed due to the absence of any impurity. The intensity of XRD peaks corresponding to the (110) of the  $\text{Sn}_{1-x}\text{Cr}_x\text{O}_{2.8}$  samples, with the varied calcined temperatures, were shown in Figure 4.2. The XRD intensities of these samples were less than those of pure  $\text{SnO}_2$ . The intensities further decreased with increasing Cr concentration. The results implied that the  $\text{Sn}^{4+}$  ions were replaced by Cr ions in the lattice of  $\text{SnO}_2$ . Due to the atomic scattering factor of Cr was less than Sn [87]. All the samples had very broad XRD peaks due to their nanocrystalline behaviors.

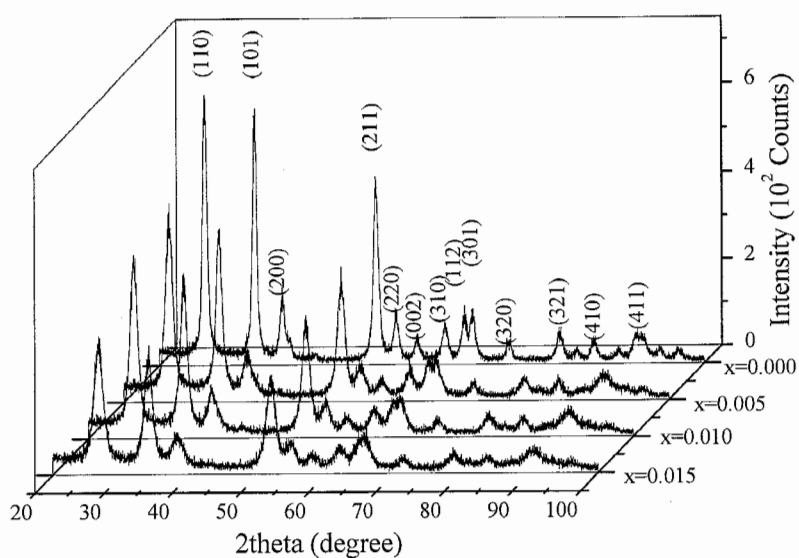


**Figure 4.1** X-ray Diffraction patterns of the  $\text{Sn}_{1-x}\text{Cr}_x\text{O}_{2.δ}$  ( $x \leq 0.015$ ) samples calcined at 773 K.

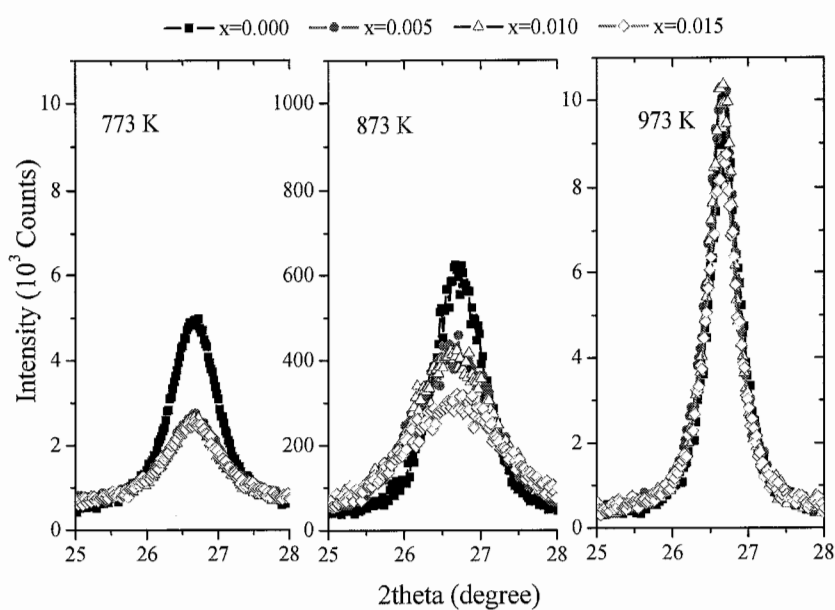


**Figure 4.2** Changes in the intensity of plane (110) of the  $\text{Sn}_{1-x}\text{Cr}_x\text{O}_{2.δ}$  samples calcined at 773, 873 and 973 K.

The XRD patterns of the  $\text{Sn}_{0.985}\text{Cr}_{0.015}\text{O}_{2-\delta}$  samples with vary calcined temperatures were shown in Figure 4.3. It was found that the X-ray intensities increased with increasing calcined temperature. The result indicated that crystallinity of the sample was increased as increasing calcination temperatures.

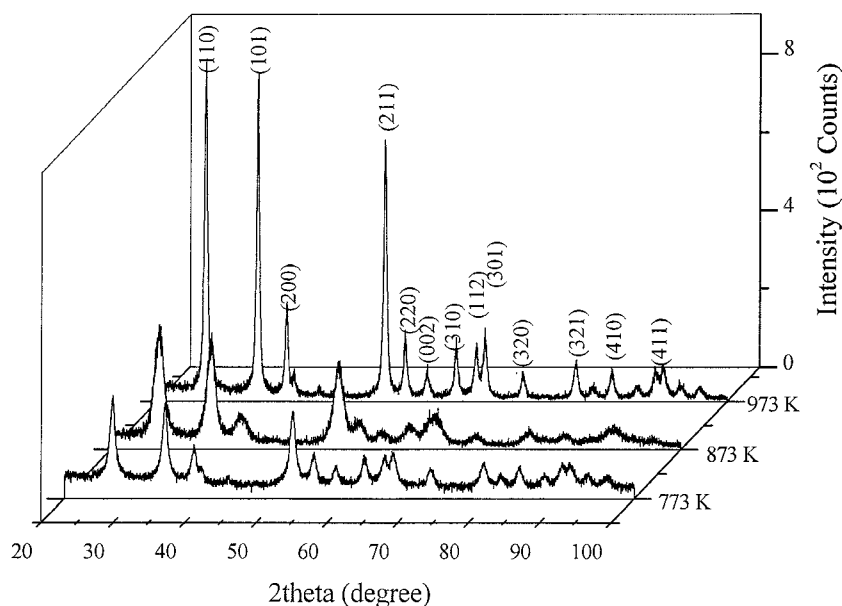


**Figure 4.3** X-ray Diffraction patterns of the  $\text{Sn}_{0.985}\text{Cr}_{0.015}\text{O}_{2-\delta}$  samples with the variation of calcined temperatures.

#### 4.1.2 The Rietveld Refinement

The Rietveld refinement of the  $\text{Sn}_{1-x}\text{Cr}_x\text{O}_{2-\delta}$  samples with  $x \leq 0.015$  calcined at 973 K were shown in Figure 4.4. The Rietveld profile analysis revealed the expected tetragonal rutile structure of  $\text{SnO}_2$  with  $P4_2/mnm$  symmetry. No additional phases were observed. The corresponding lattice parameters and the factors obtained from the Rietveld refinement of  $\text{Sn}_{1-x}\text{Cr}_x\text{O}_{2-\delta}$  samples were summarized in Table 4.1.

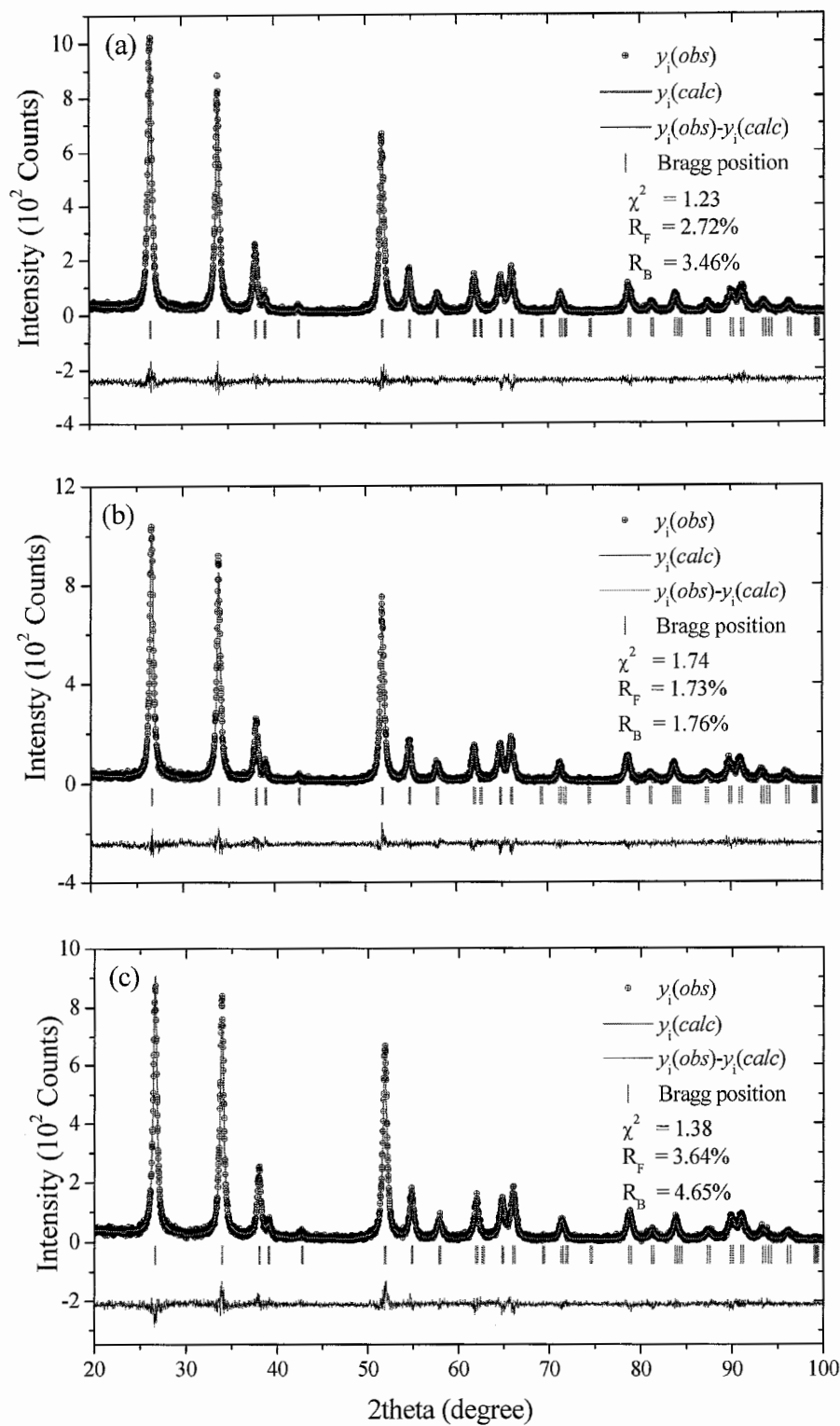


**Figure 4.4** X-ray diffractograms of (a)  $\text{Sn}_{0.995}\text{Cr}_{0.005}\text{O}_{2.8}$  (b)  $\text{Sn}_{0.990}\text{Cr}_{0.010}\text{O}_{2.8}$  and (c)  $\text{Sn}_{0.985}\text{Cr}_{0.015}\text{O}_{2.8}$  calcined at 973 K. Data points were indicated by solid cycles, while the calculated patterns were shown as a continuous line. The positions of the reflections were indicated with the vertical lines below the patterns.



**Table 4.1** The Rietveld refinement crystallographic data of the  $\text{Sn}_{1-x}\text{Cr}_x\text{O}_{2.8}$  ( $x = 0.005, 0.010$  and  $0.015$ ) samples calcined at 773, 873 and 973 K. The space group P42/mmm was used for all samples. Sn/Cr was occupied at (0, 0, 0) and  $\text{O}^{2-}$  was occupied at ( $x, y, 0$ ) while  $x$  was equal to  $y$ . The numbers in the parenthesis were estimated standard deviations to the last significant digit.

| Compound                           | $\text{Sn}_{0.995}\text{Cr}_{0.005}\text{O}_{2.8}$ |           |           | $\text{Sn}_{0.990}\text{Cr}_{0.010}\text{O}_{2.8}$ |           |           | $\text{Sn}_{0.985}\text{Cr}_{0.015}\text{O}_{2.8}$ |           |           |
|------------------------------------|--|-----------|-----------|--|-----------|-----------|--|-----------|-----------|
| Calced Temp. (K)                   | 773  | 873       | 973       | 773  | 873       | 973       | 773  | 873       | 973       |
| Parameters                         |  |           |           |  |           |           |  |           |           |
| $a = b$ (Å)                        | 4.7400(8)  | 4.7388(6) | 4.7394(6) | 4.7366(3)  | 4.7350(3) | 4.7349(1) | 4.7366(2)  | 4.7359(2) | 4.7354(2) |
| $c$ (Å)                            | 3.1898(6)  | 3.1891(5) | 3.1897(5) | 3.1866(2)  | 3.1854(2) | 3.1846(1) | 3.1861(2)  | 3.1857(2) | 3.1852(2) |
| Volume (Å <sup>3</sup> )           | 71.67(1)   | 71.61(2)  | 71.65(2)  | 71.49(1)   | 71.42(1)  | 71.40(1)  | 71.48(1)   | 71.45(1)  | 71.42(1)  |
| $\text{O}^{2-}$ position ( $x$ )   | 0.304(1)   | 0.304(1)  | 0.304(1)  | 0.304(1)   | 0.304(1)  | 0.304(1)  | 0.305(1)   | 0.302(1)  | 0.300(1)  |
| $B_{\text{iso}}$ (Å <sup>2</sup> ) | 0.24(1)  | 0.23(1)   | 0.23(1)   | 0.23(1)  | 0.24(1)   | 0.23(1)   | 0.23(1)  | 0.24(1)   | 0.23(1)   |
| $R_p$ (%)                          | 16.2   | 14.9      | 15.3      | 14.1   | 14.7      | 8.51      | 13.2   | 13.4      | 14.9      |
| $R_{\text{wp}}$ (%)                | 20.9   | 19.8      | 20.0      | 19.1   | 20.0      | 11.1      | 18.7   | 18.9      | 19.6      |
| $R_{\text{exp}}$ (%)               | 18.96  | 17.97     | 18.03     | 17.63  | 18.12     | 8.86      | 17.07  | 16.98     | 17.44     |
| $R_B$ (%)                          | 3.57   | 3.35      | 3.46      | 3.08   | 3.16      | 1.76      | 3.05   | 3.37      | 4.65      |
| $R_F$ (%)                          | 2.61   | 2.66      | 2.72      | 2.91   | 3.07      | 1.73      | 3.18   | 3.07      | 3.64      |
| $\chi^2$                           | 1.21   | 1.21      | 1.23      | 1.21   | 1.25      | 1.74      | 1.33   | 1.44      | 1.38      |
| DW-stat                            | 1.79   | 1.72      | 1.70      | 1.78   | 1.85      | 1.32      | 1.88   | 1.97      | 1.78      |

No appreciable changes were detected in tetragonal unit cell parameters in the  $\text{Sn}_{1-x}\text{Cr}_x\text{O}_{2-\delta}$  samples calcined at 773 K, shown in Table 4.1. However, the lattice parameter  $a$  was shown a slightly decrease with increasing Cr concentrations. It was in agreement with the replacement of a larger radius of the  $\text{Sn}^{4+}$  ( $\sim 0.69$  Å) by the  $\text{Cr}^{3+}$  ( $\sim 0.62$  Å) or  $\text{Cr}^{4+}$  ( $\sim 0.55$  Å) [88] for octahedral coordination. This result indicated that solid solutions with a rutile structure were formed in agreement with decreasing in XRD intensities results, shown in Figure 4.2. Such a rapid contraction of the lattice could be understood qualitatively considering the sizes of the ions and their local coordinations. Therefore, the substitutions of  $\text{Sn}^{4+}$  ions with Cr ions was expected to reduce the interatomic spacing significantly, justifying the initial contraction of the lattice. On the other hands, the lattice parameters  $a$  and  $c$  for the samples calcined at 873 and 973 K were increased with increasing Cr dopant. This result was corresponded to Punnoose *et. al.* [56], the lattice parameters  $a$  decreased with increasing preparation temperatures from the 623 to 873 K range, these trends were reversed above preparation temperature of 873 K. This change occurred due to change in the oxygen stoichiometry. As a result, all samples were be subscripted the symbol,  $\delta$  at oxygen atom for the oxygen vacancy.

#### 4.1.3 Crystallite Sizes

The average particle size ( $\langle D \rangle$  or  $D$ ) was calculated from the fine XRD line broadening, by using the usual Scherrer's equation [ $D = k\lambda/\beta\cos\theta$ ] and the Williamson-Hall Plot (WHP) method [ $\beta\cos\theta = k\lambda/D + 4\eta\sin\theta$ ]. The Full Width at Half Maximum (FWHM),  $\beta$  was calculated by using both the Lorentian profile and the Guassian profile. The  $\beta$  was estimated using the measured peaks width  $\beta_o$  and the instrumental width  $\beta_i$  [ $\beta = \sqrt{(\beta_o - \beta_i)^2 + \beta_i^2}$ ].  $\beta_o$  was the FWHM obtained from the planes (110), (101), (200), (211) and (220).  $\beta_i$  was the FWHM due to instrument effects which were obtained from commercial  $\text{SnO}_2$  which calcined at 1,273 K for 3 hours. Calculation of the crystallite sizes then was performed, for example, see Appendix IV.

### Crystallite size calculated by Scherrer's Equation

The crystallite sizes of the  $\text{Sn}_{1-x}\text{Cr}_x\text{O}_{2-\delta}$  ( $x \leq 0.015$ ) samples calcined at 773, 873 and 973 K were calculated by Scherrer's relation. The dependence of the particle size on the Cr dopant concentration with the various calcination temperatures was shown in Figure 4.5. The crystallite sizes of the samples were in the range of 5-16 nm. The crystallite sizes increased as increasing calcination temperatures. Those results indicated that the agglomeration of powders was appeared during growing crystals. On increasing of the Cr concentration, the crystallite sizes were a slightly change. This result indicated that the amount of doped chromium affected a little bit in crystal size of the nanoparticles.

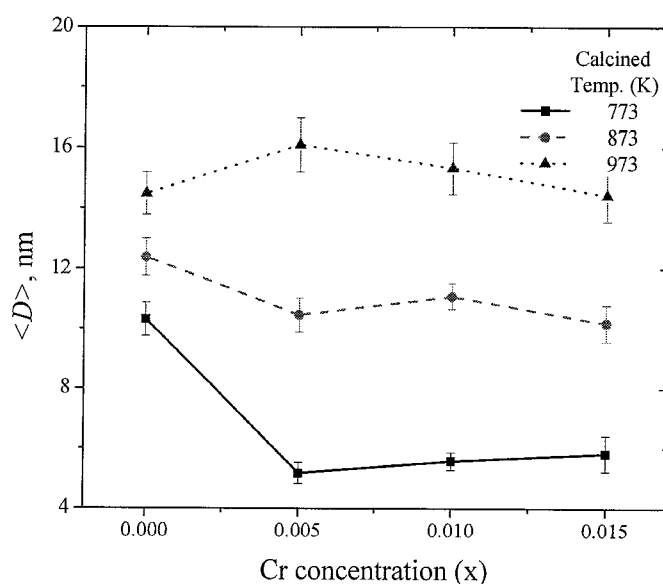


**Figure 4.5** Crystallite sizes of the  $\text{Sn}_{1-x}\text{Cr}_x\text{O}_{2-\delta}$  ( $x \leq 0.015$ ) samples with the various calcination temperatures calculated by Scherrer's equation.

### Crystallite size calculated by Williamson-Hall Plot (WHP) method

The average crystallite size of the  $\text{Sn}_{1-x}\text{Cr}_x\text{O}_{2.6}$  samples with  $x \leq 0.015$  calculated by the Williamson-Hall Plot method was shown in Figure 4.6. The crystallite size tendency was similar to that obtained from Scherrer's equation. The average crystallite size was in the range of 5 - 20 nm. However, crystallite sizes from WHP were higher than those obtained from Scherrer's equation.

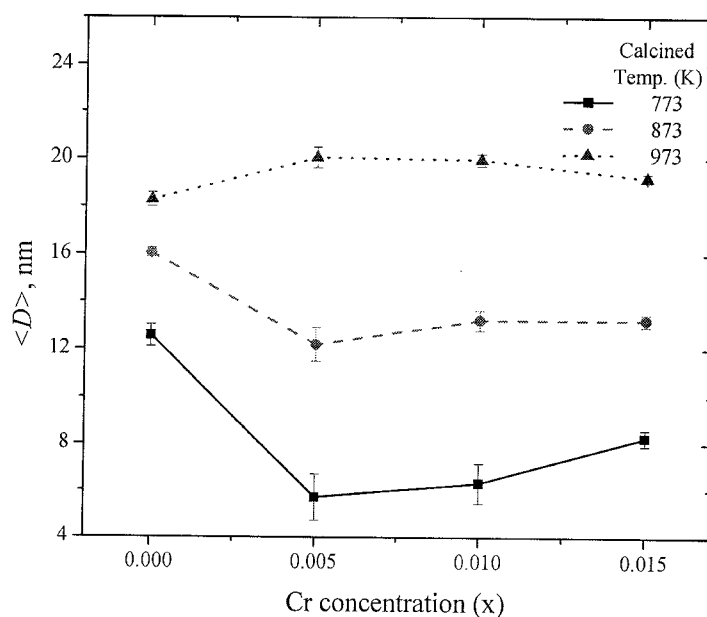


**Figure 4.6** Crystallite sizes of the  $\text{Sn}_{1-x}\text{Cr}_x\text{O}_{2.6}$  ( $x \leq 0.015$ ) samples with the various calcination temperatures calculated by Williamson-Hall Plot method.

#### 4.1.4 Microstructure

Transmission Electron Microscopy (TEM) images of  $\text{Sn}_{0.995}\text{Cr}_{0.015}\text{O}_{2.6}$  calcined at 973 K was shown in Figure 4.7(a). The presence of nearly spherical-like nanoparticles was illustrated in the TEM images. The diffraction in the inset in Figure 4.7(a) exhibited the polycrystalline rings that in agreement with the XRD patterns. Diameters in the size distribution were given in Figure 4.7(b).

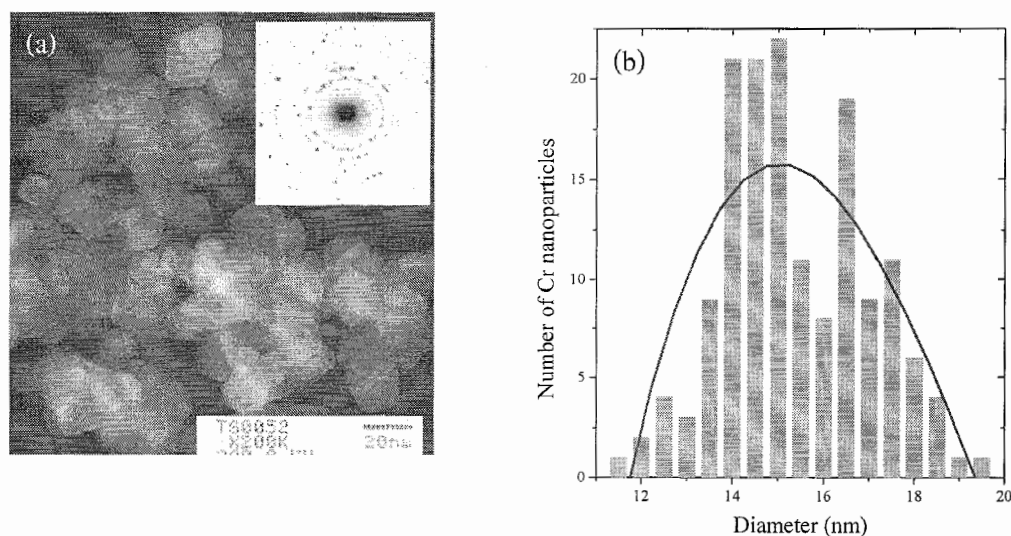


**Figure 4.7** (a) TEM images of  $\text{Sn}_{0.995}\text{Cr}_{0.015}\text{O}_{2-\delta}$  calcined at 973 K and (b) measured Cr nanoparticle size distribution corresponding to the TEM image shown in (a).

The particles were elongated with their sizes changing in the range of 5-16 nm. The crystallite sizes matched very well with similar estimation obtained from XRD results. However, the particles sizes obtained from TEM were slightly larger than those obtained from Scherrer's equation and Williamson–Hall Plot method. The advantage of using TEM for determining the particle size distribution was that one physically observed the particles and obtained information about not only particle size but also morphology. The particle sizes of the  $\text{Sn}_{1-x}\text{Cr}_x\text{O}_{2-\delta}$  samples were listed in Table 4.2.

**Table 4.2** Crystallite sizes of the  $\text{Sn}_{1-x}\text{Cr}_x\text{O}_{2-\delta}$  samples obtained from TEM images

| Calcined Temp.<br>(K) | Crystallite sizes, $\langle D \rangle$ (nm)             |   |   |
|-----------------------|---|---|---|
|                       | $\text{Sn}_{0.995}\text{Cr}_{0.005}\text{O}_{2-\delta}$ | $\text{Sn}_{0.990}\text{Cr}_{0.010}\text{O}_{2-\delta}$ | $\text{Sn}_{0.985}\text{Cr}_{0.015}\text{O}_{2-\delta}$ |
| 773                   | $5.10 \pm 0.57$   | $5.90 \pm 0.49$   | $5.36 \pm 0.57$   |
| 973                   | $14.02 \pm 1.12$  | $15.97 \pm 1.94$  | $15.62 \pm 1.61$  |

#### 4.1.5 Optical Properties

Optical characterizations of nanoparticle materials were carried out by measuring the diffuse reflectance spectra at room temperature. The diffuse reflectance,  $R$  was related to the Kubelka–Munk function  $f(R)$  by the relation,  $f(R) = (1-R)^2/2R$ . The diffuse reflectance spectra of the  $\text{Sn}_{1-x}\text{Cr}_x\text{O}_{2.8}$  samples with the different Cr content calcined at 873 K were depicted in Figure 4.8. The spectra of the nanoparticle samples showed two absorption bands at wavelengths of about 700 and 550 nm. The bands were assigned to  ${}^3\text{T}_{1g}(\text{F}) \rightarrow {}^3\text{T}_{2g}(\text{F})$  and  ${}^3\text{T}_{1g}(\text{F}) \rightarrow {}^3\text{T}_{1g}(\text{P})$  transitions, respectively, for  $\text{Cr}^{4+}$  ( $3d^2$ ) in an octahedral site. These absorption bands were corresponding to  $\text{Cr}^{4+}$  in  $\text{SnO}_2$  ceramics reported by Ren *et al.* [89]. The observation of  $d-d$  transition of  $\text{Cr}(\text{IV})$  in an octahedral site indicated that  $\text{Cr}^{4+}$  has been substituted for  $\text{Sn}^{4+}$ . In order to confirm that  $\text{Cr}^{4+}$  has been substituted for  $\text{Sn}^{4+}$ , the sample colour has been considered. The colour of  $\text{SnO}_2$  powders was white. The  $\text{Sn}_{1-x}\text{Cr}_x\text{O}_{2.8}$  samples were a pale-purple and a dark-purple in higher Cr concentration. This result closely related to  $\text{Cr}^{4+}$  in  $\text{SnO}_2$  ceramics [89], which generated a purple colour. Therefore, the  $\text{Sn}_{1-x}\text{Cr}_x\text{O}_{2.8}$  samples with a purple colour might be resulting from  $\text{Cr}^{4+}$  substituted into  $\text{Sn}^{4+}$  site.

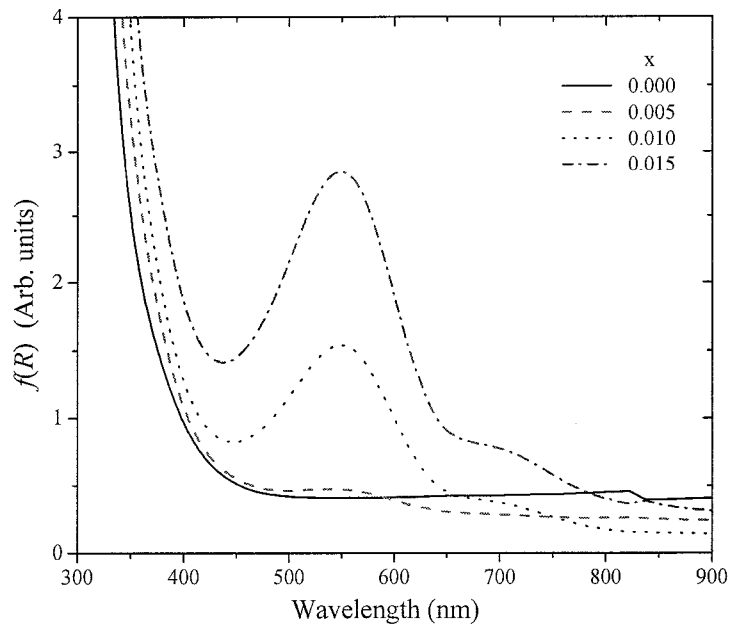


**Figure 4.8** Kubelka-Munk spectra of the  $\text{Sn}_{1-x}\text{Cr}_x\text{O}_{2.8}$  samples calcined at 873 K with the different Cr concentration.

To evaluate the band gap energy ( $E_g$ ) of the  $\text{Sn}_{1-x}\text{Cr}_x\text{O}_{2.8}$  samples, the  $(f(R)h\nu)^2$  was plotted against photon energy ( $h\nu$ ) in electron volts. For example, the plot of  $(f(R)h\nu)^2$  as a function of  $h\nu$  for the  $\text{Sn}_{1-x}\text{Cr}_x\text{O}_{2.8}$  samples calcined at 873 K with varying Cr concentration was shown in Figure 4.9. The strength lines represented the linear part of the curve which was extrapolated to intercept an abscissa axis to estimate the direct band gap energy. The obtained energy gap for the  $\text{Sn}_{1-x}\text{Cr}_x\text{O}_{2.8}$  samples were in the range of 3.90 - 4.03 eV, whereas the undoped  $\text{SnO}_2$  was about 3.99 - 4.02 eV as listed in Table 4.3.

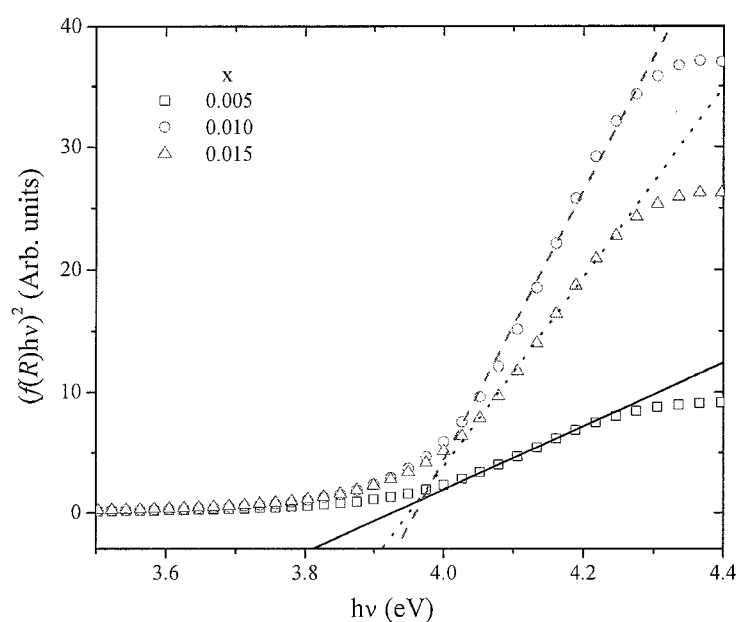


**Figure 4.9** Plot of  $(f(R)h\nu)^2$  as a function of  $h\nu$  for the  $\text{Sn}_{1-x}\text{Cr}_x\text{O}_{2.8}$  samples calcined at 873 K with the varying Cr concentrations.

**Table 4.3** Band Gap Energy,  $E_g$  (eV) of the  $\text{Sn}_{1-x}\text{Cr}_x\text{O}_{2-\delta}$  samples

| Compound  | Calcined Temperature (K) | $E_g$ (eV) |
|---|--------------------------|------------|
| $\text{SnO}_2$  | 773                      | 3.98       |
|   | 873                      | 3.99       |
|   | 973                      | 4.02       |
| $\text{Sn}_{0.995}\text{Cr}_{0.005}\text{O}_{2-\delta}$ | 773                      | 3.93       |
|   | 873                      | 3.93       |
|   | 973                      | 3.97       |
| $\text{Sn}_{0.990}\text{Cr}_{0.010}\text{O}_{2-\delta}$ | 773                      | 3.90       |
|   | 873                      | 3.97       |
|   | 973                      | 3.95       |
| $\text{Sn}_{0.985}\text{Cr}_{0.015}\text{O}_{2-\delta}$ | 773                      | 3.99       |
|   | 873                      | 3.96       |
|   | 973                      | 4.03       |

At low level Cr doping concentration ( $x \leq 0.015$ ), the different of the band gap values were very small as illustrated in Figure 4.10. It is concluded that substitution of Cr into Sn site was less effect to  $E_g$  of  $\text{SnO}_2$ . However, the band gap energies were much larger than the expected 3.6 eV for bulk pure  $\text{SnO}_2$  [50]. All results also confirmed that the particle size of  $\text{Sn}_{1-x}\text{Cr}_x\text{O}_{2-\delta}$  samples synthesized by the autocombustion technique were in the nanometer scale.



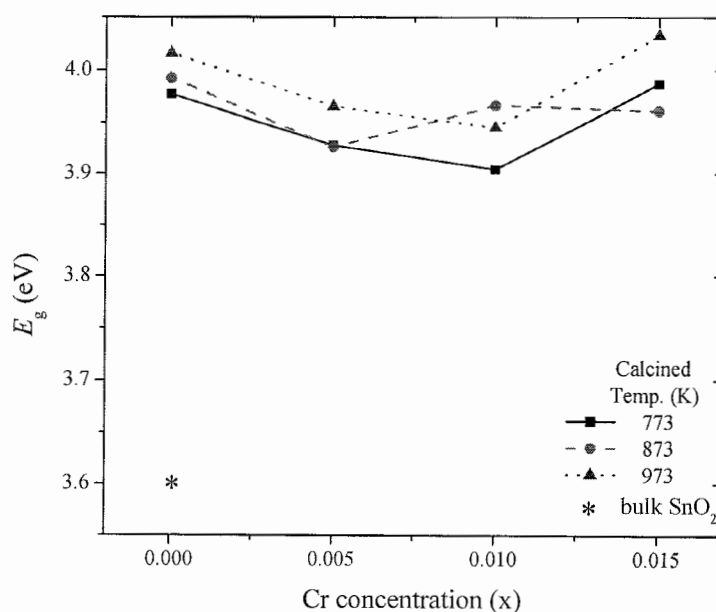


**Figure 4.10** Band gap energy ( $E_g$ ) of the  $\text{Sn}_{1-x}\text{Cr}_x\text{O}_{2.8}$  samples calcined at different temperatures and with the varying Cr concentrations.

#### 4.1.6 Magnetic Measurements

Relationship between the magnetization ( $M$ ) and the magnetic field ( $H$ ) of  $\text{Sn}_{0.995}\text{Cr}_{0.005}\text{O}_{2.8}$  calcined at 773, 873 and 973 K were illustrated in Figure 4.11. The magnetic property of the samples holder was measured first which exhibited diamagnetic magnetization. These values were subtracted automatically by the computer during the measurement of the nanoparticle samples. The hysteresis loops of the samples calcined at 873 and 973K were ferromagnetic at the room temperature. However, there was not clear loop for the sample calcined at 773 K. The saturated magnetization ( $M_s$ ) values of the samples calcined at 873 and 973K were 0.039 and 0.012  $\mu_B/\text{Cr}$ , respectively. Moreover, the remanance magnetizations ( $M_r$ ) were 0.015 and 0.003  $\mu_B/\text{Cr}$  for the samples calcined at 873 and 973K, respectively. The coercivity ( $H_c$ ) was about 300 Oe for all samples. Actually, the doping with a non-ferromagnetic element (i.e. Cr, V) could result in a magnetic moment. This was similar to that was obtained for V-doped  $\text{TiO}_2$  ( $4.2 \mu_B/\text{V}$ ) [21] or Cr-doped  $\text{TiO}_2$  ( $0.6 \mu_B/\text{Cr}$ ) [31], proving that the induced ferromagnetic did not depend simply on the magnetic order of the dopant elements. It was proved that doping a small amount of Cr into non-magnetic oxides could induce the room temperature ferromagnetism.

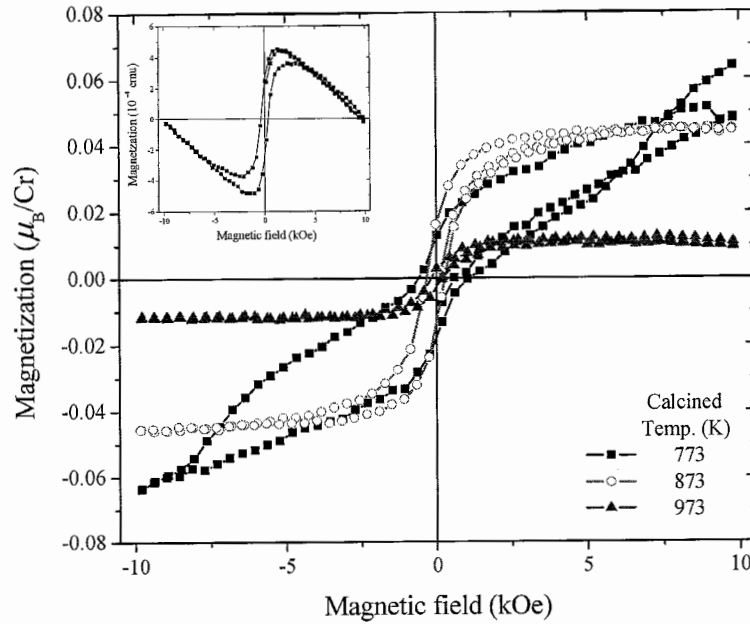


**Figure 4.11** Magnetization ( $M$ ) at room temperature of  $\text{Sn}_{0.995}\text{Cr}_{0.005}\text{O}_{2-\delta}$  calcined at 773, 873 and 973 K. Inset: diamagnetic background hysteresis loop.

The large magnetic moment in V-doped  $\text{TiO}_2$  [21] was consistent with the theoretical production with several assumptions. The large value of moment completely ruled out the possibility for having V clusters. This assumption did not come from V particles cluster which was confirmed by the magnetic force microscopy measurements. The giant magnetic moment was reported once for  $\text{Co:SnO}_2$  thin films and the authors assumed that it was due to unquenched orbital contributions [51]. The orbital moment might also play a role in V-doped  $\text{TiO}_2$  [21]. Most probably unquenched orbital moment would decrease the spin values. Moreover, the role of oxygen vacancies to act as additional carriers was also a possible assumption.

In this work, the saturated magnetization ( $M_s$ ) values could not come from Cr metal clusters because Cr metal was known to be paramagnetic at high temperatures and antiferromagnetic below 308 K [90]. These  $M_s$  values of the  $\text{Sn}_{1-x}\text{Cr}_x\text{O}_{2-\delta}$  samples did not match the values for  $\text{CrO}_2$  ( $\text{CrO}_2$  had  $T_c = 386$  K and  $M_s = 2.03 \mu_B/\text{Cr}$ ) [91]. Therefore, it was possible to assume that the ferromagnetism did not come from  $\text{CrO}_2$  clusters (also recall the XRD data with no peak for  $\text{CrO}_2$ ). These  $\text{Sn}_{1-x}\text{Cr}_x\text{O}_{2-\delta}$  samples produced only very small ferromagnetic signals,

which might appear to be in contrast to the finding of room temperature ferromagnetism in Cr-doped  $\text{SnO}_2$  thin films produced by Pulse Laser Deposition [57], with a giant magnetic moment of up to  $\sim 6 \mu_B/\text{Cr}$ . The key issue here might be the concentrations of oxygen defects that were definitely much higher in the reduced samples. Coey *et al.* have recently suggested *F*-center electrons trapped in oxygen vacancies as candidates for ferromagnetic coupling in Fe-doped  $\text{SnO}_2$  thin films [55]. In order to maintain charge neutrality when  $\text{Cr}^{3+}$  substituted for  $\text{Ti}^{4+}$ , one oxygen atom vacancy could be created for every two substitutional  $\text{Cr}^{3+}$  dopants [31]. In Figure 4.8, the reflection bands were confirmed that  $\text{Cr}^{4+}$  has been substituted for  $\text{Sn}^{4+}$ . It was indicated that small ferromagnetic behavior did not come from the role of oxygen vacancies. However, there were changes in the oxygen stoichiometry as seen in Table 4.1. Oxygen vacancy might slightly occur in the samples calcined at 873 and 973 K due to lattice distortion. The ferromagnetic behaviors of the samples were exhibited at the room temperature with the magnetization at 10 kOe slightly decreased with increasing amount of Cr impurity. It was possible that the small magnetization was due to the presence of small amount of Cr metal, non-magnetic element. The small coercivity of polycrystalline samples ( $\sim 300$  Oe) depicted the intrinsically soft nature of these materials.

For previous reports, there was ferromagnetic property at the room temperature accompanying a giant magnetic moment of  $6 \mu_B/\text{Cr}$  in Cr-doped  $\text{SnO}_2$  thin films grown on  $\text{LaAlO}_3$  substrates [57]. Their moment was much larger than that of the films grown on  $\text{SrTiO}_3$  ( $0.27 \mu_B/\text{Cr}$ ) and *R*-cut sapphire substrates ( $0.2 \mu_B/\text{Cr}$ ). However, the magnetic curves of the  $\text{Sn}_{0.8}\text{Cr}_{0.2}\text{O}_2$  films were completely paramagnetic [61]. These results implied that the different magnetic properties of Cr-doped  $\text{SnO}_2$  were showed in order to the difference either preparation technique, Cr dopant or substrates for growing thin films. As the result, the room temperature hysteresis loops of  $\text{Sn}_{0.990}\text{Cr}_{0.010}\text{O}_{2.8}$  calcined at 773, 873 and 973 K were illustrated in Figure 4.12.

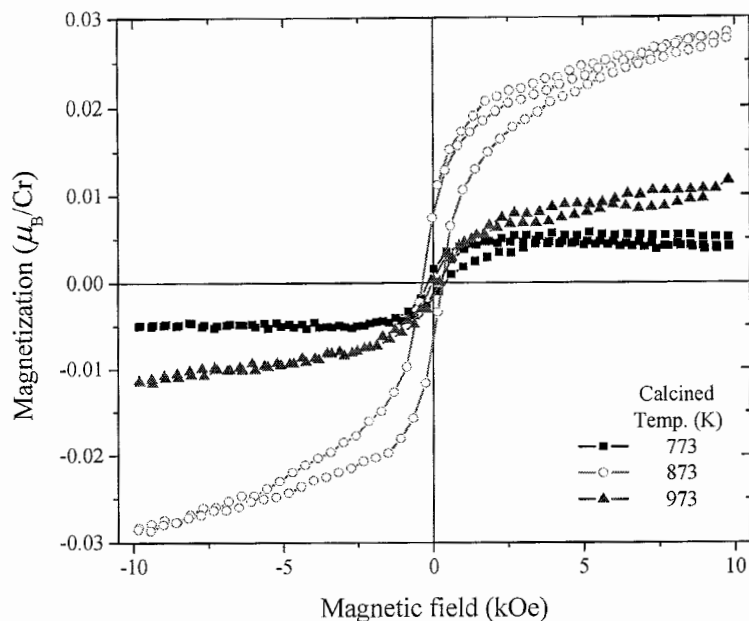


**Figure 4.12** Magnetization ( $M$ ) at room temperature of  $\text{Sn}_{0.990}\text{Cr}_{0.010}\text{O}_{2.8}$  calcined at 773, 873 and 973 K.

The hysteresis loops in Figure 4.12 were a weak ferromagnetism. The small magnetic moment of 0.005 and 0.007  $\mu_{\text{B}}/\text{Cr}$  were showed for the  $\text{Sn}_{0.990}\text{Cr}_{0.010}\text{O}_{2.8}$  samples calcined at 773 and 973 K, respectively. A little enhancement in the ferromagnetic properties was occurred in the sample calcined at 873 K with the moment about 0.018  $\mu_{\text{B}}/\text{Cr}$ . The values of  $M_{\text{R}}$  were 0.001, 0.007 and 0.002  $\mu_{\text{B}}/\text{Cr}$  for the samples calcined at 773, 873 and 973 K, respectively. The value of  $H_{\text{C}}$  was about of 300 Oe for all samples. The well defined hysteresis loops were depicted for those samples indicating a ferromagnetic behavior with  $M_{\text{R}}/M_{\text{S}}$  of 0.20, 0.39 and 0.29 for the samples calcined at 773, 873 and 973 K, respectively.

Moreover, magnetizations at room temperature as a function of the magnetic field of  $\text{Sn}_{0.985}\text{Cr}_{0.015}\text{O}_{2.8}$  calcined at 773, 873 and 973 K were illustrated in Figure 4.13. The hysteresis loops also depicted a weak ferromagnetism. The  $\text{Sn}_{0.990}\text{Cr}_{0.010}\text{O}_{2.8}$  samples calcined at 773, 873 and 973 K showed a very small magnetic moment of 0.018, 0.012 and 0.005  $\mu_B/\text{Cr}$ , respectively. The values of  $M_R$  were 0.009, 0.005 and 0.001  $\mu_B/\text{Cr}$  for the samples calcined at 773, 873 and 973 K, respectively. The values of  $H_C$  were about 300 Oe for all samples. The well defined hysteresis loops were occurred for these samples indicating a ferromagnetic behavior with  $M_R/M_S$  of 0.50, 0.42 and 0.16 for the sample calcined at 773, 873 and 973 K, respectively.

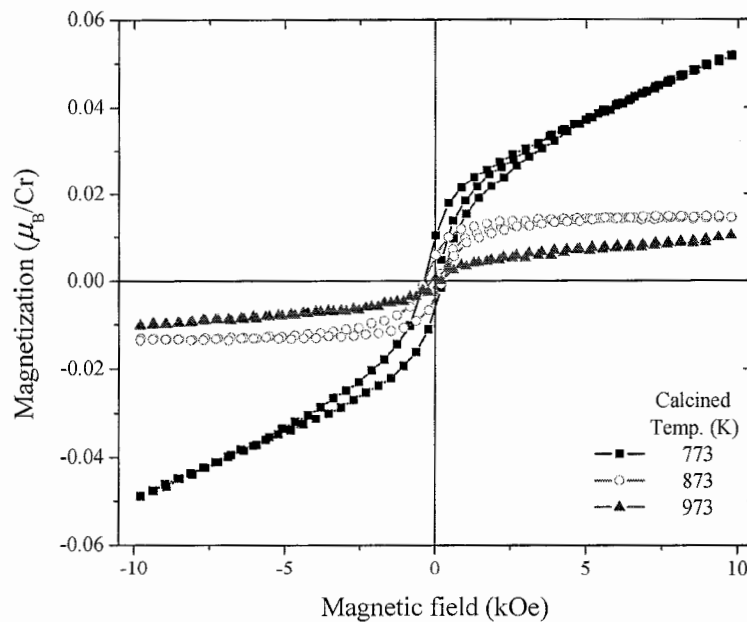


**Figure 4.13** Magnetization ( $M$ ) at room temperature of  $\text{Sn}_{0.985}\text{Cr}_{0.015}\text{O}_{2.8}$  calcined at 773, 873 and 973 K.

In general, the values of  $M_S$ ,  $M_R$  and  $H_C$  (in Figure 4.11 – Figure 4.13) gradually were increased with independent calcined temperatures. The samples produced a very weak ferromagnetic response at room temperature. It was implied that the host matrix was at least partly responsible for the ferromagnetism in these doped oxide materials.

The room temperature magnetization as a function of magnetic field of the  $\text{Sn}_{1-x}\text{Cr}_x\text{O}_{2.8}$  samples with  $x = 0.005, 0.010$  and  $0.015$  calcined at  $873\text{ K}$  was illustrated in Figure 4.14. A clearly ferromagnetic was occurred in their hysteresis loops. The saturation magnetization of  $0.039, 0.018$  and  $0.012\ \mu_{\text{B}}/\text{Cr}$  and the  $M_{\text{R}}$  value of  $0.015, 0.007$  and  $0.005\ \mu_{\text{B}}/\text{Cr}$  were appeared in the samples with  $x = 0.005, 0.010$  and  $0.015$ , respectively. The  $H_{\text{C}}$  value of the samples was in a value of  $300\text{ Oe}$ . These samples remained almost unchanged in remanence ratio of  $0.38 - 0.42$ .

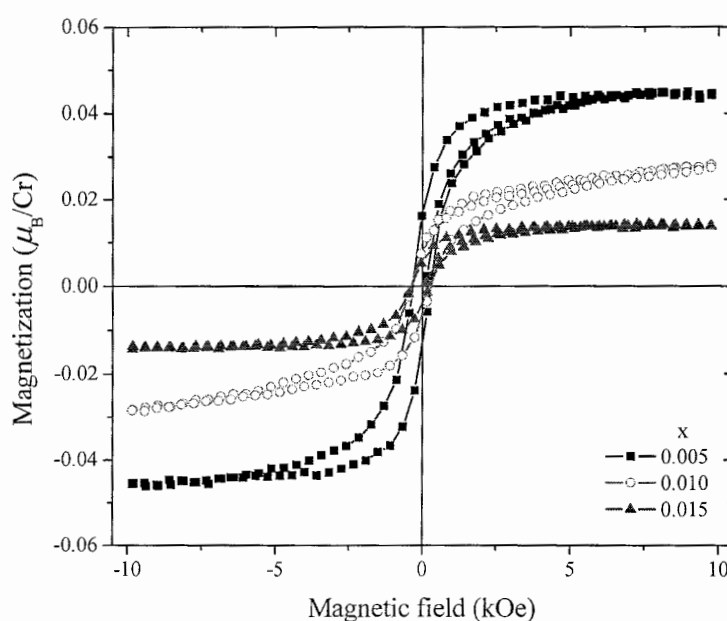


**Figure 4.14** Magnetization ( $M$ ) at room temperature of the  $\text{Sn}_{1-x}\text{Cr}_x\text{O}_{2.8}$  ( $x \leq 0.015$ ) samples calcined at  $873\text{ K}$ .

For the  $\text{Sn}_{1-x}\text{Cr}_x\text{O}_{2.8}$  samples with  $x = 0.005, 0.010$  and  $0.015$  calcined at  $773\text{ K}$  in Figure 4.15, the  $M_{\text{S}}$  values for  $x = 0.010$  was about  $0.008\ \mu_{\text{B}}/\text{Cr}$  and the moments was  $0.018\ \mu_{\text{B}}/\text{Cr}$  with  $x = 0.015$ . On the other hands, there was not clear loop for  $x = 0.005$ .

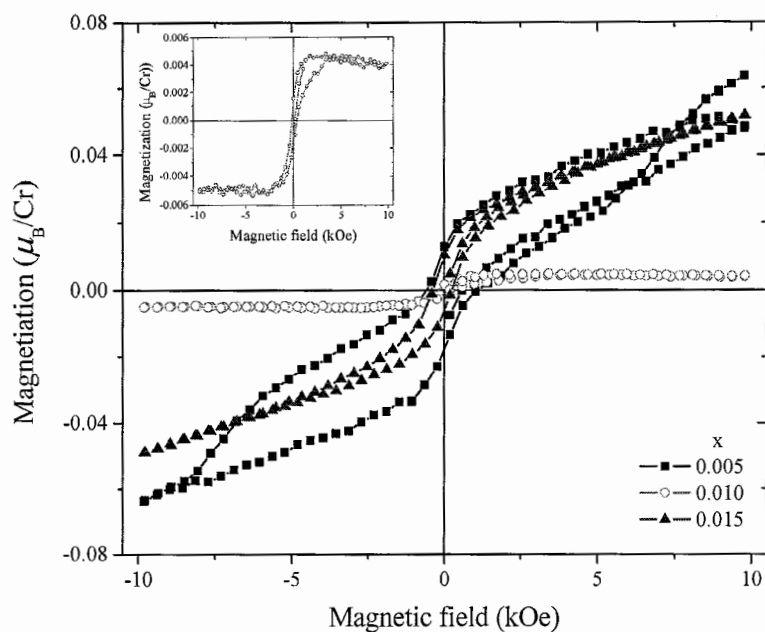


**Figure 4.15** Magnetization ( $M$ ) at room temperature of the  $\text{Sn}_{1-x}\text{Cr}_x\text{O}_{2-\delta}$  ( $x \leq 0.015$ ) samples calcined at 773 K. Inset: enlarge for  $\text{Sn}_{0.990}\text{Cr}_{0.010}\text{O}_{2-\delta}$  calcined at 773 K.

For the  $\text{Sn}_{1-x}\text{Cr}_x\text{O}_{2-\delta}$  samples calcined at 773 K in Figure 4.16, the magnetic moments were 0.022, 0.014 and 0.005  $\mu_B/\text{Cr}$  for  $x = 0.005$ , 0.010 and 0.015, respectively.

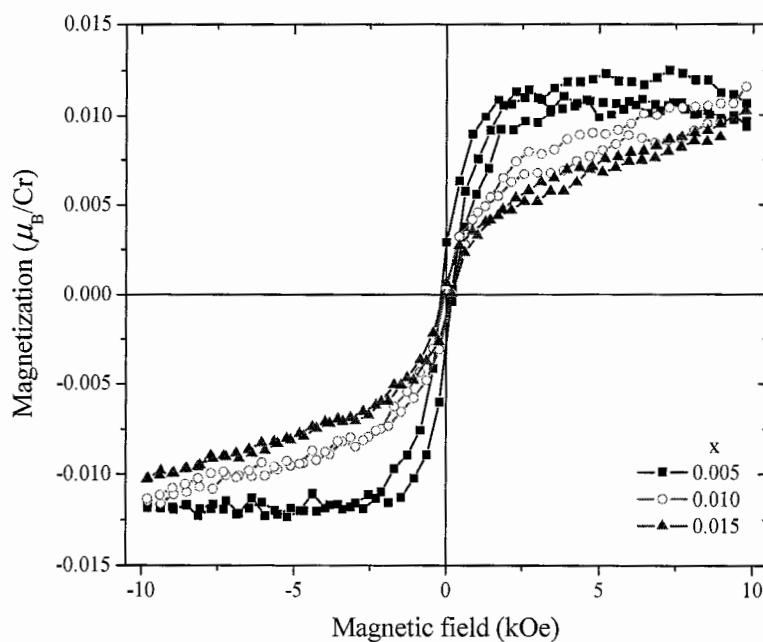


**Figure 4.16** Magnetization ( $M$ ) at room temperature of the  $\text{Sn}_{1-x}\text{Cr}_x\text{O}_{2-\delta}$  ( $x \leq 0.015$ ) samples calcined at 973 K.

## 4.2 Cobalt-doped tin oxide ( $\text{Sn}_{1-x}\text{Co}_x\text{O}_{2-\delta}$ )

### 4.2.1 X-ray Diffraction Studies

Powder XRD patterns of the  $\text{Sn}_{1-x}\text{Co}_x\text{O}_{2-\delta}$  samples with  $x \leq 0.015$  calcined at 873 K were shown in Figure 4.17. All of the  $\text{Sn}_{1-x}\text{Co}_x\text{O}_{2-\delta}$  samples could be indexed to the rutile structure with the space group  $\text{P42/mnm}$ . After a partial substitution of Sn by Co, the diffraction pattern illustrated the same positions. It was indicated that the rutile structure was not disturbed by Co substitution. No additional peaks were observed due to the absence of cobalt metal, oxides or any binary tin cobalt phases. This conclusion was confirmed by Punnose *et al.* that these phases are absent in any of the samples doped with cobalt up to 5% Co atomic weight [52]. Moreover, these samples were lower dopant about  $x \leq 0.015$  than the solubility limit of Co in  $\text{SnO}_2$ , in which  $x = 0.15$  had three additional peaks corresponding to  $\text{Co}_3\text{O}_4$  [62] or weak peaks of  $\text{Co}_3\text{O}_4$  were appeared with Co doping for  $x \geq 0.08$  [54]. The peak positions did not illustrate any measurable change, while the intensities of the peaks were decreased with increasing Co concentration.

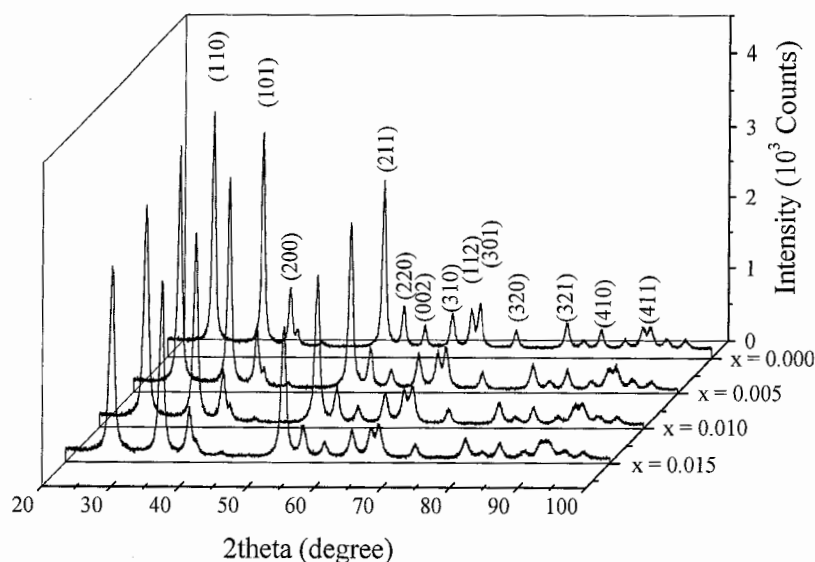


**Figure 4.17** X-ray Diffraction patterns of the  $\text{Sn}_{1-x}\text{Co}_x\text{O}_{2-\delta}$  ( $x \leq 0.015$ ) samples calcined at 873 K.



The crystallinity of Co-doped  $\text{SnO}_2$  was increased as increasing calcination temperature with more clearly a rutile structure as seen in Figure 4.18. In addition, the significant changes in XRD peak were appeared with Co doping in the plane (110), shown in Figure 4.19. Since the atomic scattering factor of Sn was greater than that of Co [87], the XRD intensities were decreased with increasing Co concentration in  $\text{SnO}_2$ . Therefore, decreasing intensities in XRD pattern were occurred when Co was substituted on  $\text{SnO}_2$  matrix.

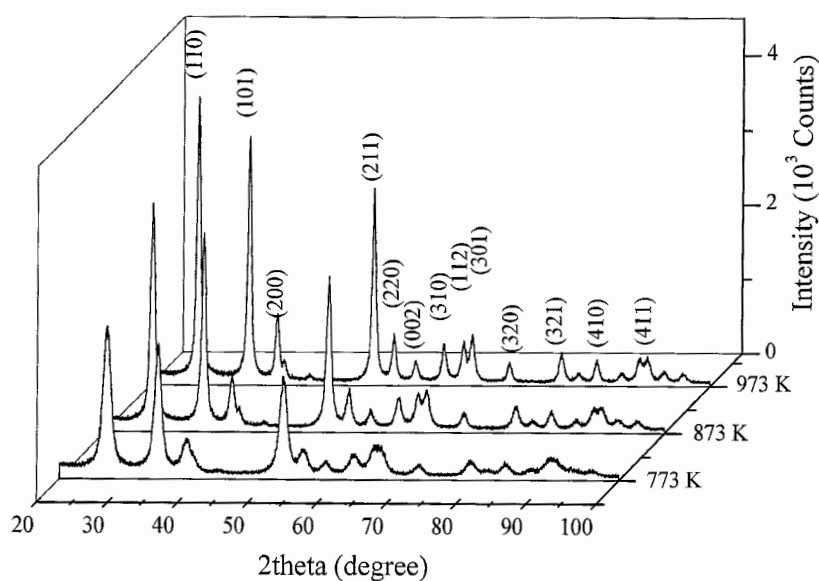


**Figure 4.18** X-ray Diffraction patterns of the  $\text{Sn}_{0.990}\text{Co}_{0.010}\text{O}_{2.6}$  samples with the variation of calcined temperatures.

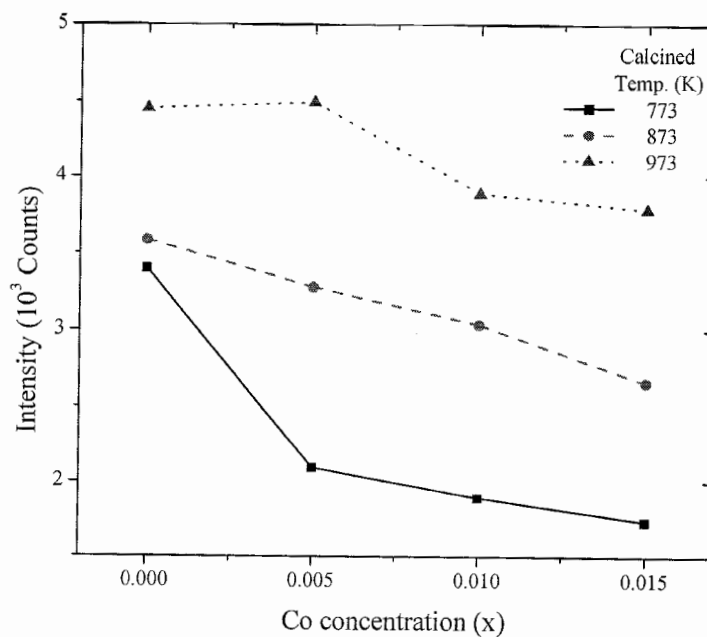


**Figure 4.19** Maximum intensities in the (110) of the  $\text{Sn}_{1-x}\text{Co}_x\text{O}_{2.δ}$  ( $x \leq 0.015$ ) samples calcined at 773, 873 and 973 K.

#### 4.2.2 The Rietveld refinement

The Rietveld refinement from the XRD patterns of the  $\text{Sn}_{1-x}\text{Co}_x\text{O}_{2.δ}$  samples calcined at 973 K were depicted in Figure 4.20. In all cases, the peak positions were assigned to the bulk rutile  $\text{SnO}_2$ . No any phase ascribed to chromium compounds was detected. These results were indicated that all cobalt ions were diffused into the crystal lattice of bulk  $\text{SnO}_2$  to substitute for tin ions. The resulting lattice parameters obtained from the Rietveld refinement of these Co-doped samples were illustrated in Table 4.4.

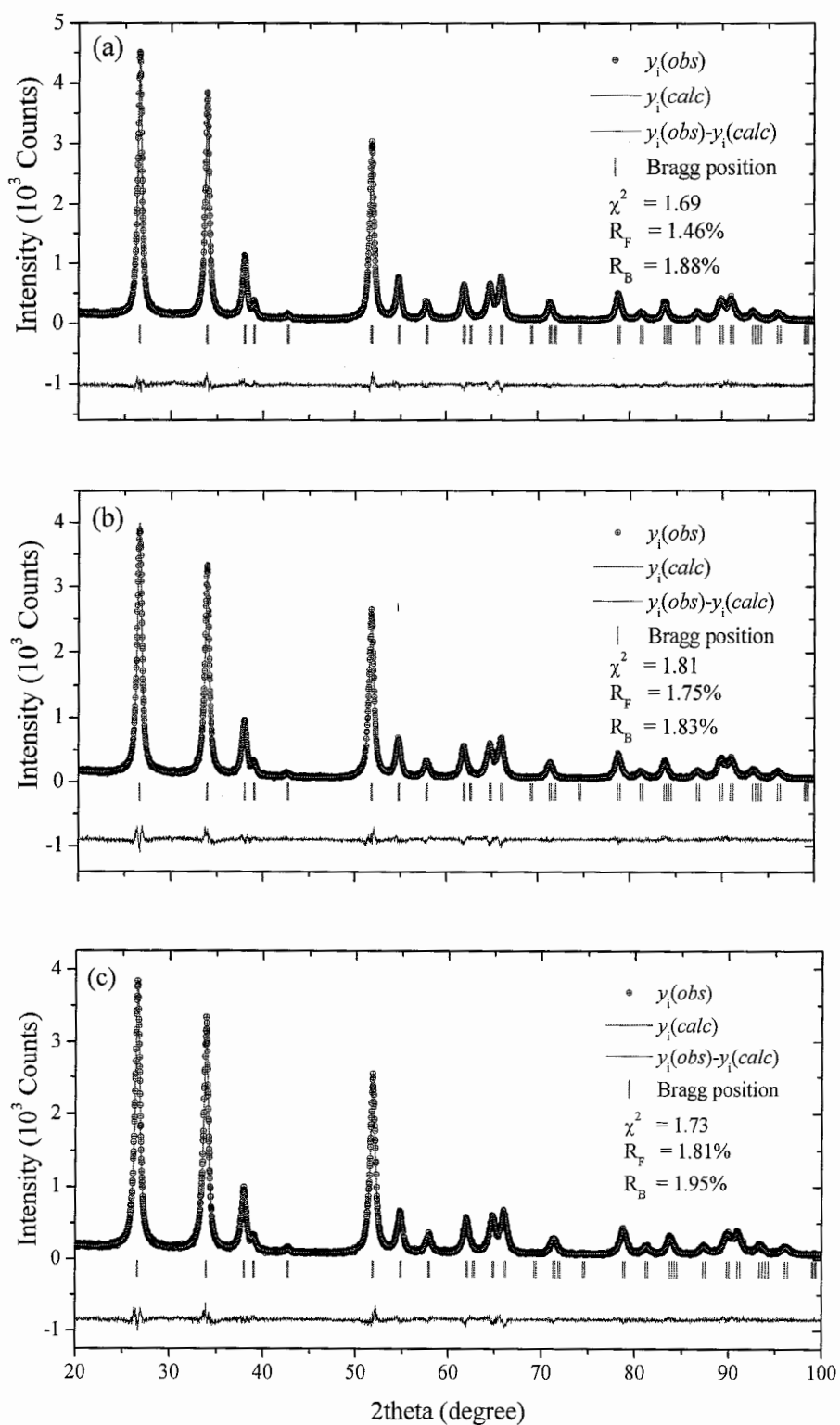


**Figure 4.20** X-ray diffractograms of (a)  $\text{Sn}_{0.995}\text{Co}_{0.005}\text{O}_{2-\delta}$ , (b)  $\text{Sn}_{0.990}\text{Co}_{0.010}\text{O}_{2-\delta}$  and (c)  $\text{Sn}_{0.985}\text{Co}_{0.015}\text{O}_{2-\delta}$  calcined at 973 K. Data points were indicated by solid cycles, while the calculated patterns were shown as a continuous line. The positions of the reflections were indicated with the vertical lines below the patterns.

**Table 4.4** The Rietveld refinement crystallographic data of the  $\text{Sn}_{1-x}\text{Co}_x\text{O}_{2-\delta}$  ( $x = 0.005, 0.010$  and  $0.015$ ) samples calcined at 773, 873 and 973 K. The space group P42/mmm was used for all samples. Sn/Cr was occupied at (0, 0, 0) and  $\text{O}^{2-}$  was occupied at (x, y, 0) while x was equal to y. The numbers in the parenthesis were estimated standard deviations to the last significant digit.

| Compound                           | $\text{Sn}_{0.995}\text{Co}_{0.005}\text{O}_{2-\delta}$ |           |           | $\text{Sn}_{0.990}\text{Co}_{0.010}\text{O}_{2-\delta}$ |           |           | $\text{Sn}_{0.985}\text{Co}_{0.015}\text{O}_{2-\delta}$ |           |           |
|------------------------------------|---|-----------|-----------|---|-----------|-----------|---|-----------|-----------|
| Calced Temp. (K)                   | 773   | 873       | 973       | 773   | 873       | 973       | 773   | 873       | 973       |
| Parameters                         |   |           |           |   |           |           |   |           |           |
| $a = b$ (Å)                        | 4.7388(3)   | 4.7372(4) | 4.7398(4) | 4.7374(2)   | 4.7362(2) | 4.7365(2) | 4.7366(1)   | 4.7371(2) | 4.7364(2) |
| $c$ (Å)                            | 3.1895(3)   | 3.1879(3) | 3.1906(3) | 3.1868(1)   | 3.1860(2) | 3.1870(2) | 3.1858(1)   | 3.1865(1) | 3.1860(1) |
| Volume (Å <sup>3</sup> )           | 71.63(1)  | 71.54(1)  | 71.68(1)  | 71.52(1)  | 71.47(1)  | 71.50(1)  | 71.47(1)  | 71.50(1)  | 71.47(1)  |
| $\text{O}^{2-}$ position (x)       | 0.305(1)  | 0.306(1)  | 0.304(1)  | 0.302(1)  | 0.305(1)  | 0.302(1)  | 0.305(1)  | 0.305(1)  | 0.304(1)  |
| $B_{\text{iso}}$ (Å <sup>2</sup> ) | 0.24(1)   | 0.24(1)   | 0.24(1)   | 0.23(1)   | 0.24(1)   | 0.23(1)   | 0.23(1)   | 0.23(1)   | 0.23(1)   |
| $R_p$ (%)                          | 8.78  | 9.10      | 9.59      | 8.73  | 9.35      | 9.89      | 8.42  | 8.77      | 8.79      |
| $R_{\text{wp}}$ (%)                | 10.7  | 11.0      | 11.5      | 10.9  | 11.3      | 11.7      | 10.6  | 11.0      | 10.9      |
| $R_{\text{exp}}$ (%)               | 8.23  | 8.35      | 8.83      | 8.32  | 8.36      | 8.79      | 8.10  | 8.20      | 8.36      |
| $R_B$ (%)                          | 1.65  | 1.93      | 1.88      | 2.01  | 2.27      | 1.83      | 1.66  | 1.96      | 1.95      |
| $R_F$ (%)                          | 1.43  | 1.51      | 1.46      | 1.72  | 1.85      | 1.75      | 1.62  | 1.79      | 1.81      |
| $\chi^2$                           | 1.70  | 1.74      | 1.69      | 1.76  | 1.87      | 1.81      | 1.85  | 1.85      | 1.73      |
| DW-stat                            | 1.16  | 1.14      | 1.17      | 1.21  | 1.14      | 1.16      | 1.31  | 1.20      | 1.30      |

For the Rietveld refinement, the structure refinement out put of the  $\text{Sn}_{1-x}\text{Co}_x\text{O}_{2.6}$  samples was illustrated in Table 4.4. These changes were revealed interesting variations in both the unit cell volume and the lattice parameters  $a$  and  $c$  with Co concentrations. On increasing of Co dopants, the lattice parameter  $c$  was slightly increased. Exception for calcined sample at 773 K, no significant change was detected. This was corresponded to the solubility limit for cobalt in  $\text{SnO}_2$  [60]. When Co concentrations were increased, the lattice parameters were increased and above  $x = 0.02$  these trends were reversed. In the other hands, the parameter  $a$  was shown for a little decrease with increasing Co contents (Table 4.4). Such a rapid contraction of the lattice could be understood qualitatively considering the sizes of the ions and their local coordinations. The possible charge states of Co dopant were  $\text{Co}^{2+}$  ( $3d^7$ ) and  $\text{Co}^{3+}$  ( $3d^6$ ), both in a low-spin state. The electron configuration of each ion was given in brackets. Substitution of either 0.65 Å sized  $\text{Co}^{2+}$  or 0.55 Å sized  $\text{Co}^{3+}$  at 0.69 Å sized  $\text{Sn}^{4+}$  was expected to reduce the interatomic spacing significantly, justifying the initial contraction of the lattice. Decreasing in the tetragonality was confirmed about substitution of Co ions in Sn matrix [88].

### 4.2.3 Crystallite Sizes

The average particle sizes ( $\langle D \rangle$ ) for all the samples were calculated using both Scherrer's equation and Williamson-Hall Plot (WHP) method. Calculation Steps for the  $\text{Sn}_{1-x}\text{Co}_x\text{O}_{2-\delta}$  samples were similar to calculation in the  $\text{Sn}_{1-x}\text{Cr}_x\text{O}_{2-\delta}$  samples.

#### Crystallite size calculated by Scherrer's Equation

Crystallite sizes of the  $\text{Sn}_{1-x}\text{Co}_x\text{O}_{2-\delta}$  samples with  $x \leq 0.015$  calcined at 773, 873 and 973 K calculated by Scherrer's Equation were summarized in Figure 4.21. The crystal sizes of the nanoparticles were affected by the amount of doped cobalt. The crystallite sizes were increased as increasing calcination temperatures, corresponding to the FWHM values which were narrower with higher calcination temperatures. On increasing the Co concentration, the average particle size was further reduced, due to the different sizes of the ionic radius and valences between the Co and Sn ions. It was concluded that the growth of  $\text{SnO}_2$  nanoparticles was inhibited by Co doping. The average crystallite size was in the range of 5 - 15 nm.

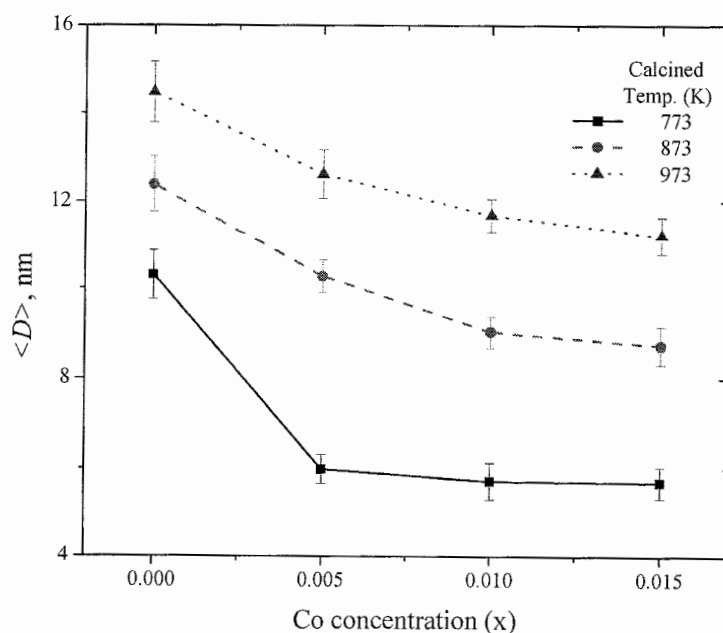


**Figure 4.21** Crystallite sizes of the  $\text{Sn}_{1-x}\text{Co}_x\text{O}_{2-\delta}$  ( $x \leq 0.015$ ) samples with the various calcination temperatures calculated by Scherrer's equation.

### Crystallite size calculated by Williamson-Hall Plot (WHP) method

Crystallite size calculations of the  $\text{Sn}_{1-x}\text{Co}_x\text{O}_{2.8}$  samples with  $x \leq 0.015$  calcined at 773, 873 and 973 K calculated by WHP method were illustrated in Figure 4.22. The crystallite sizes were increased as increasing calcination temperatures similar to those obtained from Scherrer's equation. The average crystallite size calculated by WHP method was higher than those obtained from Scherrer's method and in the range of 5 - 18 nm.

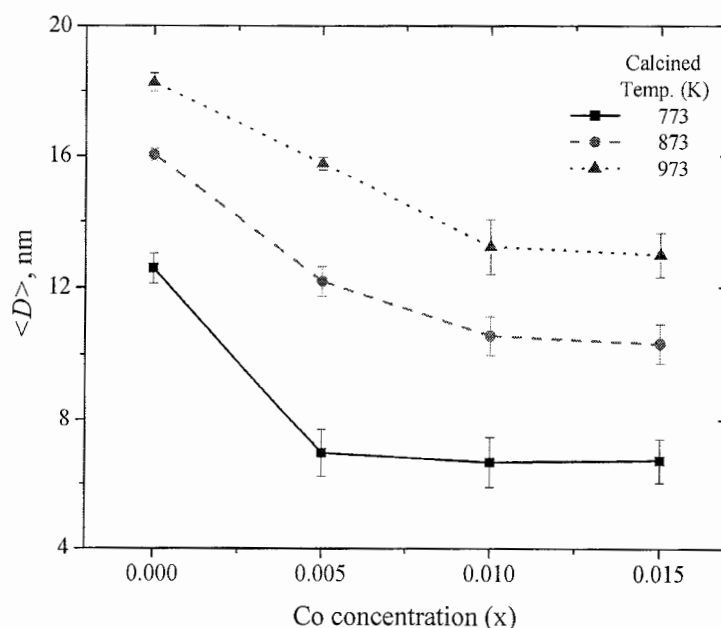


**Figure 4.22** Crystallite sizes of the  $\text{Sn}_{1-x}\text{Co}_x\text{O}_{2.8}$  ( $x \leq 0.015$ ) samples calcined at 773, 873 and 973 K calculated by Williamson-Hall Plot method.

### 4.2.4 Microstructure

A mostly spherical particles and a partly agglomeration were shown in the TEM image of  $\text{Sn}_{0.990}\text{Co}_{0.010}\text{O}_{2.8}$  nanoparticles calcined at 973 K, seen in Figure 4.23(a). The morphologies of these nanoparticles were homogeneous and agglomerated. The diffractions in the inset were exhibited for the polycrystalline rings that in agreement with the XRD results. The particle sizes from XRD (Figure 4.21 and Figure 4.22) seem to be increased with increasing calcination temperatures as expected. From the TEM images, the average particle size was  $14.99 \pm 0.87$  nm as given in Figure 4.23(b). It was larger than that calculated from XRD peaks.

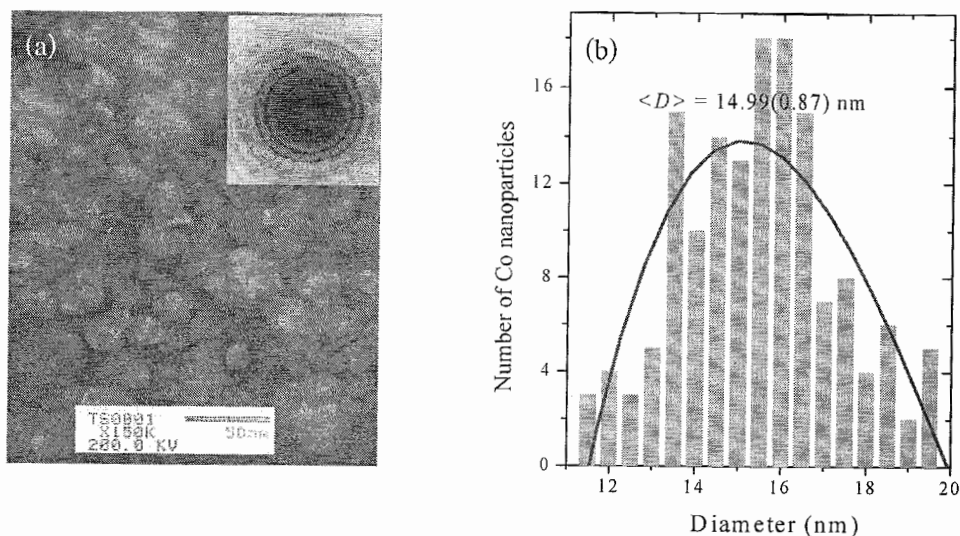
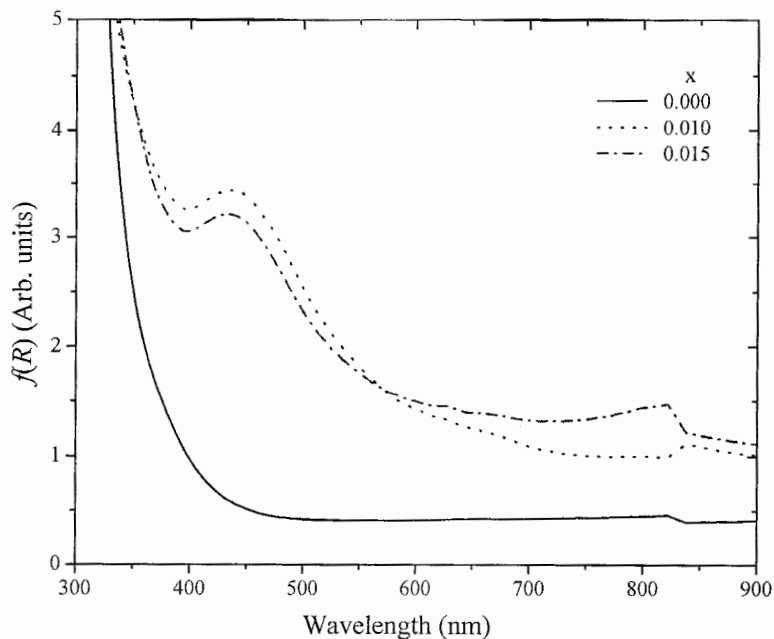


**Figure 4.23** (a) TEM images of  $\text{Sn}_{0.990}\text{Co}_{0.010}\text{O}_{2-\delta}$  calcined at 973 K and (b) measured Co nanoparticle size distribution corresponding to the TEM image shown in (a).

#### 4.2.5 Optical Properties

Diffuse reflectance measurement was employed to study the Co coping effect on the optical properties of the  $\text{SnO}_2$ . The diffuse reflectance spectra of the  $\text{Sn}_{1-x}\text{Co}_x\text{O}_{2-\delta}$  samples calcined at 873 K were illustrated in Figure 4.24. The band edges of the samples were observed at around 630 and 450 nm. These edges were assigned to the  $d-d$  crystal-field transitions  ${}^4\text{T}_{1g}(\text{F}) \rightarrow {}^4\text{T}_{2g}(\text{F})$  and  ${}^4\text{T}_{1g}(\text{F}) \rightarrow {}^4\text{T}_{1g}(\text{P})$ , respectively. The appearances of these transitions were clearly suggested that the doped  $\text{Co}^{2+}$  ( $3d^7$ ) were in the high-spin state and under an octahedral coordination. The peaks at 870 nm were due to the filter change noise and had therefore no physical meaning [92].



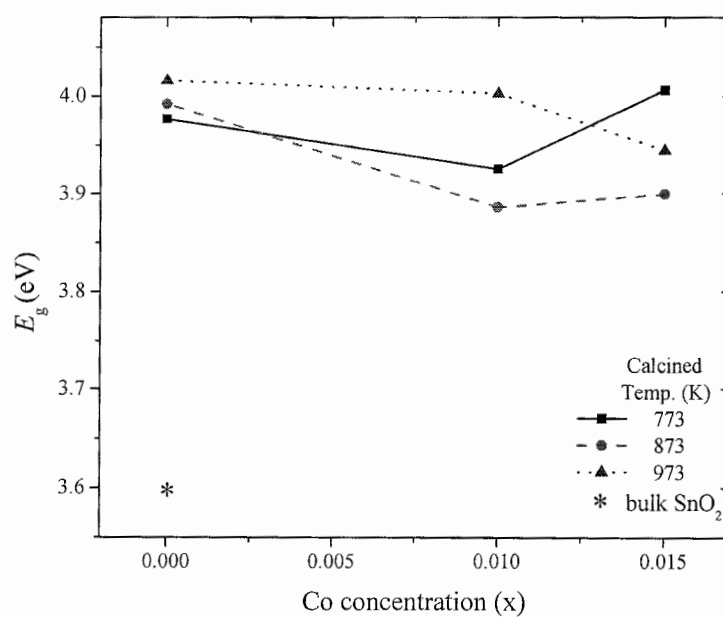


**Figure 4.24** Kubelka-Munk spectra of the  $\text{Sn}_{1-x}\text{Co}_x\text{O}_{2.8}$  samples calcined at 873 K with the different Cr concentration.

The  $\text{Sn}_{1-x}\text{Co}_x\text{O}_{2.8}$  colour was pale-yellow, which were corresponded to the reflectance spectra. Since  $\text{Sn}^{4+}$  in  $\text{SnO}_2$  was situated in octahedral coordination. These observations were clearly indicated that cobalt was substituted for Sn in  $\text{SnO}_2$  and the oxidation state of Co ions in the  $\text{Sn}_{1-x}\text{Co}_x\text{O}_{2.8}$  polycrystalline was  $\text{Co}^{2+}$ . However, the oxidation state of Cobalt was +3 in  $\text{Sn}_{0.95}\text{Co}_{0.05}\text{O}_2$  thin films deposited on Si by PLD [93]. The band gap energy of the  $\text{Sn}_{1-x}\text{Co}_x\text{O}_{2.8}$  samples, ( $E_g$ ) was calculated from their reflectance spectra by plotting  $(f(R)h\nu)^2$  versus photon energy. The linear part of the curve was extrapolated to  $(f(R)h\nu)^2 = 0$  to get band gap energy. The variation of the band gap energies was determined using the Kubelka-Munk function, listed in Table 4.5. The band gap energy was in the range of 3.89 - 4.01 eV. The variation of the band gap energies of the  $\text{Sn}_{1-x}\text{Co}_x\text{O}_{2.8}$  samples was shown in Figure 4.25. It was in a narrow range. Those results were indicated that the substitution of Co into Sn site was less effect to  $E_g$  of  $\text{SnO}_2$ . The values of  $E_g$  were in a slightly larger than those reported by Bauaine *et al.* [92]. For all of the samples investigated, the band gap energies were much larger than those of the bulk pure  $\text{SnO}_2$  (3.6 eV). It was confirmed that the  $\text{Sn}_{1-x}\text{Co}_x\text{O}_{2.8}$  samples in nanometer scale could be synthesized by the autocombustion technique.

**Table 4.5** Band Gap Energy,  $E_g$  (eV) of the  $\text{Sn}_{1-x}\text{Co}_x\text{O}_{2-\delta}$  samples

| Compound  | Calcined Temperature (K) | $E_g$ (eV) |
|---|--------------------------|------------|
| $\text{SnO}_2$  | 773                      | 3.98       |
|   | 873                      | 3.99       |
|   | 973                      | 4.02       |
| $\text{Sn}_{0.990}\text{Co}_{0.010}\text{O}_{2-\delta}$ | 773                      | 3.93       |
|   | 873                      | 3.89       |
|   | 973                      | 4.00       |
| $\text{Sn}_{0.985}\text{Co}_{0.015}\text{O}_{2-\delta}$ | 773                      | 4.01       |
|   | 873                      | 3.90       |
|   | 973                      | 3.95       |

**Figure 4.25** Band gap energy ( $E_g$ ) of the  $\text{Sn}_{1-x}\text{Co}_x\text{O}_{2-\delta}$  samples calcined at different temperatures and with the varying Co concentrations.

#### 4.2.6 Magnetic Measurements

The plot of magnetization ( $M$ ) as a function of magnetic field ( $H$ ) at room temperature of  $\text{Sn}_{0.995}\text{Co}_{0.005}\text{O}_{2-\delta}$  nanoparticles with the variation of calcined temperatures were depicted in Figure 4.26. The data have also been corrected for the diamagnetic contribution due to the plastic sample holder. A weak ferromagnetic interaction at room temperature with remanence ratio ( $M_R/M_S$ ) of about 0.53 and coercive field,  $H_C$  of 0.9 kOe were shown in the nanoparticles sample calcined at 773 K. The remanence ratio of the  $\text{Sn}_{0.995}\text{Co}_{0.005}\text{O}_{2-\delta}$  samples were increased from 0.70 to 0.72 and also the coercive field were increased from 1.2 kOe to 1.3 kOe as the calcined temperatures were increased from 873 K to 973 K. These results were indicated that the ferromagnetic ordering was increased as the calcination temperatures increasing. It was important to note that the well-defined hysteresis loop was observed for the  $\text{Sn}_{0.995}\text{Co}_{0.005}\text{O}_{2-\delta}$  sample calcined at 973 K. The saturation magnetization,  $M_S$  in this sample was almost  $0.11 \mu_B/\text{Co}$ . It was concluded that the calculations  $M_S$  were made based on the nominal Co concentration. The  $M_S$  value was equivalent to the  $\text{Sn}_{0.995}\text{Co}_{0.005}\text{O}_{2-\delta}$  nanoparticles prepared *via* coprecipitation as reported by Punnoose and Hay [53].

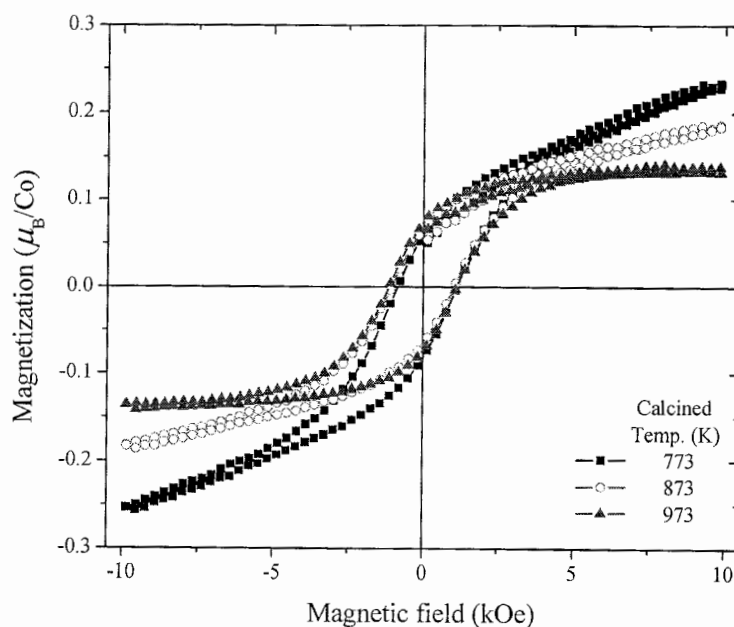


**Figure 4.26** Magnetization ( $M$ ) at room temperature of  $\text{Sn}_{0.995}\text{Co}_{0.005}\text{O}_{2-\delta}$  calcined at 773, 873 and 973 K.

For the question considering the formation of magnetic clusters, Hong *et al.* [15] did not observe any nanoparticle-sizes cluster on the surface. Further, the observed value of the moment in their samples was small compared to the value of  $1.67 \mu_B/\text{Co}$  expected for Co metal. In this work, the values of 0.09, 0.10 and  $0.11 \mu_B/\text{Co}$  in  $\text{Sn}_{0.995}\text{Co}_{0.005}\text{O}_{2.8}$  calcined at 773, 873 and 973 K, respectively, were relatively smaller compared to those expected for Co metal or those for small Co clusters ( $\sim 2.1 \mu_B/\text{Co}$ ) [94]. However, Ogale *et al.* [51] could obtain even much higher values of the magnetic moment in Co doped  $\text{SnO}_2$  films. Note that they did not attribute the higher values to the presence of clusters but to the quenched orbital moment of Co. In exchange mechanism, Coey *et al.* [55] have proposed that the exchange was mediated by carriers in a spin split impurity band. They pointed out that the oxygen vacancies were played an important role in magnetic properties. It might also induce in another valence state of Sn, assuming Co in a valence state of 2. Therefore, these data though could not rule out the presence of Co clusters, pointed out the important role played by oxygen defects.

As seen in Figure 4.26, the worst moment was detected on the sample calcined at 773 K with a coercivity at about 900 Oe and remenence ratio ( $M_R/M_S$ ) of about 0.58 (0.66 and 0.68 for calcined samples at 873 and 973 K, respectively). As those results, the sample calcined at 773 K nearby has not measured. The room temperature hysteresis loops of  $\text{Sn}_{0.990}\text{Co}_{0.010}\text{O}_{2.8}$  calcined at 873 and 973 K were illustrated in Figure 4.27.

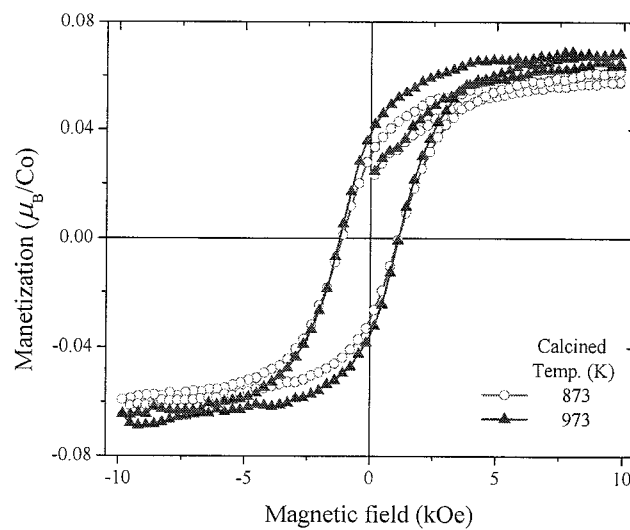


**Figure 4.27** Magnetization ( $M$ ) at room temperature of  $\text{Sn}_{0.990}\text{Co}_{0.010}\text{O}_{2.8}$  calcined at 873 and 973 K.

The values of  $M_s$  of  $\text{Sn}_{0.990}\text{Co}_{0.010}\text{O}_{2.8}$  were remained almost to unchanged in the 873 and 973 K calcined temperature with the  $M_s$  value of  $0.05 \mu_B/\text{Co}$ . Since  $M_s$  was proportional to the number of  $\text{Co}^{2+}$  spin participating in the ordered magnetic state, it was indicated that most of the  $\text{Co}^{2+}$  ions were still within the individual  $\text{Sn}_{0.990}\text{Co}_{0.010}\text{O}_{2.8}$  nanoparticles. The values of  $M_R$  were 0.03 and  $0.04 \mu_B/\text{Co}$  and the values of  $H_C$  were 1,100 and 1,300 Oe for the sample calcined at 873 and 973 K, respectively. The well defined hysteresis loops of these samples were occurred, indicating a ferromagnetic behavior with remanance ratio of 0.61 and 0.68, respectively. In this case, the more clearly ferromagnetic behavior was occurred in  $\text{Sn}_{0.990}\text{Co}_{0.010}\text{O}_{2.8}$  calcined at 973 K. Furthermore, oxygen vacancy was played in important rule for ferromagnetism.

The magnetizations at room temperature of  $\text{Sn}_{0.985}\text{Co}_{0.015}\text{O}_{2.8}$  calcined at 873 and 973 K as a function of the magnetic field were shown in Figure 4.28. The saturated magnetizations were 0.04 and  $0.07 \mu_B/\text{Co}$ , the  $M_R$  value of 0.03 and  $0.04 \mu_B/\text{Co}$  and the  $H_C$  values of 1,300 and 1,100 Oe for  $\text{Sn}_{0.985}\text{Co}_{0.015}\text{O}_{2.8}$  calcined at 873 and 973 K, respectively. These samples with well defined hysteresis loops were indicated that a fraction of the doped  $\text{Co}^{2+}$  ions was still incorporated in  $\text{SnO}_2$  in the individual particles and participate in the ordered ferromagnetic state.

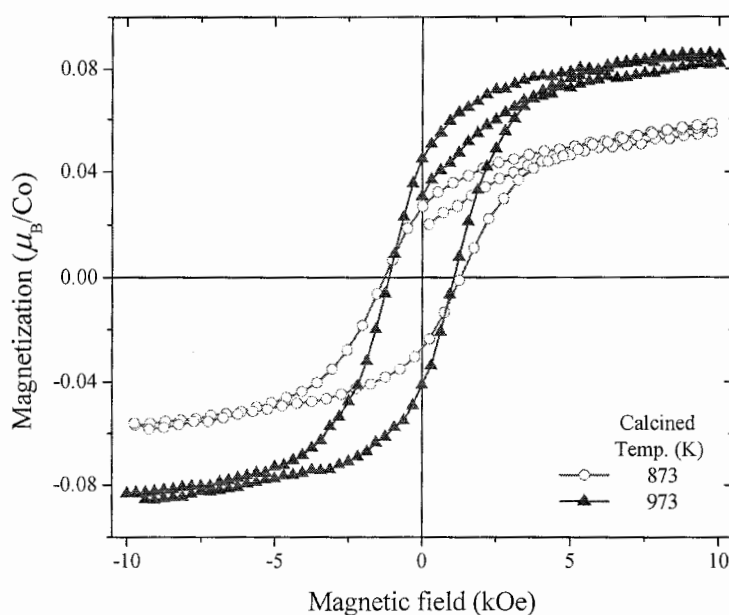


**Figure 4.28** Magnetization ( $M$ ) at room temperature of  $\text{Sn}_{0.985}\text{Co}_{0.015}\text{O}_{2.8}$  calcined at 873 and 973 K.

In general, the values of  $H_C$ ,  $M_R$  and  $M_S$  of  $\text{Sn}_{1-x}\text{Co}_x\text{O}_{2.8}$  were gradually increased with increasing calcined temperatures. Based on this result,  $\text{Sn}_{1-x}\text{Co}_x\text{O}_2$  [52-54] prepared at temperatures above 873 K might be oxygen rich while those samples prepared at lower temperature might be largely oxygen deficient and therefore there were a higher carrier concentration producing the observed ferromagnetism. However, these  $\text{Sn}_{1-x}\text{Co}_x\text{O}_{2.8}$  samples calcined at 973 K were clearly generated for ferromagnetic behavior. The complete absence of ferromagnetic was attributed to a presumably high oxygen stoichiometry and low carrier concentration.

The room temperature magnetization as a function of magnetic field of the  $\text{Sn}_{1-x}\text{Co}_x\text{O}_{2.8}$  samples with  $x = 0.005$ , 0.010 and 0.015 calcined at 973 K was illustrated in Figure 4.29. A constant saturation magnetization of  $0.06 - 0.07 \mu_B/\text{Co}$  and the  $M_R$  value of  $0.04 \mu_B/\text{Co}$  were appeared in these samples with  $x = 0.010$  and 0.015. In  $\text{Sn}_{0.995}\text{Co}_{0.005}\text{O}_{2.8}$  calcined at 973 K, the value of  $M_S$  and  $M_R$  were  $0.11 \mu_B/\text{Co}$  and  $0.08 \mu_B/\text{Co}$ , respectively. The  $H_C$  value of the samples with  $x = 0.005$  and 0.010 was 1,300 Oe, whereas a remarkable decrease to a value of 1,100 Oe was observed after the sample was doped with  $x = 0.015$ . These samples remained almost unchanged in remanence ratio of 0.67 - 0.68.

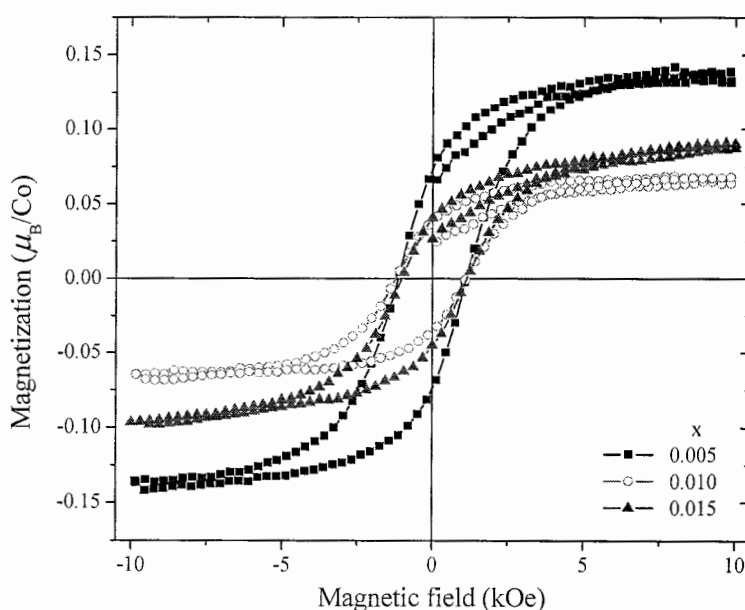


**Figure 4.29** Magnetization ( $M$ ) at room temperature of the  $\text{Sn}_{1-x}\text{Co}_x\text{O}_{2.8}$  ( $x \leq 0.015$ ) samples calcined at 973 K.

### 4.3 Iron-doped tin oxide ( $\text{Sn}_{1-x}\text{Fe}_x\text{O}_{2-\delta}$ )

#### 4.3.1 X-ray Diffraction Studies

Powder X-ray diffraction (XRD) patterns at room temperature of  $\text{Sn}_{1-x}\text{Fe}_x\text{O}_{2-\delta}$  ( $0 \leq x \leq 0.30$ ) samples calcined at 873 K were shown in Figure 4.30. The main phase of these nanoparticles was rutile  $\text{SnO}_2$  structure. It was worth noting that the samples were single phase without any foreign oxides or precipitated unreacted starting materials. This result suggested that Fe was incorporated completely into the  $\text{SnO}_2$  matrices. The systematically absent reflections of the diffraction spectra were consistent to tetragonal rutile structure of  $\text{SnO}_2$  with space group  $P42_1/mnm$ . Interestingly, similar good XRD signatures which was  $\text{SnO}_2$  ( $x = 0.000$ ), were obtained even for powders with Fe concentration as high as 30% ( $x = 0.30$ ) although  $\text{Sn}_{0.95}\text{Fe}_{0.05}\text{O}_{2-\delta}$  prepared by a solid-state reaction showed the XRD patterns of  $\text{SnO}_2$  with a trace of  $\alpha\text{-Fe}_2\text{O}_3$  [55]. However, in this case,  $\text{Fe}_2\text{O}_3$  was not detected due to the low Fe dopant concentration and to the solid solution formed.

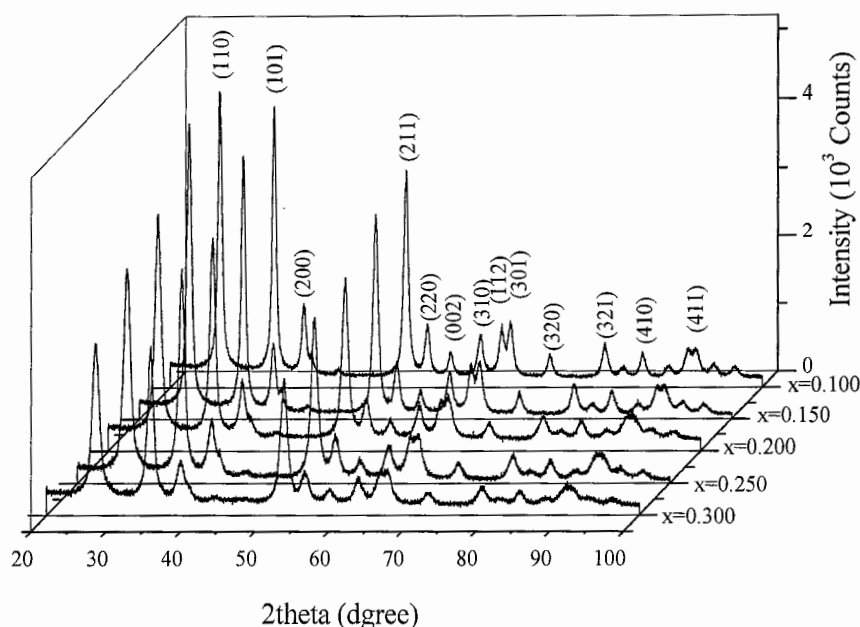


**Figure 4.30** X-ray Diffraction (XRD) patterns of the  $\text{Sn}_{1-x}\text{Fe}_x\text{O}_{2-\delta}$  ( $x \leq 0.30$ ) samples calcined at 973 K.

The crystallinity of Fe-doped  $\text{SnO}_2$  was increased as increasing calcination temperature with more clearly a rutile structure as seen in Figure 4.31. In addition, the intensities of all the peaks corresponding to the cassiterite phase (110) were decreased after Fe doping, shown in Figure 4.32. Since the atomic scattering factor of Sn was higher than Fe [87]. At even higher Fe content, a decrease in the XRD intensity was encountered.

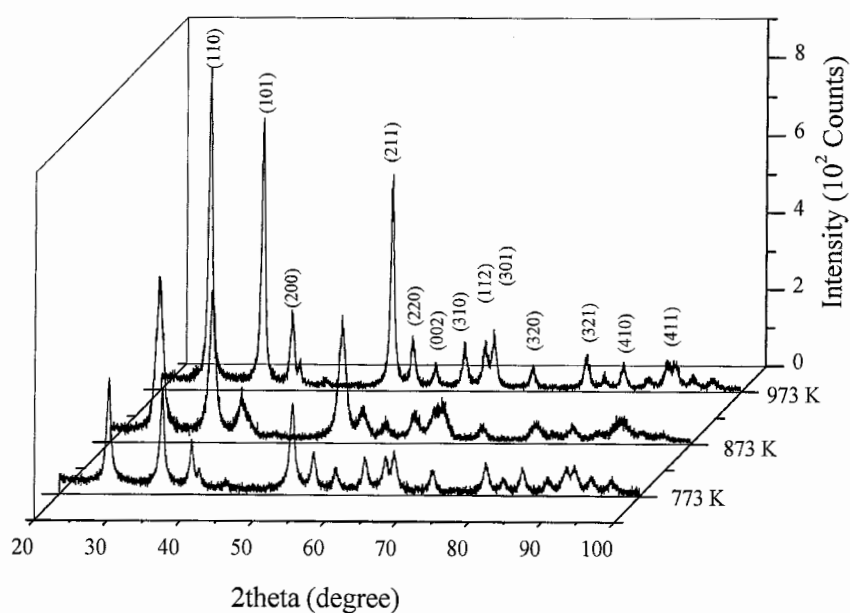


**Figure 4.31** X-ray Diffraction patterns of the  $\text{Sn}_{0.990}\text{Fe}_{0.010}\text{O}_{2.8}$  samples with the variation of calcined temperatures.



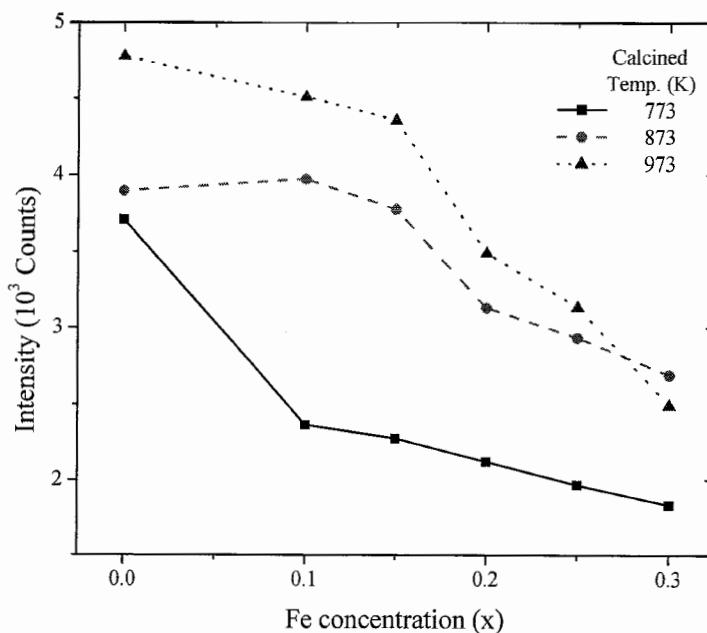


**Figure 4.32** Maximum intensities in the (110) of the  $\text{Sn}_{1-x}\text{Fe}_x\text{O}_{2.8}$  ( $x \leq 0.30$ ) samples calcined at 773, 873 and 973 K.

#### 4.3.2 The Rietveld refinement

The difference of the observed and the calculated X-ray diffraction (XRD) patterns of the  $\text{Sn}_{1-x}\text{Fe}_x\text{O}_{2.8}$  samples with  $x \leq 0.30$  calcined at 973 K were displayed in Figure 4.33. In the refining process, the tetragonal rutile  $\text{SnO}_2$  structure was selected as starting model structure. Fe ions were assumed to incorporate into the  $\text{SnO}_2$  lattice and occupy the Sn sites. The resulting lattice parameters and the related factors obtained from the Rietveld refinement of these Fe-doped samples were tabulated in Table 4.6 and Table 4.7.

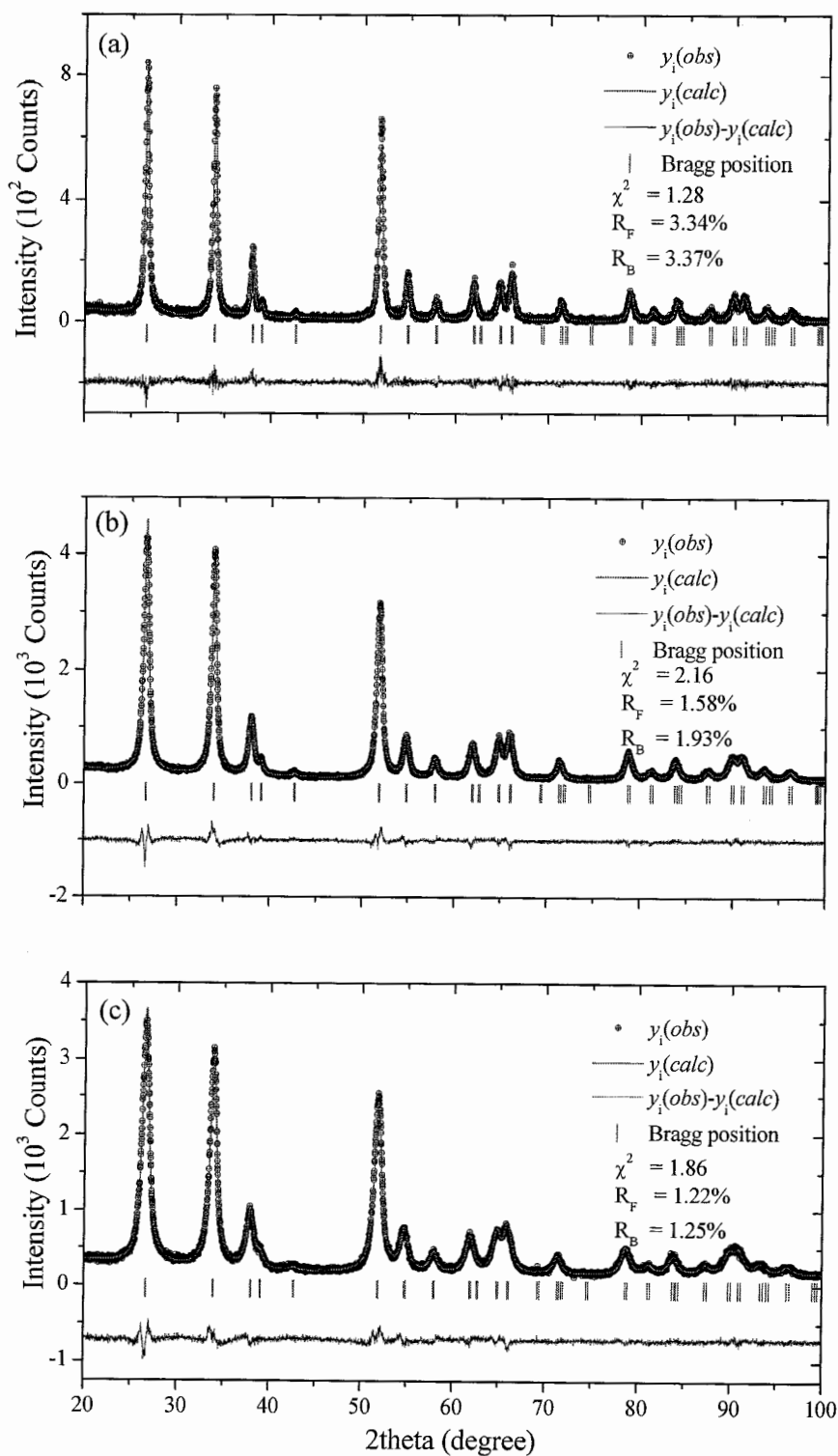


**Figure 4.33** X-ray diffractograms of (a)  $Sn_{0.990}Fe_{0.010}O_{2.8}$ , (b)  $Sn_{0.900}Fe_{0.100}O_{2.8}$  and (c)  $Sn_{0.800}Fe_{0.200}O_{2.8}$  calcined at 973 K. Data points were indicated by solid circles, while the calculated patterns were shown as a continuous line. The positions of the reflections were indicated with the vertical lines below the patterns.

**Table 4.6** The Rietveld refinement crystallographic data of the  $\text{Sn}_{1-x}\text{Fe}_x\text{O}_{2\delta}$  ( $x = 0.005, 0.010$  and  $0.015$ ) samples calcined at 773, 873 and 973 K. The space group  $\text{P42}/\text{mm}$  was used for all samples. Sn/Cr was occupied at  $(0, 0, 0)$  and  $\text{O}^{2-}$  was occupied at  $(x, y, 0)$  while  $x$  was equal to  $y$ . The numbers in the parenthesis were estimated standard deviations to the last significant digit.

| Compound                           | $\text{Sn}_{0.995}\text{Fe}_{0.005}\text{O}_{2\delta}$ |           |           | $\text{Sn}_{0.990}\text{Fe}_{0.010}\text{O}_{2\delta}$ |           |           | $\text{Sn}_{0.985}\text{Fe}_{0.015}\text{O}_{2\delta}$ |           |           |
|------------------------------------|--|-----------|-----------|--|-----------|-----------|--|-----------|-----------|
| Calced Temp. (K)                   | 773  | 873       | 973       | 773  | 873       | 973       | 773  | 873       | 973       |
| Parameters                         |  |           |           |  |           |           |  |           |           |
| $a = b$ (Å)                        | 4.7409(6)  | 4.7390(6) | 4.7394(6) | 4.7373(3)  | 4.7359(3) | 4.7369(3) | 4.7379(2)  | 4.7376(2) | 4.7377(2) |
| $c$ (Å)                            | 3.1896(4)  | 3.1892(4) | 3.1900(5) | 3.1871(2)  | 3.1854(2) | 3.1868(3) | 3.1869(2)  | 3.1867(2) | 3.1866(2) |
| Volume (Å <sup>3</sup> )           | 71.69(2)   | 71.63(2)  | 71.65(2)  | 71.52(1)   | 71.45(1)  | 71.51(1)  | 71.54(1)   | 71.52(1)  | 71.53(1)  |
| $\text{O}^{2-}$ position ( $x$ )   | 0.304(1)   | 0.302(1)  | 0.303(1)  | 0.304(1)   | 0.304(1)  | 0.300(1)  | 0.300(1)   | 0.303(1)  | 0.303(1)  |
| $B_{\text{iso}}$ (Å <sup>2</sup> ) | 0.23(1)  | 0.23(1)   | 0.23(1)   | 0.23(1)  | 0.23(1)   | 0.23(1)   | 0.24(1)  | 0.24(1)   | 0.23(1)   |
| $R_p$ (%)                          | 15.2   | 15.3      | 14.8      | 13.9   | 14.5      | 15.4      | 11.6   | 15.3      | 13.8      |
| $R_{\text{wp}}$ (%)                | 20.0   | 20.1      | 19.2      | 19.1   | 20.0      | 20.2      | 13.5   | 20.4      | 19.0      |
| $R_{\text{exp}}$ (%)               | 18.03  | 18.18     | 17.93     | 17.38  | 17.49     | 18.04     | 9.38   | 18.16     | 17.18     |
| $R_B$ (%)                          | 3.29   | 3.47      | 3.19      | 3.44   | 3.61      | 3.37      | 5.52   | 4.62      | 2.99      |
| $R_F$ (%)                          | 2.59   | 2.81      | 2.42      | 3.13   | 3.36      | 3.34      | 2.84   | 3.38      | 2.99      |
| $\chi^2$                           | 1.23   | 1.22      | 1.15      | 1.26   | 1.36      | 1.28      | 2.25   | 1.39      | 1.35      |
| DW-stat                            | 1.689  | 1.74      | 1.74      | 1.83   | 1.77      | 1.76      | 1.08   | 1.86      | 1.86      |

**Table 4.7** The Rietveld refinement crystallographic data of the  $\text{Sn}_{1-x}\text{Fe}_x\text{O}_{2-\delta}$  ( $x = 0.100, 0.200$  and  $0.300$ ) samples calcined at 773, 873 and 973 K. The space group P42/mnm was used for all samples. Sn/Cr was occupied at (0, 0, 0) and  $\text{O}^{2-}$  was occupied at ( $x, y, 0$ ) while  $x$  was equal to  $y$ . The numbers in the parenthesis were estimated standard deviations to the last significant digit.

| Compound                           | $\text{Sn}_{0.900}\text{Fe}_{0.100}\text{O}_{2-\delta}$ |           |           | $\text{Sn}_{0.800}\text{Fe}_{0.200}\text{O}_{2-\delta}$ |           |           | $\text{Sn}_{0.700}\text{Fe}_{0.300}\text{O}_{2-\delta}$ |           |           |
|------------------------------------|---|-----------|-----------|---|-----------|-----------|---|-----------|-----------|
| Calcined Temp. (K)                 | 773   | 873       | 973       | 773   | 873       | 973       | 773   | 873       | 973       |
| Parameters                         |   |           |           |   |           |           |   |           |           |
| $a = b$ (Å)                        | 4.7361(4)   | 4.7371(2) | 4.7370(2) | 4.7410(5)   | 4.7394(3) | 4.7392(2) | 4.7403(6)   | 4.7412(4) | 4.7375(3) |
| $c$ (Å)                            | 3.1868(3)   | 3.1853(2) | 3.1846(1) | 3.1898(4)   | 3.1848(3) | 3.1834(2) | 3.1866(4)   | 3.1846(3) | 3.1809(3) |
| Volume (Å <sup>3</sup> )           | 71.48(1)  | 71.48(1)  | 71.46(1)  | 71.70(1)  | 71.54(1)  | 71.50(1)  | 71.61(2)  | 71.59(1)  | 71.39(1)  |
| $\text{O}^{2-}$ position ( $x$ )   | 0.302(1)  | 0.304(1)  | 0.301(1)  | 0.302(1)  | 0.307(1)  | 0.303(1)  | 0.297(1)  | 0.304(9)  | 0.301(1)  |
| $B_{\text{iso}}$ (Å <sup>2</sup> ) | 0.22(1)   | 0.23(1)   | 0.22(1)   | 0.21(1)   | 0.22(1)   | 0.21(1)   | 0.20(1)   | 0.20(1)   | 0.20(1)   |
| $R_p$ (%)                          | 8.51  | 8.94      | 9.25      | 9.14  | 9.29      | 9.29      | 9.75  | 9.59      | 11.7      |
| $R_{\text{wp}}$ (%)                | 10.1  | 10.4      | 10.8      | 10.5  | 10.6      | 10.5      | 10.9  | 10.6      | 12.4      |
| $R_{\text{exp}}$ (%)               | 7.32  | 7.01      | 7.39      | 7.40  | 7.25      | 7.73      | 7.98  | 7.42      | 9.20      |
| $R_B$ (%)                          | 1.40  | 2.27      | 1.93      | 1.38  | 2.05      | 1.25      | 1.71  | 1.51      | 1.93      |
| $R_F$ (%)                          | 1.06  | 1.75      | 1.58      | 1.04  | 1.51      | 1.22      | 1.16  | 1.32      | 1.54      |
| $\chi^2$                           | 1.90  | 2.24      | 2.16      | 2.00  | 2.13      | 1.86      | 1.88  | 2.04      | 1.82      |
| DW-stat                            | 1.08  | 0.92      | 1.04      | 1.03  | 1.00      | 1.12      | 1.04  | 0.95      | 1.12      |

The lattice parameters  $a$  and  $c$  showed a very slightly change in Table 4.6 that corresponding to the lattice parameters in  $\text{Sn}_{0.95}\text{Fe}_{0.05}\text{O}_2$  at  $x = 0.005 - 0.015$  although there were a sharp decrease at  $x > 0.015$  [56]. In addition, the lattice volumes in  $\text{Sn}_{0.95}\text{Fe}_{0.05}\text{O}_2$  were quite constant corresponding to the study which the unit cell volume was minimized at 873 K [56]. A constant in the volume the  $\text{Sn}_{1-x}\text{Fe}_x\text{O}_{2.8}$  samples was appeared in all calcined temperature samples. These results suggested that the Fe doping could prevent the growth of  $\text{SnO}_2$  crystallites. Tetragonality ( $a/c$ ) in Table 4.6 and Table 4.7 was increased with increasing Fe content although  $a/c$  was quite constant at the lower Fe doping. To further confirmed substitution of  $\text{Fe}^{3+}$  ( $3d^5$ ) for  $\text{Sn}^{4+}$  in the cell, the unit cell refinements have been performed. Due to the ionic radius of  $\text{Fe}^{3+}$  ( $\sim 0.65 \text{ \AA}$ ) smaller than that of  $\text{Sn}^{4+}$  ( $\sim 0.69 \text{ \AA}$ ) [88], the tetragonality ( $a/c$ ) of these samples were decreased with increasing Fe concentration. Substitution of  $\text{Sn}^{4+}$  ions with  $\text{Fe}^{3+}$  ions was expected to reduce the interatomic spacing significantly, justifying the initial contraction of the lattice.

#### 4.3.3 Crystallite sizes

The average particle sizes ( $\langle D \rangle$ ) for all the samples were calculated using both Scherrer's equation and Williamson-Hall Plot (WHP) method. Calculation steps for the  $\text{Sn}_{1-x}\text{Fe}_x\text{O}_{2.8}$  samples were similar to calculation of the  $\text{Sn}_{1-x}\text{Cr}_x\text{O}_{2.8}$  samples

### Crystallite size calculated by Scherrer's Equation

Calculations of crystallite sizes of the  $\text{Sn}_{1-x}\text{Fe}_x\text{O}_{2.8}$  samples with  $x \leq 0.30$  calcined at 773, 873 and 973 K by Scherrer's Equation were summarized in Figure 4.34.

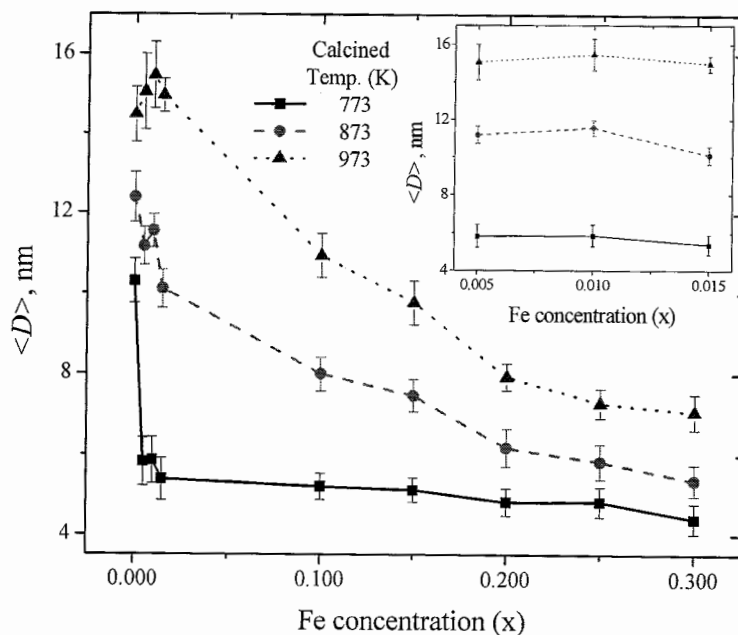


**Figure 4.34** Crystallite sizes of the  $\text{Sn}_{1-x}\text{Fe}_x\text{O}_{2.8}$  ( $x \leq 0.30$ ) samples calcined at 773, 873 and 973 K calculated by Scherrer's equation. Inset: enlarge for the  $\text{Sn}_{1-x}\text{Fe}_x\text{O}_{2.8}$  ( $x \leq 0.015$ ) samples.

The amount of doped iron affected crystal size of the nanoparticles. These estimates showed that the crystallite sizes were increased with increasing of the calcined temperature due to agglomeration of growing crystal. The average crystallite size was in the range of 5 - 15 nm. On increasing the Fe concentration, the average particle size was further reduced. This effect in conjunction with the smaller ionic radius of  $\text{Fe}^{3+}$  ion in comparison to  $\text{Sn}^{4+}$  ion could disturb long range crystallographic ordering, and thus reducing the crystallite size. The presence of iron ions in the crystallographic structure was increased the formation of oxygen vacancies as required by the charge balance.

### Crystallite size calculated by Williamson-Hall Plot (WHP) method

Crystallite sizes calculations of  $\text{Sn}_{1-x}\text{Fe}_x\text{O}_{2.8}$  samples with  $x \leq 0.30$  calcined at 773, 873 and 973 K by Williamson-Hall Plot method were shown in Figure 4.35. The crystallite sizes were increased as increasing calcination temperature similar to those obtained from Scherrer's equation. The average crystallite size was in the range of 5 - 18 nm. The reduction of the crystallite size suggested that Fe ion was replaced to Sn ion.

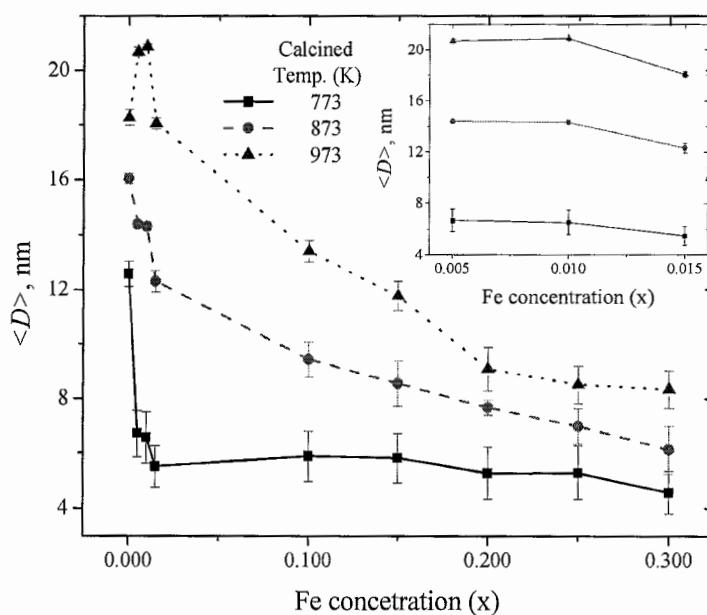


**Figure 4.35** Crystallite sizes of the  $\text{Sn}_{1-x}\text{Fe}_x\text{O}_{2.8}$  ( $x \leq 0.30$ ) samples calcined at 773, 873 and 973 K calculated by Williamson-Hall plot. Inset: enlarge for the  $\text{Sn}_{1-x}\text{Fe}_x\text{O}_{2.8}$  ( $x \leq 0.015$ ) samples.

#### 4.3.4 Microstructure

The TEM images of  $\text{Sn}_{0.900}\text{Fe}_{0.100}\text{O}_{2.8}$  calcined at 973 K was shown in Figure 4.36(a). A loose microstructure and a closely spherical-like nanoparticles with a partly agglomeration were appeared. The diffraction in the inset exhibited the polycrystalline rings that in agreement with the XRD patterns (Figure 4.30). The particle size distribution was determined by manually image analysis. The average particle size of  $\text{Sn}_{0.900}\text{Fe}_{0.100}\text{O}_{2.8}$  was of  $12.94 \pm 1.00$  nm as given in Figure 4.36(b). In addition, the average sizes for the  $\text{Sn}_{1-x}\text{Fe}_x\text{O}_{2.8}$  samples calcined at 973 K with  $x = 0.010, 0.200$  and  $0.300$  were  $15.26 \pm 1.97, 9.50 \pm 1.14$  and  $8.53 \pm 0.84$  nm, respectively. The crystallite sizes were decreased with Fe doping, in excellent agreement with XRD studies. However, the size estimated from TEM was slightly larger than that obtained from XRD data. In this case, four samples were chosen to take the TEM images for confirm nanocrystallinity and the particle sizes.

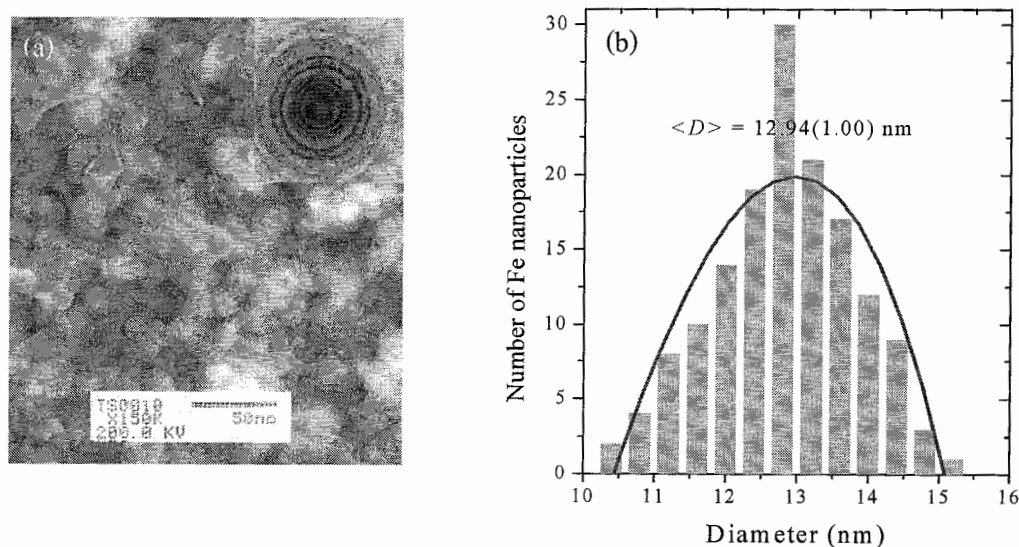


**Figure 4.36** (a) TEM images of  $\text{Sn}_{0.900}\text{Fe}_{0.100}\text{O}_{2.8}$  calcined at 973 K and (b) measured Fe nanoparticle size distribution corresponding to the TEM image shown in (a).



### 4.3.5 Optical Properties

The optical properties were characterized by measuring the diffuse reflection. The reflectance spectra of the  $\text{Sn}_{1-x}\text{Fe}_x\text{O}_{2.8}$  samples were shown in Figure 4.37. There were drastic changes in the spectra. Pale-yellow powders of the  $\text{Sn}_{1-x}\text{Fe}_x\text{O}_{2.8}$  samples were corresponded to the reflectance spectra. These spectra displayed a red shift in the band gap transition with increasing Fe dopant, similar to the  $\text{Fe}^{3+}$ -doped  $\text{SnO}_2$  *via* sol-gel hydrothermal route [95]. A red shifts of this type could be attributed to the charge transfer transitions between the  $\text{Fe}^{3+}$  *d*-electrons and the  $\text{SnO}_2$  conduction or valence band.

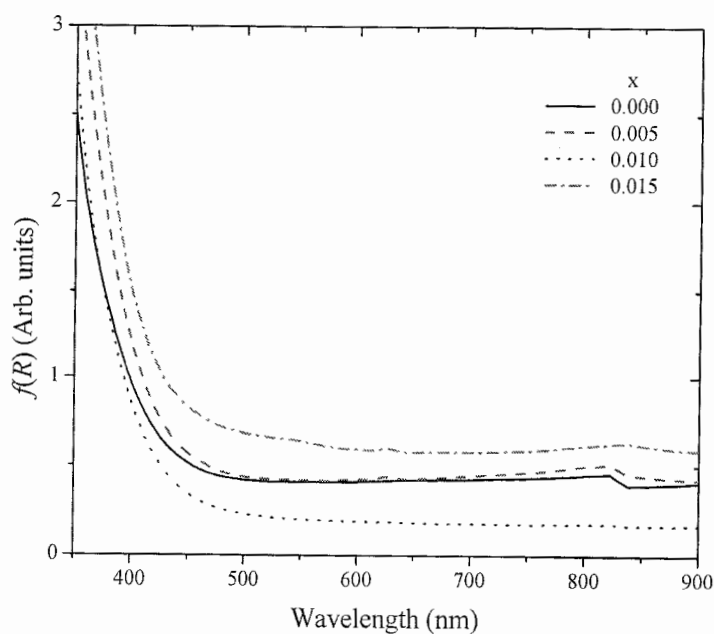


**Figure 4.37** Kubelka-Munk spectra of the  $\text{Sn}_{1-x}\text{Fe}_x\text{O}_{2.8}$  samples calcined at 873 with different Fe concentration.

The band gap energy could be determined by extrapolation to the zero of  $(f(R)h\nu)^2$ . The intercept to the plots would give a good approximation of the band gap energies for the direct band gap material. The variation of the band gap energies of the  $\text{Sn}_{1-x}\text{Fe}_x\text{O}_{2.8}$  samples were listed in Table 4.8, in the range of 3.77-3.98 eV

**Table 4.8** Band Gap Energy,  $E_g$  (eV) of the  $\text{Sn}_{1-x}\text{Fe}_x\text{O}_{2-\delta}$  samples

| Compound  | Calcined Temperature (K) | $E_g$ (eV) |
|---|--------------------------|------------|
| $\text{SnO}_2$  | 773                      | 3.98       |
|   | 873                      | 3.99       |
|   | 973                      | 4.02       |
| $\text{Sn}_{0.995}\text{Fe}_{0.005}\text{O}_{2-\delta}$ | 773                      | 3.91       |
|   | 873                      | 3.95       |
|   | 973                      | 3.96       |
| $\text{Sn}_{0.990}\text{Fe}_{0.010}\text{O}_{2-\delta}$ | 773                      | 3.98       |
|   | 873                      | 3.96       |
|   | 973                      | 3.93       |
| $\text{Sn}_{0.985}\text{Fe}_{0.015}\text{O}_{2-\delta}$ | 773                      | 3.96       |
|   | 873                      | 3.96       |
|   | 973                      | 3.95       |
| $\text{Sn}_{0.900}\text{Fe}_{0.100}\text{O}_{2-\delta}$ | 773                      | 3.85       |
|   | 873                      | 3.88       |
|   | 973                      | 3.87       |
| $\text{Sn}_{0.850}\text{Fe}_{0.150}\text{O}_{2-\delta}$ | 773                      | 3.86       |
|   | 873                      | 3.89       |
|   | 973                      | 3.86       |
| $\text{Sn}_{0.800}\text{Fe}_{0.200}\text{O}_{2-\delta}$ | 773                      | 3.89       |
|   | 873                      | 3.83       |
|   | 973                      | 3.83       |
| $\text{Sn}_{0.750}\text{Fe}_{0.250}\text{O}_{2-\delta}$ | 773                      | 3.77       |
|   | 873                      | 3.80       |
|   | 973                      | 3.87       |
| $\text{Sn}_{0.700}\text{Fe}_{0.300}\text{O}_{2-\delta}$ | 773                      | 3.89       |
|   | 873                      | 3.84       |
|   | 973                      | 3.83       |

A slightly change in the band gap values of the  $\text{Sn}_{1-x}\text{Fe}_x\text{O}_{2.8}$  samples with a very low doping Fe concentration ( $x \leq 0.015$ ) were illustrated in Figure 4.38. This result indicated that substitution of Fe into Sn site was less effect to  $E_g$  of  $\text{SnO}_2$ .

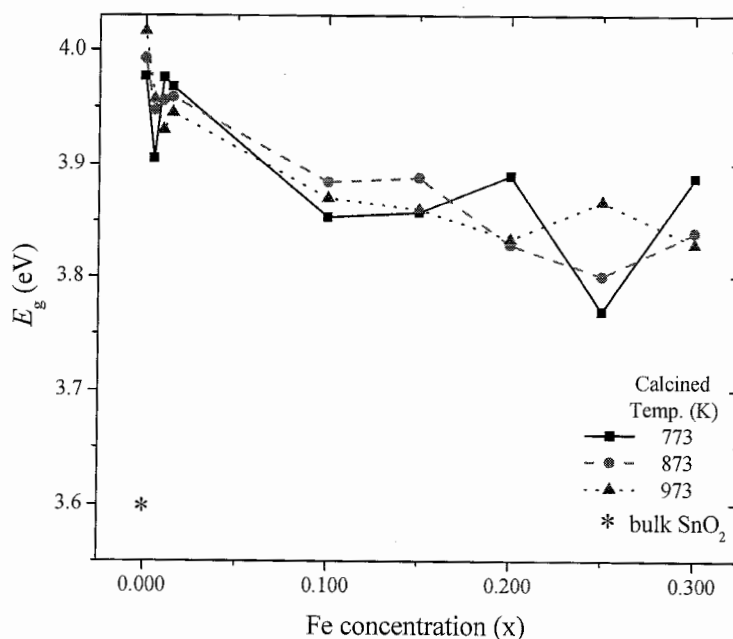


**Figure 4.38** Band gap energy ( $E_g$ ) of the  $\text{Sn}_{1-x}\text{Fe}_x\text{O}_{2.8}$  samples calcined at different temperatures and with varying Fe concentrations.

However, the band gap energies of the  $\text{Sn}_{1-x}\text{Fe}_x\text{O}_{2.8}$  samples were shifted to the lower value with increasing Fe dopant higher than 10%. This result could be explained on the basis of the  $sp-d$  exchange interaction between the band electrons and the localized  $d$  electrons of the  $\text{Fe}^{3+}$  ions substituting  $\text{Sn}^{4+}$  ions. The  $s-d$  and  $p-d$  exchange interactions gave rise to a negative and positive correction to the conduction and valence band edges, respectively, leading to a band gap narrowing. Moreover, the band gap energies were much larger than the bulk pure  $\text{SnO}_2$  (3.6 eV). This result confirmed that the  $\text{Sn}_{1-x}\text{Fe}_x\text{O}_{2.8}$  samples synthesized by the autocombustion technique could be prepared in nanometer scale.

#### 4.3.6 Magnetic Measurement

The magnetization ( $M$ ) of  $\text{Sn}_{0.995}\text{Fe}_{0.005}\text{O}_{2-\delta}$  calcined at 773, 873 and 973 K as a function of an applied magnetic field ( $H$ ) were depicted in Figure 4.39.

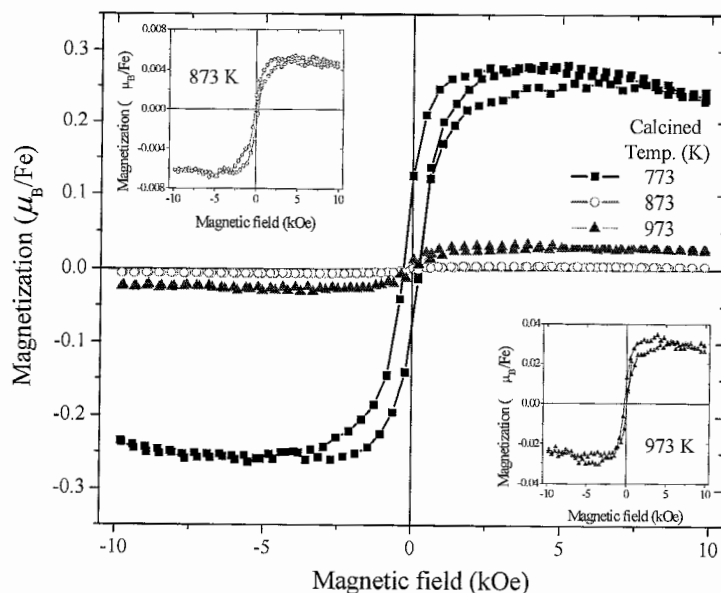


**Figure 4.39** Magnetization ( $M$ ) at room temperature of  $\text{Sn}_{0.995}\text{Fe}_{0.005}\text{O}_{2-\delta}$  calcined at 773, 873 and 973 K. Inset: enlarge the loops of  $\text{Sn}_{0.995}\text{Fe}_{0.005}\text{O}_{2-\delta}$  calcined at 873 and 973 K.

The data have been corrected for the diamagnetic contribution due to the sample holder. The magnetizations of all compounds were saturated at relatively low fields  $\sim 150$  Oe. A decrease in the ferromagnetic moment was independent on increasing calcined temperature, the magnetic moments were observed in a large change for calcined at 773 K ( $0.256 \mu_{\text{B}}/\text{Fe}$ ) and calcined at 873 K ( $0.006 \mu_{\text{B}}/\text{Fe}$ ) or calcined at 973 K ( $0.022 \mu_{\text{B}}/\text{Fe}$ ). The  $M_{\text{R}}$  values were 0.076, 0.001 and 0.006 for the samples calcined at 773, 873 and 973 K, respectively. This clearly established the fact that the ferromagnetic component was stronger when prepared at lower calcination temperatures, in excellent agreement with Punnoose *et al.* results discussed earlier [56]. Mathew *et al.* suggested that low annealing temperatures favored ferromagnetism, probably due to uniform distribution of the transition metal dopant ions in the host  $\text{SnO}_2$  lattice [96]. Moreover, they found that the complete disappearance of ferromagnetism in samples annealed at temperatures above 873 K ruled out of the formation of iron oxide. In Figure 4.39, the

best magnetic moment of about  $0.25 \mu_B/\text{Fe}$  for  $\text{Sn}_{0.995}\text{Fe}_{0.005}\text{O}_{2-\delta}$  calcined at 773 K, were decreased readily as Fe dopant ( $x$ ) was enhanced, in agreement with Fitzgerald *et al.* as reported previously [97]. The moments at low concentrations ( $x \leq 0.02$ ) approached or surpassed the spin-only values, and they could not be explained in terms of secondary impurity phases. In any case, Mn-, Fe- and Co-doped  $\text{SnO}_2$ , the moments at low concentrations far exceed those of all known ferromagnetic phases [97]. The coercivity ( $H_C$ ) of these samples calcined at 773, 873 and 973 K were about 280, 160 and 150 Oe, respectively, which were significantly different from the value of  $H_C = 1844$  Oe obtained for the pure hematite sample [56]. The small coercivity of polycrystalline samples indicated the intrinsically soft nature of these materials. It seems to be that the coercive field results from the magnetic correlation between iron particles instead of that of iron clusters.

The  $M$ - $H$  curves of  $\text{Sn}_{0.990}\text{Fe}_{0.010}\text{O}_{2-\delta}$  calcined at 773, 873 and 973 K were shown in Figure 4.40. The magnetic moments were 0.022 and  $0.045 \mu_B/\text{Fe}$  and the  $M_R$  values were 0.008 and  $0.007 \mu_B/\text{Fe}$  for the samples calcined at 773 and 873 K, respectively. Surprisingly, the ferromagnetic ordering completely disappeared and it became paramagnetic. This probably implied that when constraints on the samples were more relaxed, the ferromagnetism could be enormously reduced as found in Ni-doped  $\text{SnO}_2$  by PLD [98].

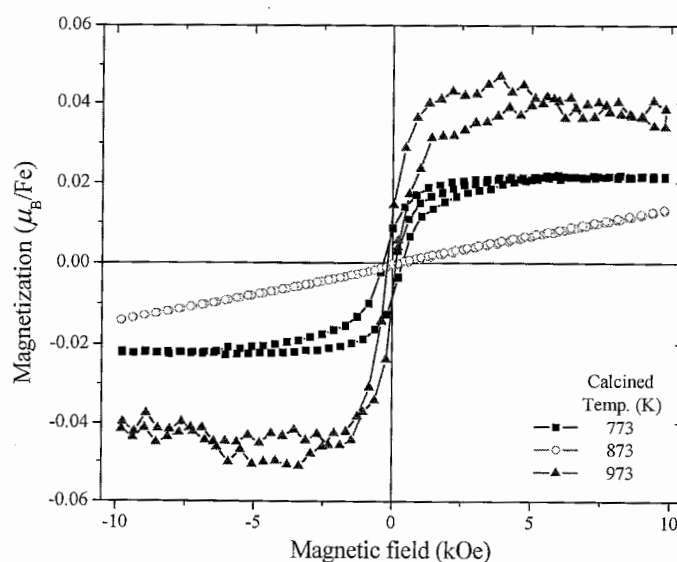


**Figure 4.40** Magnetization ( $M$ ) at room temperature of  $\text{Sn}_{0.990}\text{Fe}_{0.010}\text{O}_{2-\delta}$  calcined at 773, 873 and 973 K.

The magnetization ( $M$ ) as a function of an applied magnetic field ( $H$ ) of  $\text{Sn}_{0.985}\text{Fe}_{0.015}\text{O}_{2.8}$  calcined at 773, 873 and 973 K was illustrated in Figure 4.41. In the other hands, the samples lost the ferromagnetic ordering and formed diamagnetic behavior instead.

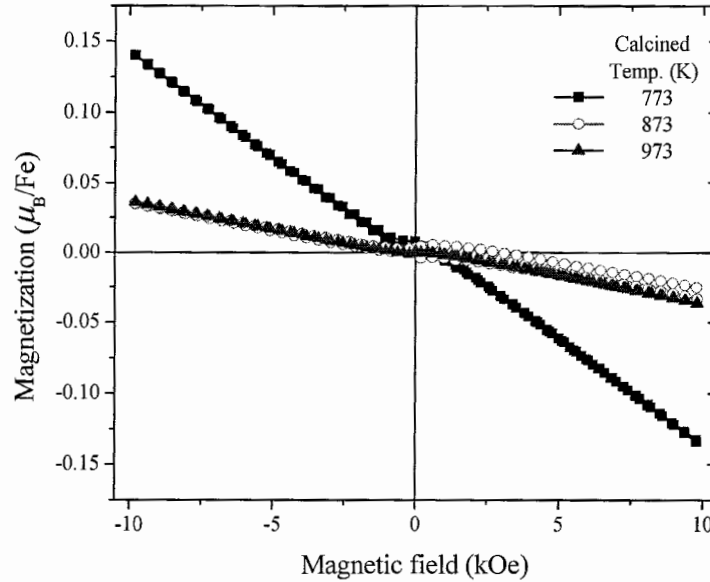


**Figure 4.41** Magnetization ( $M$ ) at room temperature of  $\text{Sn}_{0.985}\text{Fe}_{0.015}\text{O}_{2.8}$  calcined at 773, 873 and 973 K.

A typical VSM hysteresis loop taken at room temperature from the  $\text{Sn}_{1-x}\text{Fe}_x\text{O}_{2.8}$  samples with  $x = 0.100, 0.150, 0.200, 0.250$  and  $0.300$  calcined at 773 K was shown in Figure 4.42 with substantial different behavior. Clearly, there were two types of curves in different shapes. A weak ferromagnetic-like characteristic with a saturated magnetization of  $0.002 \mu_B/\text{Fe}$  was appeared in  $\text{Sn}_{0.900}\text{Fe}_{0.100}\text{O}_{2.8}$  calcined at 773 K. It corresponded to this sample synthesized by a polymerized complex method with  $M_s = 0.013 \text{ emu/g}$  ( $0.0017 \mu_B/\text{Fe}$ ) [99]. The other  $\text{Sn}_{1-x}\text{Fe}_x\text{O}_{2.8}$  samples showed that a hysteresis loop was very narrow and not saturated.

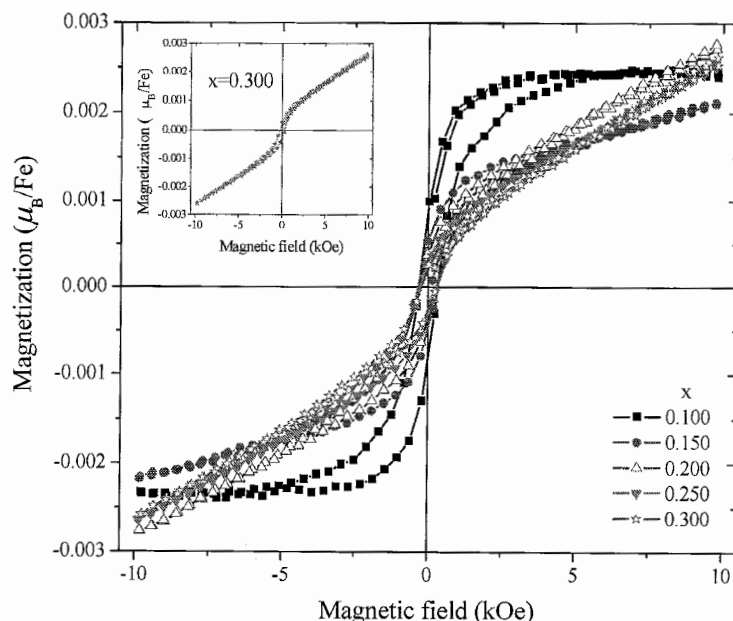


**Figure 4.42** Magnetization ( $M$ ) at room temperature of the  $\text{Sn}_{1-x}\text{Fe}_x\text{O}_{2.8}$  ( $0.100 \leq x \leq 0.300$ ) samples calcined at 773 K. Inset: enlarge the loop of  $\text{Sn}_{0.700}\text{Fe}_{0.300}\text{O}_{2.8}$ .

A rapid expansion of the  $\text{SnO}_2$  lattice and significant structural disorder were resulted in increasing the Fe doping to  $> 10\%$ . The ferromagnetic ordering might be destroyed with such enormous structural changes. These magnetizations showed a cycle typical of a superparamagnetic system, although the weak hysteresis observed indicated the presence of a small amount of a ferromagnetic component. This result suggested that Fe has been incorporated into  $\text{SnO}_2$  structure either substitutionally or interstitially. The coercivity ( $H_C$ ) was about 300 Oe, which was significantly different from the value of  $H_C = 1844$  Oe obtained for the pure hematite sample [56]. The existence of a significant coercivity in  $\text{Sn}_{1-x}\text{Fe}_x\text{O}_2$  samples was clearly ruled out their possible origin from nanoscale superparamagnetic particles of iron oxides [56]. It was well known that when magnetic materials were prepared in nanoscale sizes, they demonstrated superparamagnetic behavior characterized by hysteresis loops with zero coercivity above their blocking temperatures. This blocking behavior implied that there were precipitated ferromagnetic particles in the films which were partially responsible for the ferromagnetic property of Fe-doped  $\text{SnO}_2$ . Therefore, it was the most possible that the  $\text{Sn}_{1-x}\text{Fe}_x\text{O}_{2.8}$  samples with  $x > 0.100$  were superparamagnetism.

At the same time, the  $M$ - $H$  curves of the  $\text{Sn}_{1-x}\text{Fe}_x\text{O}_{2.8}$  samples with  $0.100 \leq x \leq 0.300$  calcined at 873 and 973 K were shown in Figure 4.43 and Figure 4.44, respectively. There were two types of curves in the different shapes similar to the samples calcined at 773 K (Figure 4.42). The presence of a very weak ferromagnetic-like characteristic ( $< 0.001 \mu_B/\text{Fe}$ ) was generated in the  $\text{Sn}_{0.900}\text{Fe}_{0.100}\text{O}_{2.8}$  samples calcined at both 873 and 973 K. A superparamagnetic behavior was demonstrated in the other  $\text{Sn}_{1-x}\text{Fe}_x\text{O}_{2.8}$  samples.

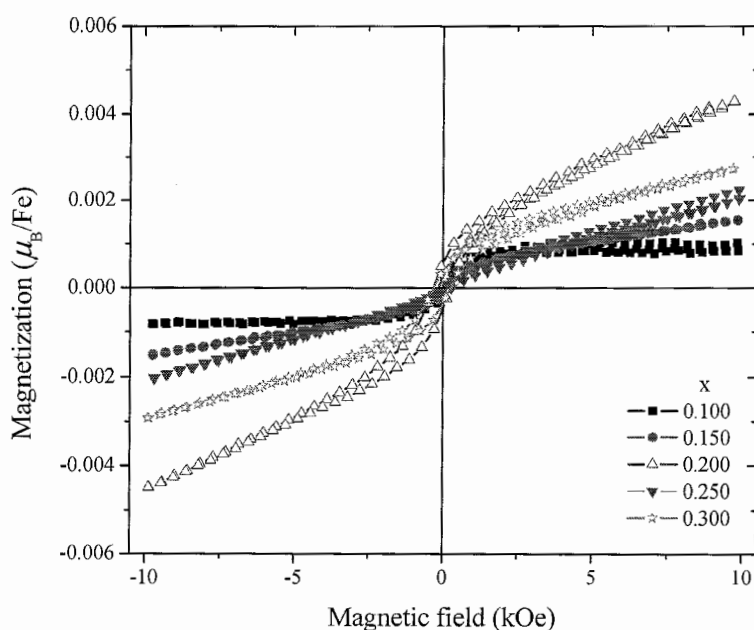


**Figure 4.43** Magnetization ( $M$ ) at room temperature of the  $\text{Sn}_{1-x}\text{Fe}_x\text{O}_{2.8}$  ( $0.100 \leq x \leq 0.300$ ) samples calcined at 873 K.



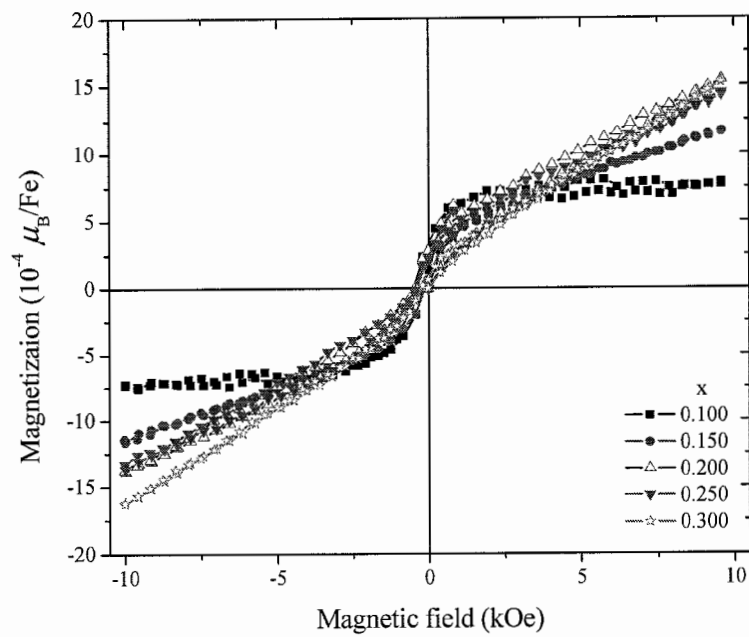


**Figure 4.44** Magnetization ( $M$ ) at room temperature of the  $\text{Sn}_{1-x}\text{Fe}_x\text{O}_{2-\delta}$  ( $0.100 \leq x \leq 0.300$ ) samples calcined at 973 K.

## CHAPTER V

### CONCLUSIONS

The nanoparticle  $\text{Sn}_{1-x}\text{TM}_x\text{O}_{2-\delta}$  powders (TM were Cr and Co with  $x \leq 0.015$  and Fe with  $x \leq 0.30$ ) were prepared by the autocombustion technique. All XRD patterns showed the rutile structure of  $\text{SnO}_2$  (JCPDS file: 41-1445) without any trace of an impurity phase. The peak positions did not show any measurable change, while the intensities of the peaks were decreased with increasing Co concentrations. All samples were a very broad XRD peaks due to their nanocrystalline behavior. The XRD intensities of these samples were increased as increasing calcination temperatures indicating that crystallinity of these samples were increased.

The crystallite sizes were calculated using the Scherrer's equation and the Williamson-Hall Plot method. The crystallite sizes were increased as increasing calcination temperatures indicating that the agglomerated powders were occurred during growing crystals. On increasing the TM concentration, the average particle size was decreased slightly with TM doping, in excellent agreement with TEM studies especially in Cr dopant. The presence of a nearly spherical-like nanoparticles with a partly agglomeration were showed by the TEM image. However, the particles sizes estimated from TEM were slightly larger than those obtained from XRD breadth. The average crystallite size was in the range of 5 - 20 nm. This confirmed that the  $\text{Sn}_{1-x}\text{TM}_x\text{O}_{2-\delta}$  samples could be synthesized in the nanometer level.

The absorption bands of  $d-d$  transition corresponding to the spin-allowed transitions in each metal, two absorption bands for  $\text{Cr}^{4+}$  ( $d^2$ ):  ${}^3\text{T}_{1g}(\text{F}) \rightarrow {}^3\text{T}_{2g}(\text{F})$  and  ${}^3\text{T}_{1g}(\text{F}) \rightarrow {}^3\text{T}_{1g}(\text{P})$  and two absorption bands for  $\text{Co}^{2+}$  ( $d^7$ ) that were ascribed to  ${}^4\text{T}_{1g}(\text{F}) \rightarrow {}^4\text{T}_{2g}(\text{F})$  and  ${}^4\text{T}_{1g}(\text{F}) \rightarrow {}^4\text{T}_{1g}(\text{P})$ , were discussed from the diffuse reflectance spectra. In the other hands, a red shifts in band gap transition could be attributed to the charge transfer transitions between the  $\text{Fe}^{3+}$   $d$ -electrons and the  $\text{SnO}_2$  conduction or valence bands. These results confirmed that  $\text{Sn}^{4+}$  was partly substituted by  $\text{Cr}^{4+}$ ,  $\text{Co}^{2+}$  and  $\text{Fe}^{3+}$ . The diffuse reflectance,  $R$  was related to the Kubelka-Munk function  $f(R)$  by the relation  $f(R) = (1-R)^2/2R$ . The band gap energies,  $E_g$  were then calculated from plotting of  $f(R)^2$  versus energy. The band gap energies were in the range of 3.2 - 3.8 eV. Optical absorption

measurements showed  $E_g$  which were decreased as increasing of the calcined temperatures. Moreover, increasing the TM concentrations reversed the trend in that the band gap was decreased gradually. However, the band gap energies of these samples were much higher than the expected 3.6 eV for bulk-pure  $\text{SnO}_2$ . This result confirmed that the  $\text{Sn}_{1-x}\text{TM}_x\text{O}_{2-\delta}$  nanoparticles have been synthesized by the autocombustion technique.

Room temperature ferromagnetism has been observed in all TM doped  $\text{SnO}_2$  powders. The hysteresis loops at the room temperature of the  $\text{Sn}_{1-x}\text{Cr}_x\text{O}_{2-\delta}$  samples showed a weak ferromagnetism. The saturation magnetization ( $M_s$ ) value of the  $\text{Sn}_{0.995}\text{Cr}_{0.005}\text{O}_{2-\delta}$  samples calcined at 873 K was about  $0.039 \mu_B/\text{Cr}$ . Thus, a magnetic moment might result in the samples doping with a non-ferromagnetic element. The coercivity ( $H_C$ ) of these samples was about 300 Oe. In addition, the well-defined hysteresis loop was observed for the  $\text{Sn}_{1-x}\text{Co}_x\text{O}_{2-\delta}$  samples. The saturation magnetization of the  $\text{Sn}_{0.995}\text{Co}_{0.005}\text{O}_{2-\delta}$  samples calcined at 973 K was  $0.11 \mu_B/\text{Co}$ . The remanence ratio and the coercive field were 0.72 and 1.3 kOe, respectively. For Fe dopant, the magnetizations of all the compounds were saturated at relatively low fields. The magnetic moment of the  $\text{Sn}_{0.995}\text{Fe}_{0.005}\text{O}_{2-\delta}$  sample calcined at 773 K was about  $0.256 \mu_B/\text{Fe}$ . The moments were decreased readily as Fe dopant increasing. The coercivity of these samples was about 200 Oe. The hysteresis loops of high Fe concentration were two types of curves. The presence of a weak ferromagnetic-like behavior with a saturated magnetization of about  $0.002 \mu_B/\text{Fe}$  was appeared in the  $\text{Sn}_{0.900}\text{Fe}_{0.100}\text{O}_{2-\delta}$  sample calcined at 773 K. A very narrow and not saturated hysteresis loops were showed in the other  $\text{Sn}_{1-x}\text{Fe}_x\text{O}_{2-\delta}$  samples,  $x > 0.100$ . These samples were superparamagnetism. The coercivity ( $H_C$ ) was about 300 Oe. The small coercivity of a polycrystalline samples indicated the intrinsically soft nature of these materials. The relatively lower magnetic moments observed in these samples was a drawback in employing them in spintronics devices.

### **Suggestion for future work**

These TM-doped SnO<sub>2</sub> nanoparticles might be characterized in the other techniques to obtain to be good diluted magnetic semiconductor (DMS) nanoparticle materials. Energy dispersive X-ray spectroscopy (EDS) and X-ray photoelectron spectroscopy (XPS) might be employed for elemental analysis. In addition, Mössbauer spectroscopy might be performed to confirm oxidation state of Fe. Moreover, magnetic property might be to obtain Curie temperature using a superconducting quantum interference device (SQUID).

## REFERENCES

## REFERENCES

1. Wolf S. A. and et al. "Spintronics: A Spin-Based Electronics Vision for the Future", **Science**. 2001; 294, 1488–1495.
2. Pearton S. J. and et al. "Advances in Wide Bandgap Materials for Semiconductor Spintronics", **Materials Science and Engineering**. 2003; R40, 137–168.
3. Cibert J., Bobo J.-F. and Lüders U. "Development of New Materials for Spintronics", **Comptes Rendus Physique**. 2005; 6, 977–996.
4. Ohno H. and et al. "(Ga,Mn)As: A New Diluted Magnetic Semiconductor Based on GaAs", **Applied Physics Letters**. 1996; 69, 363–365.
5. Matsumoto Y. and et al. "Room-Temperature Ferromagnetism in Transparent Transition Metal-Doped Titanium Dioxide", **Science**. 2001; 291, 854–856.
6. Ohno H. "Making Nonmagnetic Semiconductors Ferromagnetic", **Science**. 1998; 281, 951–956.
7. Ohno H. and et al. "Magnetotransport Properties of p-type (In,Mn)As Diluted Magnetic III-V Semiconductors", **Physical Review Letters**. 1992; 68, 2664–2667.
8. Fukumura T., Toyosaki H. and Yamada Y. "Magnetic Oxide Semiconductors", **Semiconductor Science and Technology**. 2005; 20, S103–S111.
9. Hong N. H. "Ferromagnetism in Transition-Metal-Doped Semiconducting Oxide Thin Films", **Journal of Magnetism and Magnetic Materials**. 2006; 303, 338–343.
10. Chambers S. A. and et al. "Epitaxial Growth and Properties of Ferromagnetic Co-Doped TiO<sub>2</sub> Anatase", **Applied Physics Letters**. 2001; 79, 3467–3469.
11. Chambers S. A. and et al. "Clusters and Magnetism in Epitaxial Co-Doped TiO<sub>2</sub> Anatase", **Applied Physics Letters**. 2003; 82, 1257–1259.
12. Stampe P. A. and et al. "Investigation of the Cobalt Distribution in TiO<sub>2</sub>:Co Thin Films", **Journal of Applied Physics**. 2002; 92, 7114–7121.
13. Kennedy R. and et al. "Hopping Transport in TiO<sub>2</sub>:Co: A Signature of Multiphase Behavior", **Applied Physics Letters**. 2004; 84, 2832–2834.
14. Stampe P. A. and et al. "Investigation of the Cobalt Distribution in the Room Temperature Ferromagnet TiO<sub>2</sub>:Co", **Journal of Applied Physics**. 2003; 93, 7864–7866.

## REFERENCES (CONTINUED)

15. Hong N. H. and et al. "Substrate Effects on the Room-Temperature Ferromagnetism in Co-Doped TiO<sub>2</sub> Thin Films Grown by Pulsed Laser Deposition", **Journal of Applied Physics**. 2004; 95, 7378–7380.
16. Park M. S., Kwon S. K. and Min B. I. "Electronic Structures of Doped Anatase TiO<sub>2</sub>: Ti<sub>1-x</sub>M<sub>x</sub>O<sub>2</sub> (M = Co, Mn, Fe, Ni)", **Physical Reviews B**. 2002; 65, 161201/1–4.
17. Fukumura T. , and et al. "Exploration of Oxide-based Diluted Magnetic Semiconductors toward Transparent Spintronics", **Applied Surface Science**. 2004; 223, 62–67.
18. Janisch R., Gopal P. and Spaldin N. A. "Transition Metal-doped TiO<sub>2</sub> and ZnO–Present Status of the Field", **Journal of Physics: Condensed Matter**. 2005; 17, R657–R689.
19. Shinde S. R. and et al. "Ferromagnetism in Laser Deposited Anatase Ti<sub>1-x</sub>Co<sub>x</sub>O<sub>2-δ</sub> Films", **Physical Review B**. 2003; 67, 115211/1–6.
20. Chambers S.A. and et al. "Epitaxial Growth and Properties of MBE-Grown Ferromagnetic Co-doped TiO<sub>2</sub> Anatase Films on SrTiO<sub>3</sub> (001) and LaAlO<sub>3</sub> (001)", **Thin Solid Films**. 2002; 418, 197–210.
21. Hong N. H. and et al. "Room Temperature Ferromagnetism in Anatase Ti<sub>0.95</sub>V<sub>0.05</sub>O<sub>2</sub> Thin Films", **Physica B**. 2005; 355, 295–298.
22. Seong N.-J., Yoon S.-G. and Cho C.-R. "Effects of Co-doping Level on the Microstructural and Ferromagnetic Properties of Liquid-Delivery Metalorganic-Chemical-Vapor-Deposited Ti<sub>1-x</sub>Co<sub>x</sub>O<sub>2</sub> Thin Films", **Applied Physics Letters**. 2002; 81, 4209–4211.
23. Kim H. and et al. "Formation of Co Nanoclusters in Epitaxial Ti<sub>0.96</sub>Co<sub>0.04</sub>O<sub>2</sub> Thin Films and their Ferromagnetism", **Applied Physics Letters**. 2002; 82, 2421–2423.
24. Kim J.-Y. and et al. "Ferromagnetism Induced by Clustered Co in Co-Doped Anatase TiO<sub>2</sub> Thin Films", **Physical Review Letters**. 2003; 90, 017401/1–4.
25. Bryan J. D. and et al. "Strong Room-Temperature Ferromagnetism in Co<sup>2+</sup>-Doped TiO<sub>2</sub> Made from Colloidal Nanocrystals", **Journal of the American Chemical Society**. 2004; 126, 11640–11647.
26. Jeong B.-S. and et al. "Properties of Anatase Co<sub>x</sub>Ti<sub>1-x</sub>O<sub>2</sub> Thin Films Epitaxially Grown by Reactive Sputtering", **Thin Solid Films**. 2005; 488, 194–199.

## REFERENCES (CONTINUED)

27. Han G. C. and et al. "Epitaxial Growth of Ferromagnetic Co:TiO<sub>2</sub> Thin Films by Co-sputtering", **Journal of Magnetism and Magnetic Materials**. 2004; 268, 159–164.
28. Park W. K. and et al. "Semiconducting and Ferromagnetic Behavior of Sputtered Co-doped TiO<sub>2</sub> Thin Films above Room Temperature", **Journal of Applied Physics**. 2002; 91, 8093–8095.
29. Osterwalder J. and et al. "Growth of Cr-doped TiO<sub>2</sub> Films in the Rutile and Anatase Structures by Oxygen Plasma Assisted Molecular Beam Epitaxy", **Thin Solid Films**. 2005; 484, 289–298.
30. Shutthanandan V. and et al. "Synthesis of Room-Temperature Ferromagnetic Cr-doped TiO<sub>2</sub>(110) Rutile Single Crystals using Ion Implantation", **Nuclear Instruments and Methods in Physics Research B**. 2006; 242, 198–200.
31. Hong N. H., Sakai J. and Prellier W. "Distribution of Dopant in Fe:TiO<sub>2</sub> and Ni:TiO<sub>2</sub> Thin Films", **Journal of Magnetism and Magnetic Materials**. 2004; 281, 347–352.
32. Fukumura T. and et al. "An Oxide-diluted Magnetic Semiconductor: Mn-doped ZnO", **Applied Physics Letters**. 1999; 75, 3366–3368.
33. Ueda K., Tabata H. and Kawai T. "Magnetic and Electric Properties of Transition-Metal-doped ZnO Films", **Applied Physics Letters**. 2001; 79, 988–990.
34. Jin Z. and et al. "High Throughput Fabrication of Transition-Metal-doped Epitaxial ZnO Thin Films: A Series of Oxide-Diluted Magnetic Semiconductors and their Properties", **Applied Physics Letters**. 2001; 78, 3824–3826.
35. Fukumura T. and et al. "Magnetic Properties of Mn-doped ZnO", **Applied Physics Letters**. 2001; 78, 958–960.
36. Kim J.-H. and et al. "Magnetic Properties of Epitaxially Grown Semiconducting Zn<sub>1-x</sub>Co<sub>x</sub>O Thin Films by Pulsed Laser Deposition", **Journal of Applied Physics**. 2002; 92, 6066–6071.
37. Paul Joseph D. and et al. "Synthesis of Zn<sub>0.95</sub>Cr<sub>0.05</sub>O DMS by co-precipitation and Ceramic Methods: Structural and Magnetization Studies", **Materials Chemistry and Physics**. 2006; 97, 188–192.



## REFERENCES (CONTINUED)

38. Tiwari A. and et al. "Structural, Optical and Magnetic Properties of Dilute Magnetic Semiconducting  $\text{Zn}_{1-x}\text{Mn}_x\text{O}$  Films", **Solid State Communications**. 2002; 121, 371-374.
39. Theodoropoulou N.A. and et al. "Ferromagnetism in Co- and Mn-doped ZnO", **Solid-State Electronics**. 2003; 47, 2231-2235.
40. Wakano T. and et al. "Magnetic and Magneto-transport Properties of ZnO:Ni Films", **Physica E**. 2001; 10, 260-264.
41. Saeki H., Tabata H. and Kawai T. "Magnetic and Electric Properties of Vanadium -doped ZnO Films", **Solid State Communications**. 2001; 120, 439-443.
42. Cho Y. M. and et al. "Effects of Rapid Thermal Annealing on the Ferromagnetic Properties of Sputtered  $\text{Zn}_{1-x}(\text{Co}_{0.5}\text{Fe}_{0.5})_x\text{O}$  Thin Films", **Applied Physics Letters**. 2002; 80, 3358-3360.
43. Lee H.-J. and et al. "Study of Diluted Magnetic Semiconductor: Co-doped ZnO", **Applied Physics Letters**. 2002; 81, 4020-4022.
44. Jung S. W. and et al. "Ferromagnetic Properties of  $\text{Zn}_{1-x}\text{Mn}_x\text{O}$  Epitaxial Thin Films", **Applied Physics Letters**. 2002; 80, 4561-4563.
45. Han S.-J. and et al. "A key to Room-Temperature Ferromagnetism in Fe-doped ZnO: Cu", **Applied Physics Letters**. 2002; 81, 4212-4214.
46. Kim J. H. and et al. "The Origin of Room Temperature Ferromagnetism in Cobalt-doped Zinc Oxide Thin Films Fabricated by PLD", **Journal of the European Ceramic Society**. 2004; 24, 1847-1851.
47. Pei G. and et al. "Synthesis and Magnetic Properties of Ni-doped Zinc Oxide Powders", **Journal of Magnetism and Magnetic Materials**. 2006; 302, 340-342.
48. Jeon K. A. and et al. "Magnetic and Optical Properties of  $\text{Zn}_{1-x}\text{Mn}_x\text{O}$  Thin Films Prepared by Pulsed Laser Deposition", **Journal of Crystal Growth**. 2006; 287, 66-69.
49. Alaria J. and et al. "No Ferromagnetism in Mn- doped ZnO Semiconductors", **Chemical Physics Letters**. 2005; 415, 337-341.

## REFERENCES (CONTINUED)

50. Kimura H. and et al. "Rutile-type Oxide-diluted Magnetic Semiconductor: Mn-doped  $\text{SnO}_2$ ", **Applied Physics Letters**. 2002; 80, 94-96.
51. Ogale S. B. and et al. "High Temperature Ferromagnetism with a Giant Magnetic Moment in Transparent Co-doped  $\text{SnO}_{2.8}$ ", **Physical Review Letters**. 2003; 91, 077205/1-4.
52. Punnoose A. and et al. "Room-temperature Ferromagnetism in Chemically Synthesized  $\text{Sn}_{1-x}\text{Co}_x\text{O}_2$  Powders", **Applied Physics Letters**. 2004; 85, 1559-1561.
53. Punnoose A. and Hays J. "Possible Metamagnetic Origin of Ferromagnetism in Transition metal-doped  $\text{SnO}_2$ ", **Journal of Applied Physics**. 2005; 97, 10D321/1-3.
54. Hays J. and et al. "Relationship between the Structural and Magnetic Properties of Co-doped  $\text{SnO}_2$  Nanoparticles", **Physical Review B**. 2005; 72, 075203/1-7.
55. Coey J. M. D. and et al. "Ferromagnetism in Fe-doped  $\text{SnO}_2$  Thin Films", **Applied Physics Letters**. 2004; 84, 1332-1334.
56. Punnoose A. and et al. "Development of High-temperature Ferromagnetism in  $\text{SnO}_2$  and Paramagnetism in  $\text{SnO}$  by Fe Doping", **Physical Review B**. 2005; 72, 054402/1-14.
57. Hong N. H. and et al. "Transparent Cr-doped  $\text{SnO}_2$  Thin Films: Ferromagnetism beyond Room Temperature with a Giant Magnetic Moment", **Journal of Physics: Condensed Matter**. 2005; 17, 1697-1702.
58. Hong N. H. and Sakai J. "Ferromagnetic V-doped  $\text{SnO}_2$  Thin Films", **Physica B**. 2005; 358, 265-268.
59. Hong N. H. and et al. "Magnetism in Ni-doped  $\text{SnO}_2$  Thin Films", **Journal of Physics: Condensed Matter**. 2005; 17, 6533-6538.
60. Fitzgerald C. B. and et al. " $\text{SnO}_2$  Doped with Mn, Fe or Co: Room Temperature Dilute Magnetic Semiconductors", **Journal of Applied Physics**. 2004; 95, 7390-7392.
61. Wang W. and et al. "Structure and Magnetic Properties of Cr/Fe-doped  $\text{SnO}_2$  Thin Films", **Journal of Applied Physics**. 2006; 99, 08M115/1-3.
62. Gopinadhan K. and et al. "Cobalt-Substituted  $\text{SnO}_2$  Thin Films: A Transparent Ferromagnetic Semiconductor", **Journal of Applied Physics**. 2006; 99, 126106/1-3.

## REFERENCES (CONTINUED)

63. Lee S. -Y. and Park B. -O. "Structural, Electrical and Optical Characteristics of SnO<sub>2</sub>: Sb Thin Films by Ultrasonic Spray Pyrolysis", **Thin Solid Films**. 2006; 510, 154-158.
64. Yang H. and et al. "Synthesis of Vanadium-doped SnO<sub>2</sub> Nanoparticles by Chemical co-precipitation Method", **Materials Letters**. 2003; 57, 3124-3127.
65. Rani S. and et al. "Structure, Microstructure and Photoluminescence Properties of Fe doped SnO<sub>2</sub> Thin Films", **Solid State Communications**. 2007; 141, 214-218.
66. Zhang J. and Gao L. "Synthesis and Characterization of Antimony-doped Tin Oxide (ATO) Nanoparticles by a New Hydrothermal Method", **Materials Chemistry and Physics**. 2004; 87, 10-13.
67. Wang C. and et al. "A novel Method to Prepare Nanocrystalline SnO<sub>2</sub>", **Nanostructured Materials**. 1996; 7, 421-425.
68. Patil K. C., Aruna S. T. and Mimani T. "Combustion Synthesis: an Update", **Current Opinion in Solid State and Materials Science**. 2002; 6, 507-512.
69. de Sousa V. C., Morelli M. R. and Kiminami R. H. G. "Combustion Process in the Synthesis of ZnO-Bi<sub>2</sub>O<sub>3</sub>", **Ceramics International**. 2000; 26, 561-564.
70. Fraigi L., Lamas D. G. and Walsoe de R. N. E. "Novel Method to Prepare Nanocrystalline SnO<sub>2</sub> Powders by a Gel-combustion Process", **Nanostructured Materials**. 1999; 11, 311-318.
71. Zhang J. and Gao L. "Antimony-doped Tin Oxide Nanocrystallites Prepared by a Combustion Process", **Materials Letters**. 2004; 58, 2730-2734.
72. Fraigi L., Lamas D. G. and Walsoe de R. N. E. "Comparison Between two Combustion Routes for the Synthesis of Nanocrystalline SnO<sub>2</sub> Powders", **Materials Letters**. 2001; 47, 262-266.
73. Rietveld H. M. "A Profile Refinement Method for Nuclear and Magnetic Structures", **Journal of Crystallography**. 1969; 2, 65-71.
74. McCusker L. B. and et al. "Rietveld Refinement Guidelines", **Journal of Crystallography**. 1999; 32, 36-50.

## REFERENCES (CONTINUED)

75. Rodríguez-Carvajal J. "Recent advances in Magnetic Structure Determination by Neutron Powder Diffraction", **Physica B: Condensed Matter**. 1993; 192, 55-69.
76. Finger L. W., Cox D. E. and Jephcoat A. P. "A Correction for Powder Diffraction Peak Asymmetry Due to Axial Divergence", **Journal of Crystallography**. 1994; 27, 892-900.
77. Young R. A. **The Rietveld Method**. International Union of Crystallography, Oxford University Press, 1993 and reference therein.
78. Larson A. C. and Von Dreele R. B. "General Structure Analysis System (GSAS)", Los Alamos National Laboratory Report LAUR. 1994, 86-748.
79. Toby B. H. "EXPGUI, a Graphical User Interface for GSAS", **Journal of Crystallography**. 2001; 34, 210-213.
80. Wiles, D. B., Young, R. A. "A New Computer Program for Rietveld Analysis of X-ray Powder Diffraction Patterns", **Journal of Crystallography**. 1981; 14, 149-151.
81. Young R. A. and et al. "DBWS-9411 - an Upgrade of the DBWS\*. Programs for Rietveld Refinement with PC and Mainframe Computers", **Journal of Crystallography**. 1995; 28, 366-367.
82. Izumi F. and et al. "Rietveld Analysis of Powder Patterns Obtained by TOF Neutron Diffraction Using Cold Neutron Sources", **Journal of Crystallography**. 1987; 20, 411-418.
83. Scherrer P. "Bestimmung der Größe und der inneren Struktur von Kolloidteilchen mittels Röntgenstrahlung", **Gottinger Nachrichten**. 1918; 2, 98-100.
84. Langford J. I. and Wilson A. J. C. "Scherrer after Sixty Years: A Survey and Some New Results in the Determination of Crystallite size", **Journal of Crystallography**. 1978; 11, 102-113.
85. Williamson G. K. and Hall W. H. "X-ray Line Broadening from Filled Aluminium and Wolfram", **Acta Metallurgy**. 1953; 1, 22-31.

## REFERENCES (CONTINUED)

86. Wertheim G. K. and et al. "Determination of the Gaussian and Lorentzian Content of Experimental Line Shapes", **Review of Scientific Instruments**. 1974; 45, 1369-1371.
87. Suryanarayana C. and Grant Norton M. **X-ray Diffraction: A Practical Approach**. New York: Plenum Press. 1998.
88. Shannon R. D. "Revised Effective Ionic Radii and Systematic Studies of Interatomic Distances in Halides and Chalcogenides", **Acta Crystallographica**. 1976; A32, 751-767.
89. Ren F. and et al. "Chromium-based Ceramic Colors", **Ceramic Bullatin**. 1992; 71, 759-764.
90. Tena M.A. and et al. "Study of Cr-SnO<sub>2</sub> Ceramic Pigment and of Ti/Sn Ratio on Formation and Coloration of These Materials", **Journal of the European Ceramic Society**. 2007; 27, 215-221.
91. Kittel C. **Introduction to Solid State Physics**. 7<sup>th</sup> edition. New York: Wiley, 1996.
92. Bouaine A. and et al. "Structural, Optical, and Magnetic Properties of Co-doped SnO<sub>2</sub> Powders Synthesized by the Coprecipitation Technique", **Journal of Physical Chemistry C**. 2007; 111, 2924-2928.
93. Yan L., Pan J. S. And Ong C. K. "XPS Studies of Room Temperature Magnetic Co-doped SnO<sub>2</sub> Deposited on Si", **Materials Science and Engineering B**. 2006; 128, 34-36.
94. Bucher J. P., Douglass D. C., and Bloomfield L. A. "Magnetic Properties of Free Cobalt Clusters", **Physical Review Letters**. 1991; 66, 3052-3055.
95. Fang L. M. and et al. "Synthesis and Characteristics of Fe<sup>3+</sup>-doped SnO<sub>2</sub> nanoparticles via sol-gel-calcination or sol-gel-hydrothermal route", **Journal of Alloys and Compounds**. 2008; 454, 261-267.
96. Mathew X. and et al. "Effect of Annealing Conditions on the Fe Incorporation and Ferromagnetism of Sn<sub>1-x</sub>Fe<sub>x</sub>O<sub>2</sub>: A Raman Spectroscopic Investigation", **Journal of Applied Physics**. 2006; 99, 08M101/1-3.

## REFERENCES (CONTINUED)

97. Fitzgerald C. B. and et al. "Magnetism in Diluted Magnetic Oxide Thin Films Based on  $\text{SnO}_2$ ", **Physical Review B**. 2006; 74, 115307/1–10.
98. Hong N. H. and et al. "Role of Defects in Tuning Ferromagnetism in Diluted Magnetic Oxide Thin Films", **Physical Review B**. 2005; 72, 045336/1–5.
99. Sakuma J. and et al. "Mossbauer Studies and Magnetic Properties of  $\text{SnO}_2$  Doped with  $^{57}\text{Fe}$ ", **Thin Solid Films**. 2007; 515, 8653–8655.

## **APPENDICES**

**APPENDIX A**  
**X-ray Diffraction patterns**



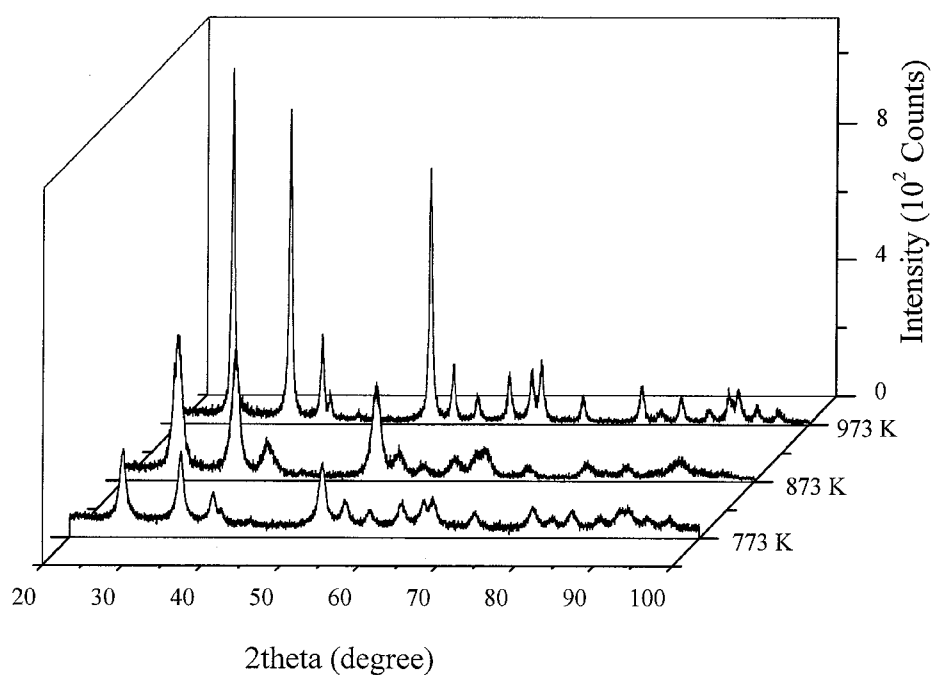


**Figure A.1** X-ray Diffraction patterns of  $\text{Sn}_{0.990}\text{Cr}_{0.010}\text{O}_{2.8}$  calcined at 773, 873 and 973 K.

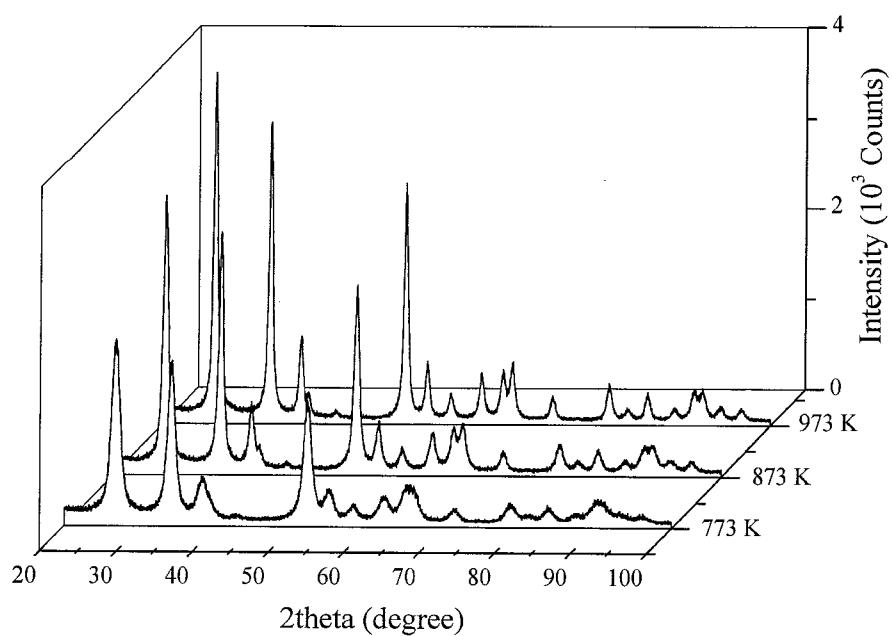


**Figure A.2** X-ray Diffraction patterns of  $\text{Sn}_{0.990}\text{Co}_{0.010}\text{O}_{2.8}$  calcined at 773, 873 and 973 K.

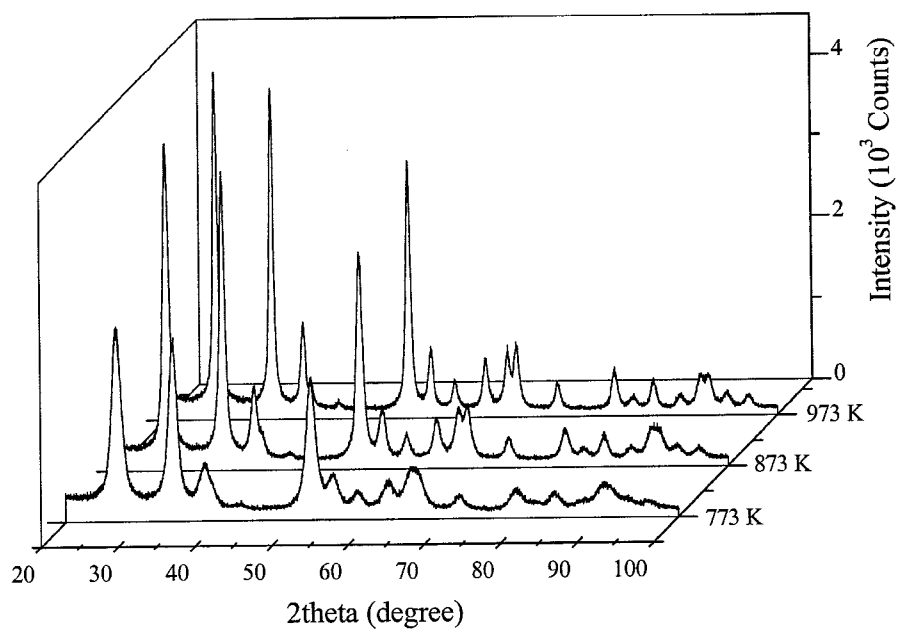


**Figure A.3** X-ray Diffraction patterns of  $\text{Sn}_{0.990}\text{Fe}_{0.010}\text{O}_{2.8}$  calcined at 773, 873 and 973 K.

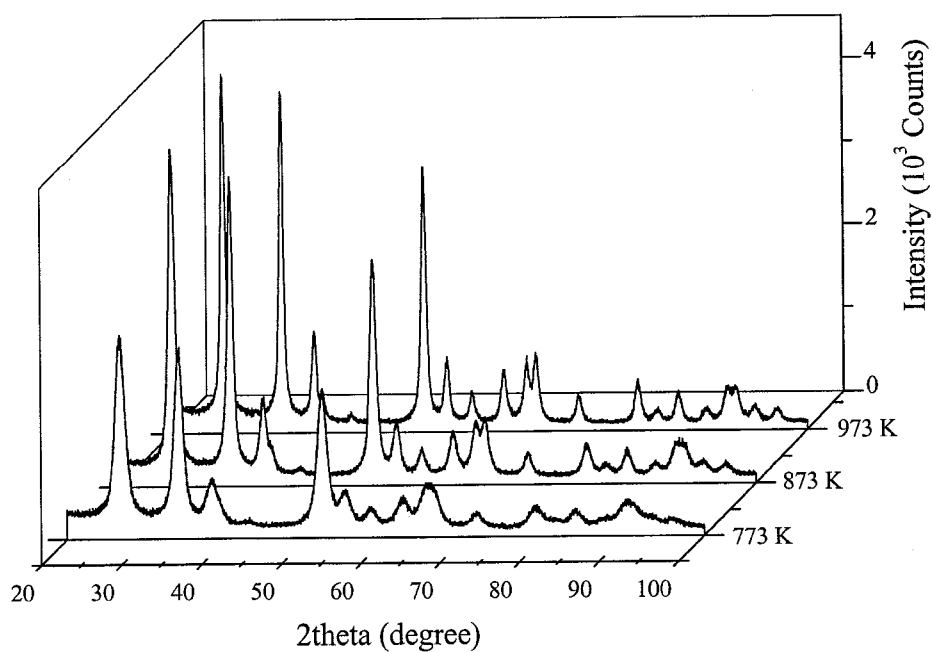


**Figure A.4** X-ray Diffraction patterns of  $\text{Sn}_{0.900}\text{Fe}_{0.100}\text{O}_{2.8}$  calcined at 773, 873 and 973 K.

**APPENDIX B**  
**Atomic Scattering Factors**

**Table B.1** Atomic scattering factors of some element [87].

| $\frac{\sin \theta}{\lambda} (\text{\AA}^{-1})$ | 0.0 | 0.1  | 0.2  | 0.3  | 0.4  | 0.5  | ... |
|---|-----|------|------|------|------|------|-----|
| Cr  | 24  | 21.1 | 17.4 | 14.2 | 12.1 | 10.6 | ... |
| Mn  | 25  | 22.1 | 18.2 | 14.9 | 12.7 | 11.1 | ... |
| Fe  | 26  | 23.1 | 18.9 | 15.6 | 13.3 | 11.6 | ... |
| Co  | 27  | 24.1 | 19.8 | 16.4 | 14.0 | 12.1 | ... |
| Sn  | 50  | 45.7 | 39.5 | 33.8 | 28.7 | 25.6 | ... |
| O   | 8   | 7.1  | 5.3  | 3.9  | 2.9  | 2.2  | ... |
| O <sup>2-</sup>                                 | 10  | 8.0  | 5.5  | 3.8  | 2.7  | 2.1  | ... |

**APPENDIX C**  
**The Database of Some Ionic Radii**

**Table C.1** The database of some ionic radii [88].

| Ion | Charge | Coordination | Spin State | Ionic Radius (Å) |
|-----|--------|--------------|------------|------------------|
| O   | -2     | II           |            | 1.35             |
| Sn  | 4      | IV           |            | 0.55             |
|     |        | VI           |            | 0.69*            |
| Cr  | 2      | VI           | High Spin  | 0.8*             |
|     |        |              | Low Spin   | 0.73             |
|     | 3      | VI           |            | 0.615*           |
|     |        |              |            |                  |
|     |        | IV           |            | 0.41             |
|     |        |              |            | 0.55             |
| Fe  | 2      | VI           | Low Spin   | 0.61             |
|     |        |              | High Spin  | 0.78*            |
|     |        | VIII         |            | 0.92             |
|     |        |              |            |                  |
|     | 3      | VI           | Low Spin   | 0.55             |
|     |        |              | High Spin  | 0.645*           |
|     |        | VIII         | High Spin  | 0.78             |
|     |        |              |            |                  |
| Co  | 2      | VI           | High Spin  | 0.745*           |
|     |        |              | Low Spin   | 0.65             |
|     | 3      | VI           | Low Spin   | 0.545*           |
|     |        |              | High Spin  | 0.61             |
|     | 4      | IV           |            | 0.4              |
|     |        | VI           |            | 0.53             |

**Note:** (\*) = Most Reliable.

## APPENDIX D

**The Crystallite Sizes Calculations for  $\text{Sn}_{0.700}\text{Fe}_{0.300}\text{O}_{2.8}$  calcined at 973 K**

**Table D.1**  $\beta_i$  of commercial  $\text{SnO}_2$  which calcined at 1,273 K for 3 hrs.

| Material: Commercial $\text{SnO}_2$ |            | Radiation: $\text{CuK}\alpha$ , $\lambda = 0.15418$ nm |                        |
|-------------------------------------|------------|--|------------------------|
| 2 theta (degree)                    | <i>hkl</i> | FWHM (degree)  | FWHM (rad) = $\beta_i$ |
| 26.5866                             | 110        | 0.2214   | $3.86 \times 10^{-3}$  |
| 33.8632                             | 101        | 0.2155   | $3.76 \times 10^{-3}$  |
| 37.9406                             | 200        | 0.1938   | $3.38 \times 10^{-3}$  |
| 51.8138                             | 211        | 0.1876   | $3.27 \times 10^{-3}$  |
| 54.8148                             | 220        | 0.1776   | $3.10 \times 10^{-3}$  |

**Table D.2** Crystallite size calculation by Scherrer's Equation.

| Material: $\text{Sn}_{0.70}\text{Fe}_{0.30}\text{O}_{2.8}$ |            |                     |                       | Radiation: $\text{CuK}\alpha$ , $\lambda = 0.15418$ nm               |                       |                                 |
|--|------------|---------------------|-----------------------|--|-----------------------|---------------------------------|
| $2\theta(^{\circ})$  | <i>hkl</i> | $\beta_o(^{\circ})$ | $\beta_o(\text{rad})$ | $\beta_r = \sqrt{(\beta_o - \beta_i)\sqrt{(\beta_o^2 - \beta_i^2)}}$ | $\beta_r \cos\theta$  | $\langle D \rangle (\text{nm})$ |
| 26.61  | 110        | 1.32                | $2.31 \times 10^{-2}$ | $2.10 \times 10^{-2}$  | $2.04 \times 10^{-2}$ | 6.82                            |
| 33.94  | 101        | 1.17                | $2.04 \times 10^{-2}$ | $1.82 \times 10^{-2}$  | $1.75 \times 10^{-2}$ | 7.95                            |
| 38.04  | 200        | 1.33                | $2.32 \times 10^{-2}$ | $2.13 \times 10^{-2}$  | $2.01 \times 10^{-2}$ | 6.89                            |
| 51.91  | 211        | 1.40                | $2.44 \times 10^{-2}$ | $2.26 \times 10^{-2}$  | $2.03 \times 10^{-2}$ | 6.82                            |
| 54.85  | 220        | 1.39                | $2.42 \times 10^{-2}$ | $2.25 \times 10^{-2}$  | $2.00 \times 10^{-2}$ | 6.95                            |
|  |            |                     |                       |  |                       | $7.09 \pm 0.44$                 |

**Table D.3** Crystallite size calculation by Williamson-Hall Plot method.

| Material: $\text{Sn}_{0.70}\text{Fe}_{0.30}\text{O}_{2.8}$ |            |                     |                       | Radiation: $\text{CuK}\alpha$ , $\lambda = 0.15418$ nm               |                       |               |
|--|------------|---------------------|-----------------------|--|-----------------------|---------------|
| $2\theta(^{\circ})$  | <i>hkl</i> | $\beta_o(^{\circ})$ | $\beta_o(\text{rad})$ | $\beta_r = \sqrt{(\beta_o - \beta_i)\sqrt{(\beta_o^2 - \beta_i^2)}}$ | $\beta_r \cos\theta$  | $4\sin\theta$ |
| 26.61  | 110        | 1.32                | $2.31 \times 10^{-2}$ | $2.10 \times 10^{-2}$  | $2.04 \times 10^{-2}$ | 0.92          |
| 33.94  | 101        | 1.17                | $2.04 \times 10^{-2}$ | $1.82 \times 10^{-2}$  | $1.75 \times 10^{-2}$ | 1.17          |
| 38.04  | 200        | 1.33                | $2.32 \times 10^{-2}$ | $2.13 \times 10^{-2}$  | $2.01 \times 10^{-2}$ | 1.30          |
| 51.91  | 211        | 1.40                | $2.44 \times 10^{-2}$ | $2.26 \times 10^{-2}$  | $2.03 \times 10^{-2}$ | 1.75          |
| 54.85  | 220        | 1.39                | $2.42 \times 10^{-2}$ | $2.25 \times 10^{-2}$  | $2.00 \times 10^{-2}$ | 1.84          |

Plot  $\beta_r \cos\theta$  versus  $4\sin\theta$



## **APPENDIX E**

**Crystallite sizes calculated by Scherrer's equation  
and Williamson–Hall Plot method**

**Table E.1** Crystallite sizes,  $D$  (nm) of the  $\text{Sn}_{1-x}\text{Cr}_x\text{O}_{2.8}$  samples

| x     | Scherrer's equation |                  |                  | WHP method       |                  |                  |
|-------|---------------------|------------------|------------------|------------------|------------------|------------------|
|       | 773 K               | 873 K            | 973 K            | 773 K            | 873 K            | 973 K            |
| 0.000 | $10.31 \pm 0.56$    | $12.39 \pm 0.63$ | $14.48 \pm 0.69$ | $12.58 \pm 0.46$ | $16.04 \pm 0.18$ | $18.27 \pm 0.29$ |
| 0.005 | $6.96 \pm 0.73$     | $12.19 \pm 0.45$ | $15.76 \pm 0.20$ | $5.71 \pm 0.99$  | $12.20 \pm 0.71$ | $20.05 \pm 0.43$ |
| 0.010 | $6.67 \pm 0.77$     | $10.55 \pm 0.58$ | $13.22 \pm 0.82$ | $6.31 \pm 0.86$  | $13.22 \pm 0.43$ | $19.97 \pm 0.24$ |
| 0.015 | $6.73 \pm 0.67$     | $10.32 \pm 0.59$ | $12.98 \pm 0.67$ | $8.21 \pm 0.34$  | $13.22 \pm 0.26$ | $19.20 \pm 0.18$ |

**Table E.2** Crystallite sizes,  $D$  (nm) of the  $\text{Sn}_{1-x}\text{Co}_x\text{O}_{2.8}$  samples

| x     | Scherrer's equation |                  |                  | WHP method       |                  |                  |
|-------|---------------------|------------------|------------------|------------------|------------------|------------------|
|       | 773 K               | 873 K            | 973 K            | 773 K            | 873 K            | 973 K            |
| 0.000 | $10.31 \pm 0.56$    | $12.39 \pm 0.63$ | $14.48 \pm 0.69$ | $12.58 \pm 0.46$ | $16.04 \pm 0.18$ | $18.27 \pm 0.29$ |
| 0.005 | $5.99 \pm 0.33$     | $10.27 \pm 0.37$ | $12.62 \pm 0.55$ | $5.17 \pm 0.35$  | $10.46 \pm 0.56$ | $16.09 \pm 0.90$ |
| 0.010 | $5.72 \pm 0.41$     | $9.03 \pm 0.34$  | $11.69 \pm 0.37$ | $5.56 \pm 0.29$  | $11.08 \pm 0.43$ | $15.32 \pm 0.84$ |
| 0.015 | $5.68 \pm 0.36$     | $8.73 \pm 0.42$  | $11.22 \pm 0.43$ | $5.82 \pm 0.59$  | $10.18 \pm 0.61$ | $14.43 \pm 0.85$ |

**Table E.3** Crystallite sizes,  $D$  (nm) of the  $\text{Sn}_{1-x}\text{Fe}_x\text{O}_{2.8}$ 

| x     | Scherrer's equation |                  |                  | WHP method       |                  |                  |
|-------|---------------------|------------------|------------------|------------------|------------------|------------------|
|       | 773 K               | 873 K            | 973 K            | 773 K            | 873 K            | 973 K            |
| 0.000 | $10.31 \pm 0.56$    | $12.39 \pm 0.63$ | $14.48 \pm 0.69$ | $12.58 \pm 0.46$ | $16.04 \pm 0.18$ | $18.27 \pm 0.29$ |
| 0.005 | $5.83 \pm 0.60$     | $11.18 \pm 0.47$ | $15.05 \pm 0.96$ | $6.71 \pm 0.86$  | $14.40 \pm 0.08$ | $20.70 \pm 0.17$ |
| 0.010 | $5.86 \pm 0.57$     | $11.55 \pm 0.40$ | $15.47 \pm 0.83$ | $6.57 \pm 0.94$  | $14.32 \pm 0.14$ | $20.89 \pm 0.10$ |
| 0.015 | $5.39 \pm 0.52$     | $10.11 \pm 0.48$ | $14.96 \pm 0.42$ | $5.51 \pm 0.74$  | $12.30 \pm 0.39$ | $18.05 \pm 0.20$ |
| 0.100 | $5.22 \pm 0.32$     | $8.00 \pm 0.42$  | $10.95 \pm 0.55$ | $5.88 \pm 0.91$  | $9.41 \pm 0.64$  | $13.41 \pm 0.41$ |
| 0.150 | $5.14 \pm 0.30$     | $7.47 \pm 0.39$  | $9.78 \pm 0.55$  | $5.81 \pm 0.88$  | $8.53 \pm 0.81$  | $11.76 \pm 0.55$ |
| 0.200 | $4.84 \pm 0.34$     | $6.19 \pm 0.47$  | $7.94 \pm 0.33$  | $5.27 \pm 0.93$  | $7.67 \pm 0.28$  | $9.06 \pm 0.79$  |
| 0.250 | $4.85 \pm 0.38$     | $5.84 \pm 0.44$  | $7.30 \pm 0.36$  | $5.29 \pm 0.95$  | $6.98 \pm 0.66$  | $8.49 \pm 0.67$  |
| 0.300 | $4.41 \pm 0.39$     | $5.38 \pm 0.39$  | $7.09 \pm 0.44$  | $4.59 \pm 0.77$  | $6.13 \pm 0.86$  | $8.34 \pm 0.67$  |

**APPENDIX F**  
**Kubelka-Munk Spectra**

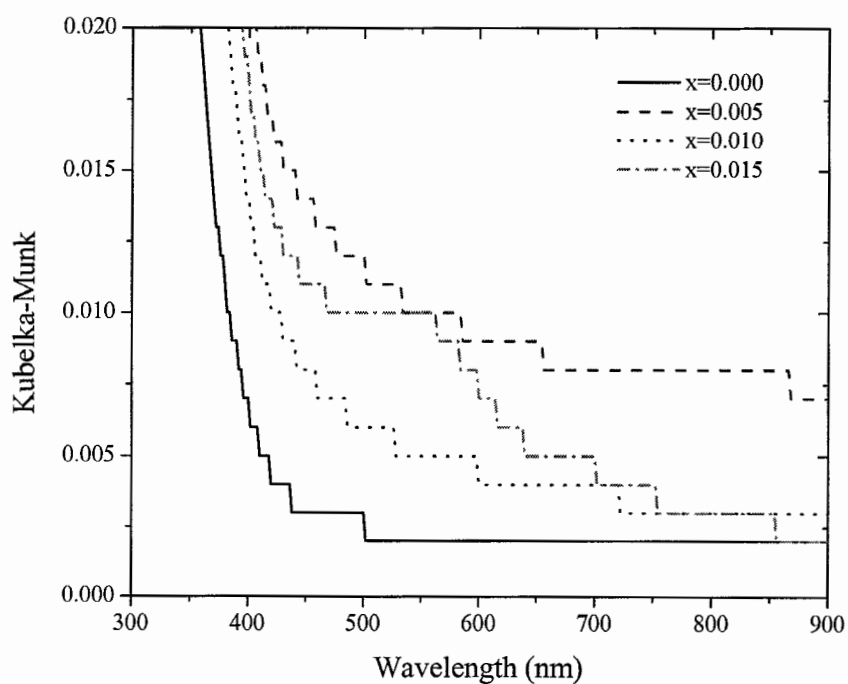


**Figure F.1** The Kubelka-Munk spectra of the  $\text{Sn}_{1-x}\text{Cr}_x\text{O}_{2.8}$  ( $x \leq 0.015$ ) samples calcined at 773 K.

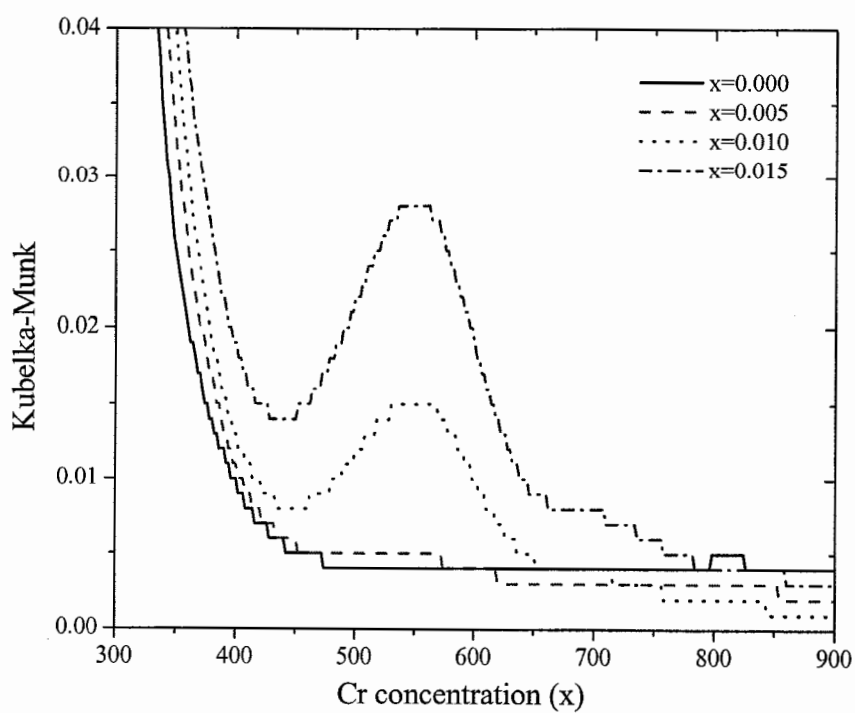


**Figure F.2** The Kubelka-Munk spectra of the  $\text{Sn}_{1-x}\text{Cr}_x\text{O}_{2.8}$  ( $x \leq 0.015$ ) samples calcined at 873 K.

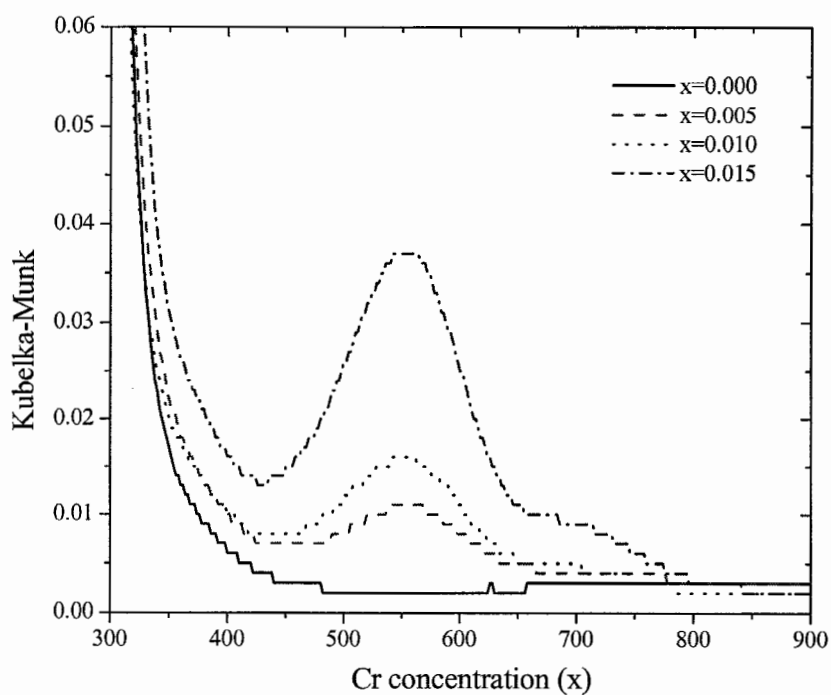


**Figure F.3** The Kubelka-Munk spectra of the  $\text{Sn}_{1-x}\text{Cr}_x\text{O}_{2.8}$  ( $x \leq 0.015$ ) samples calcined at 973 K.

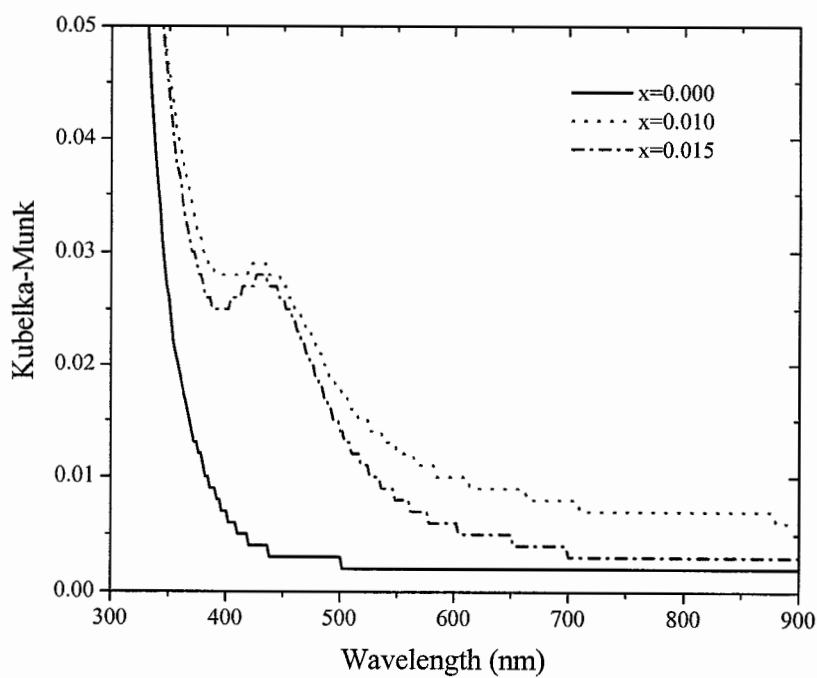


**Figure F.4** The Kubelka-Munk spectra of the  $\text{Sn}_{1-x}\text{Co}_x\text{O}_{2.8}$  ( $x \leq 0.015$ ) samples calcined at 773 K.

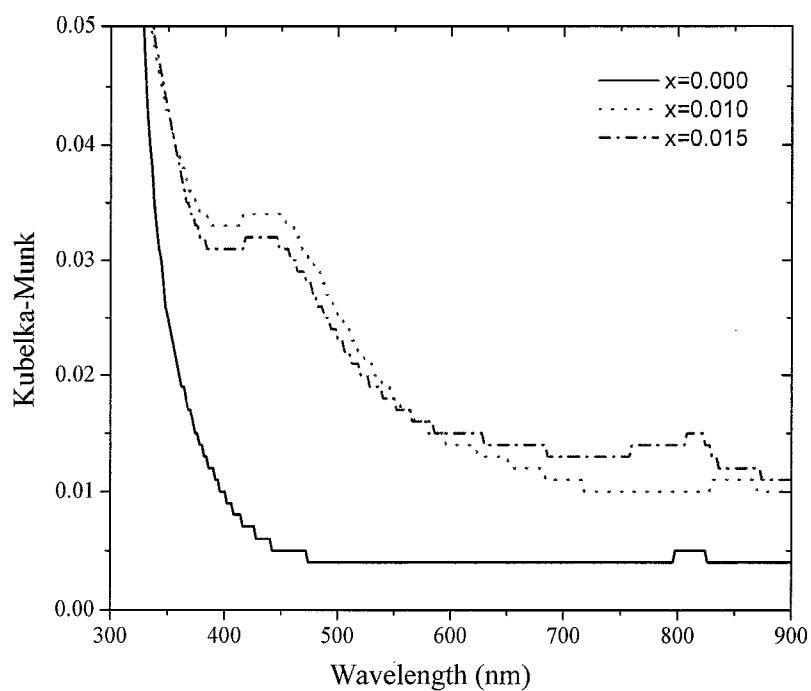


**Figure F.5** The Kubelka-Munk spectra of the  $\text{Sn}_{1-x}\text{Co}_x\text{O}_{2-\delta}$  ( $x \leq 0.015$ ) samples calcined at 873 K.

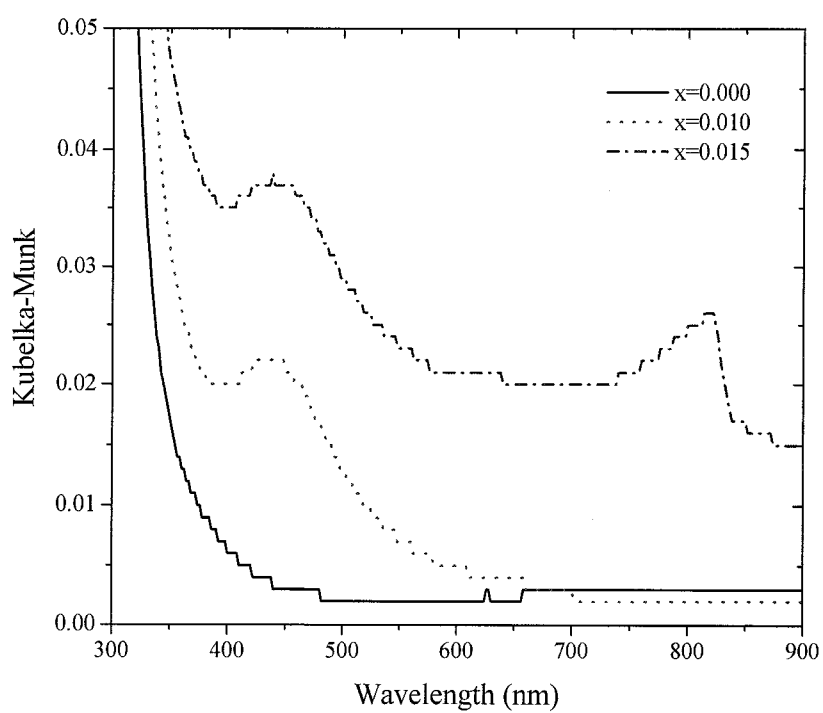


**Figure F.6** The Kubelka-Munk spectra of the  $\text{Sn}_{1-x}\text{Co}_x\text{O}_{2-\delta}$  ( $x \leq 0.015$ ) samples calcined at 973 K.

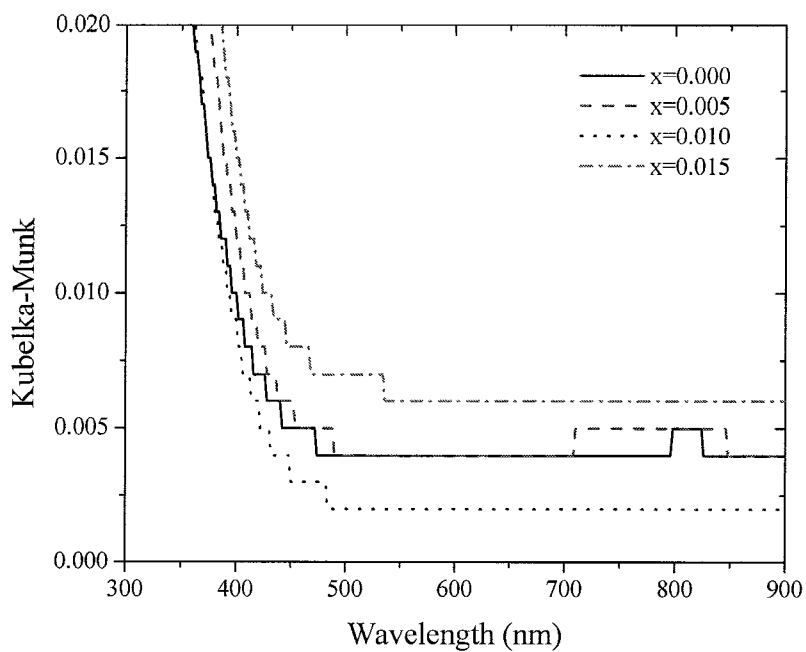


**Figure F.7** The Kubelka-Munk spectra of the  $\text{Sn}_{1-x}\text{Fe}_x\text{O}_{2.\delta}$  ( $x \leq 0.015$ ) samples calcined at 873 K.

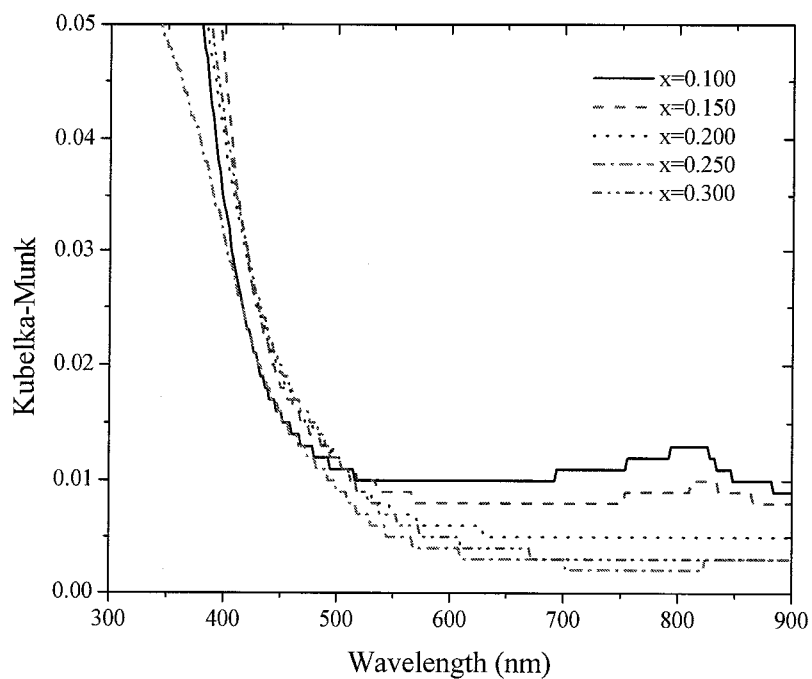


**Figure F.8** The Kubelka-Munk spectra of the  $\text{Sn}_{1-x}\text{Fe}_x\text{O}_{2.\delta}$  ( $0.100 \leq x \leq 0.300$ ) samples calcined at 873 K.

## **APPENDIX G**

### **X-ray Diffractograms of $\text{Sn}_{1-x}\text{TM}_x\text{O}_{2.8}$ from Rietveld Refinement**



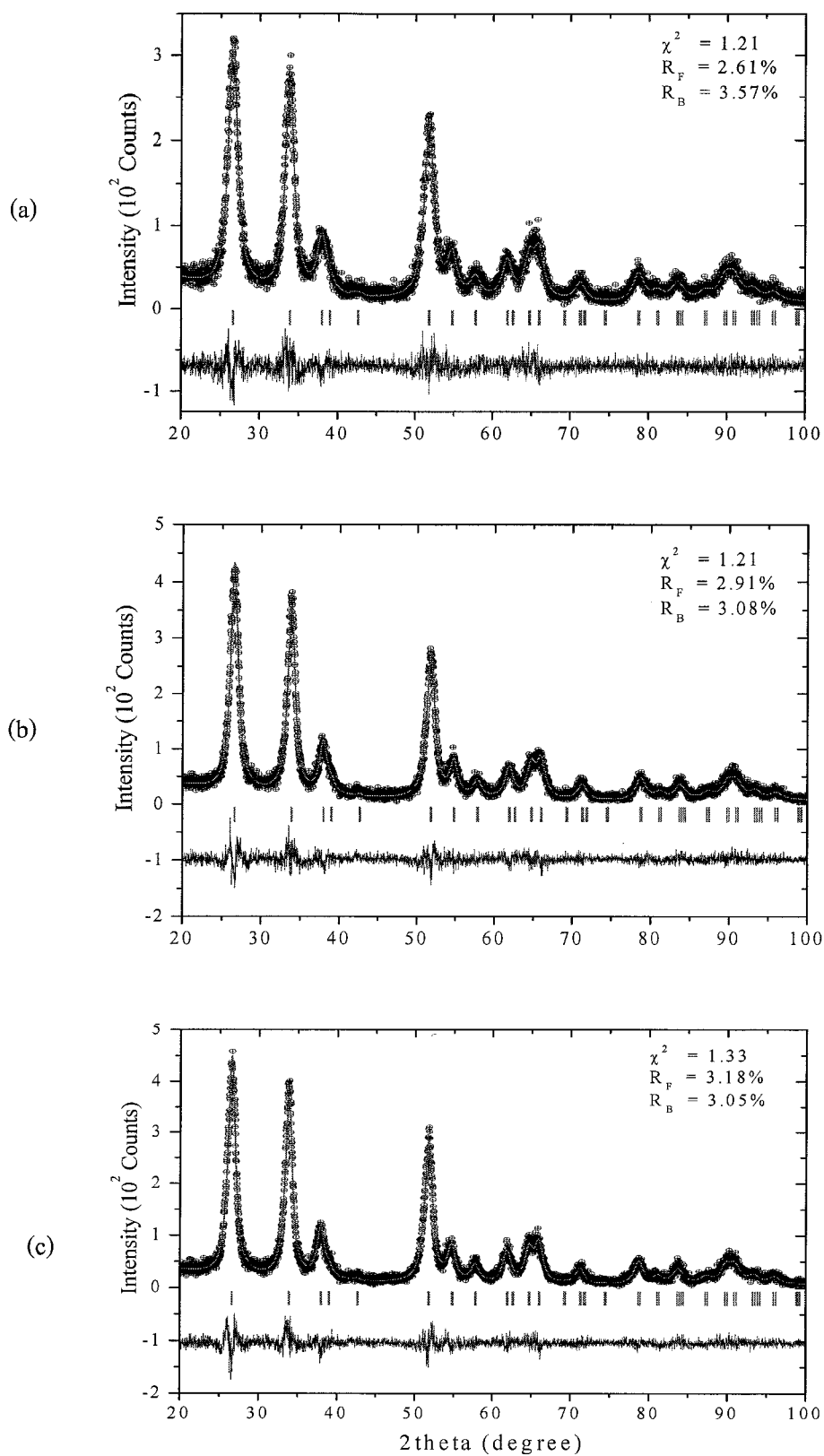


**Figure G.1** X-ray diffractograms of the  $\text{Sn}_{1-x}\text{Cr}_x\text{O}_{2.8}$  samples calcined at 773 K; (a)  $x = 0.005$  (b)  $x = 0.010$  and (c)  $x = 0.015$ .

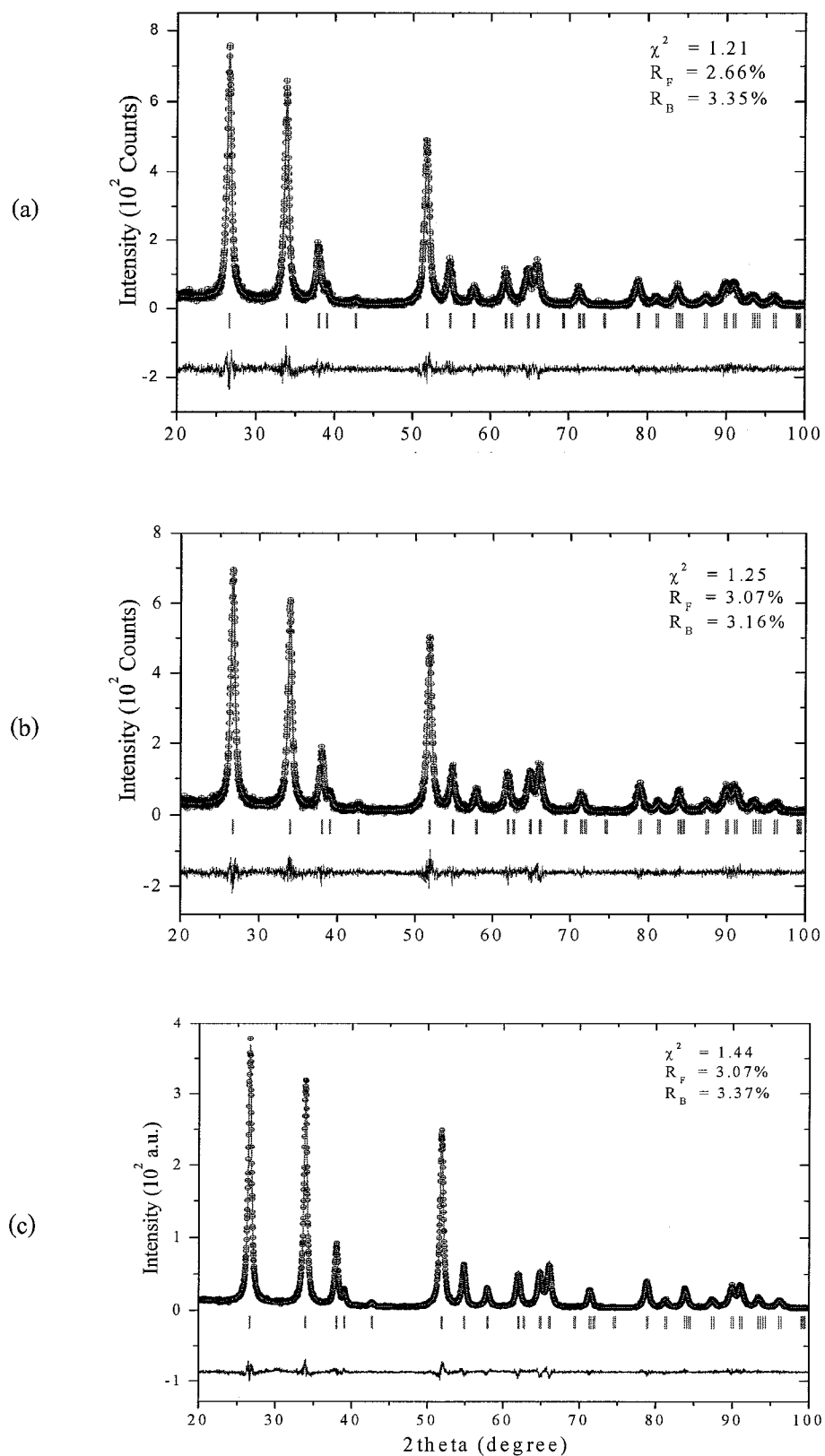


**Figure G.2** X-ray diffractograms of the  $\text{Sn}_{1-x}\text{Cr}_x\text{O}_{2.8}$  samples calcined at 873 K; (a)  $x = 0.005$  (b)  $x = 0.010$  and (c)  $x = 0.015$ .

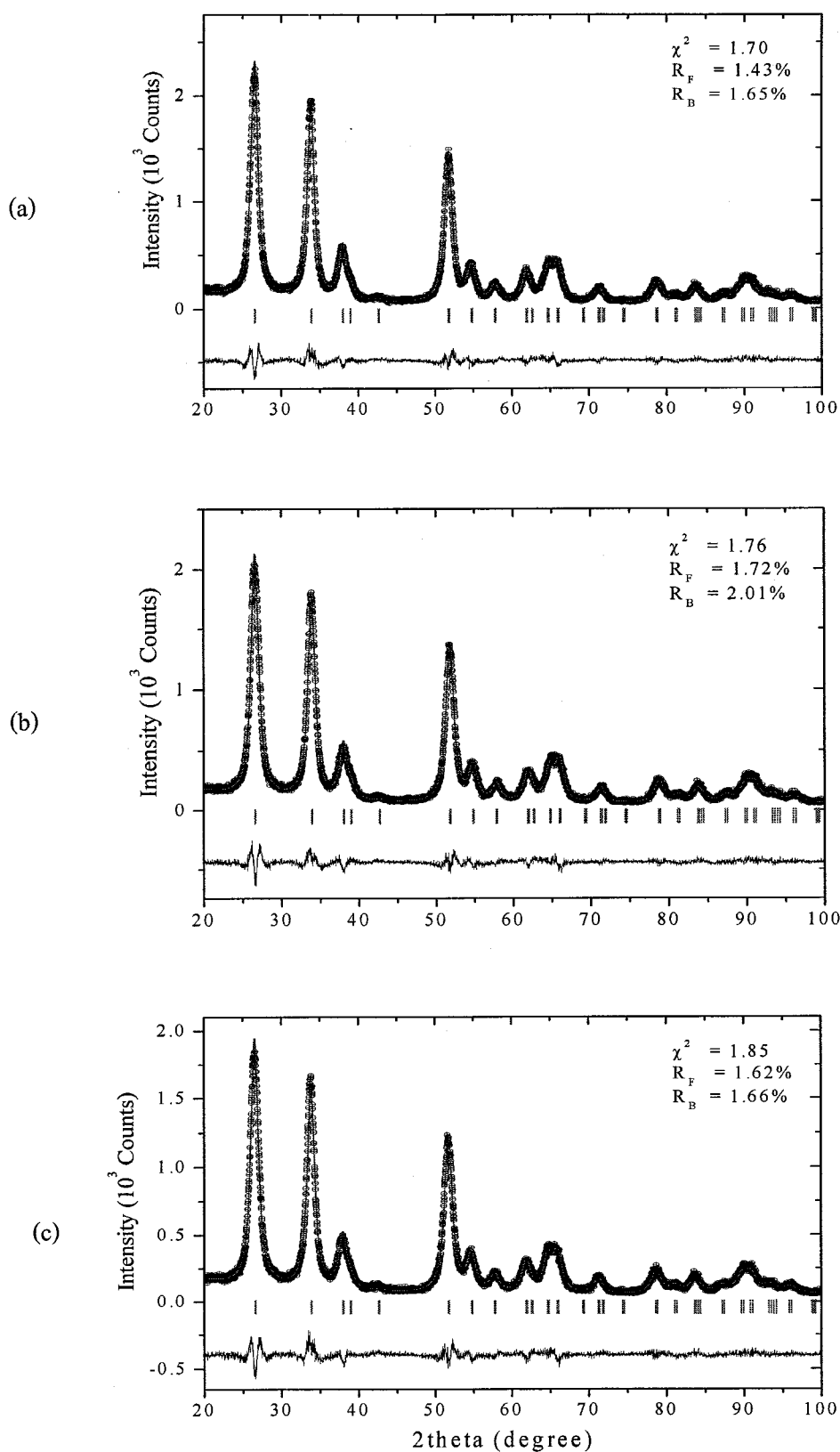


**Figure G.3** X-ray diffractograms of the  $\text{Sn}_{1-x}\text{Co}_x\text{O}_{2.8}$  samples calcined at 773 K; (a)  $x = 0.005$  (b)  $x = 0.010$  and (c)  $x = 0.015$ .

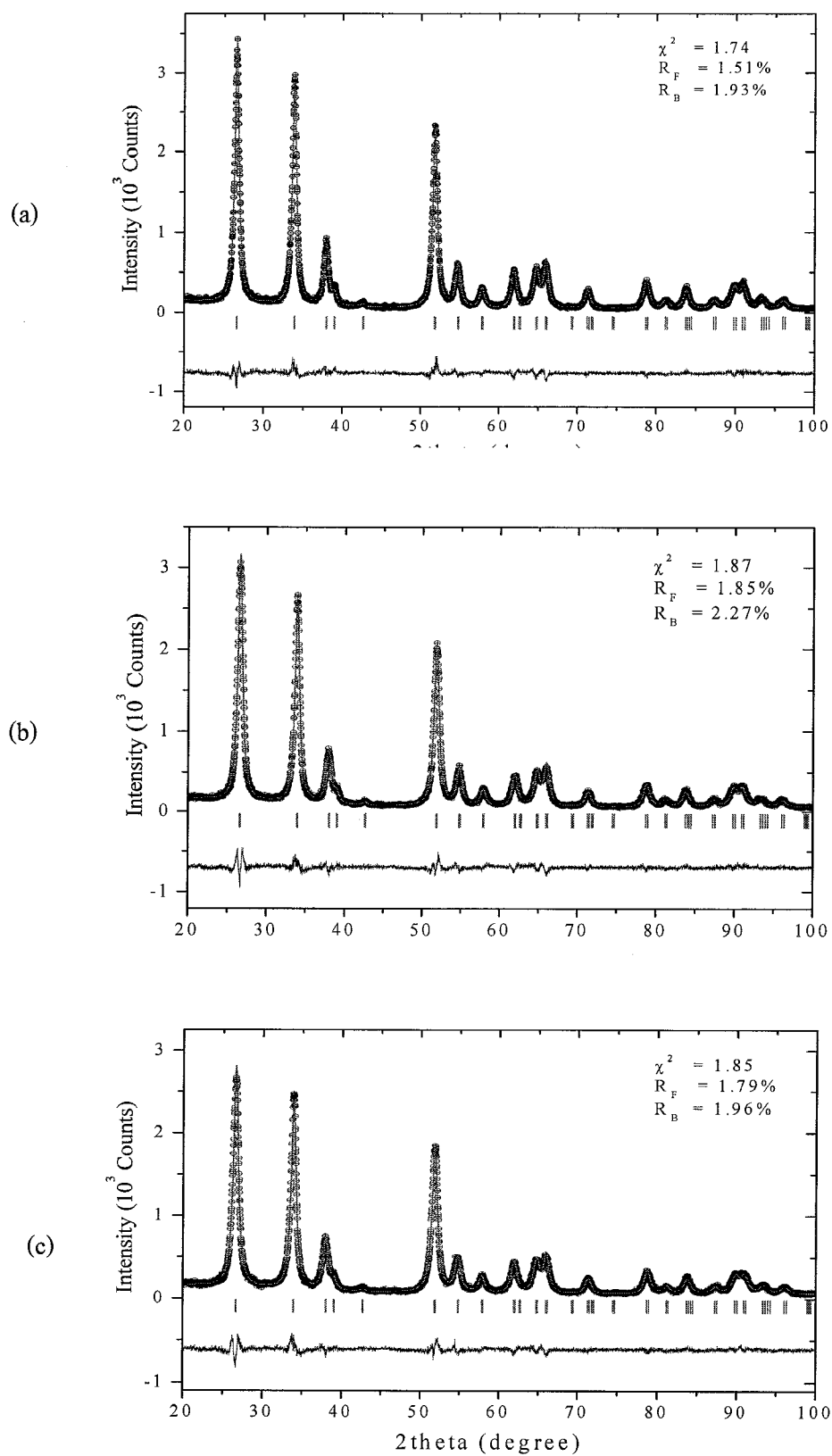


**Figure G.4** X-ray diffractograms of the  $\text{Sn}_{1-x}\text{Co}_x\text{O}_{2.8}$  samples calcined at 873 K; (a)  $x = 0.005$  (b)  $x = 0.010$  and (c)  $x = 0.015$ .

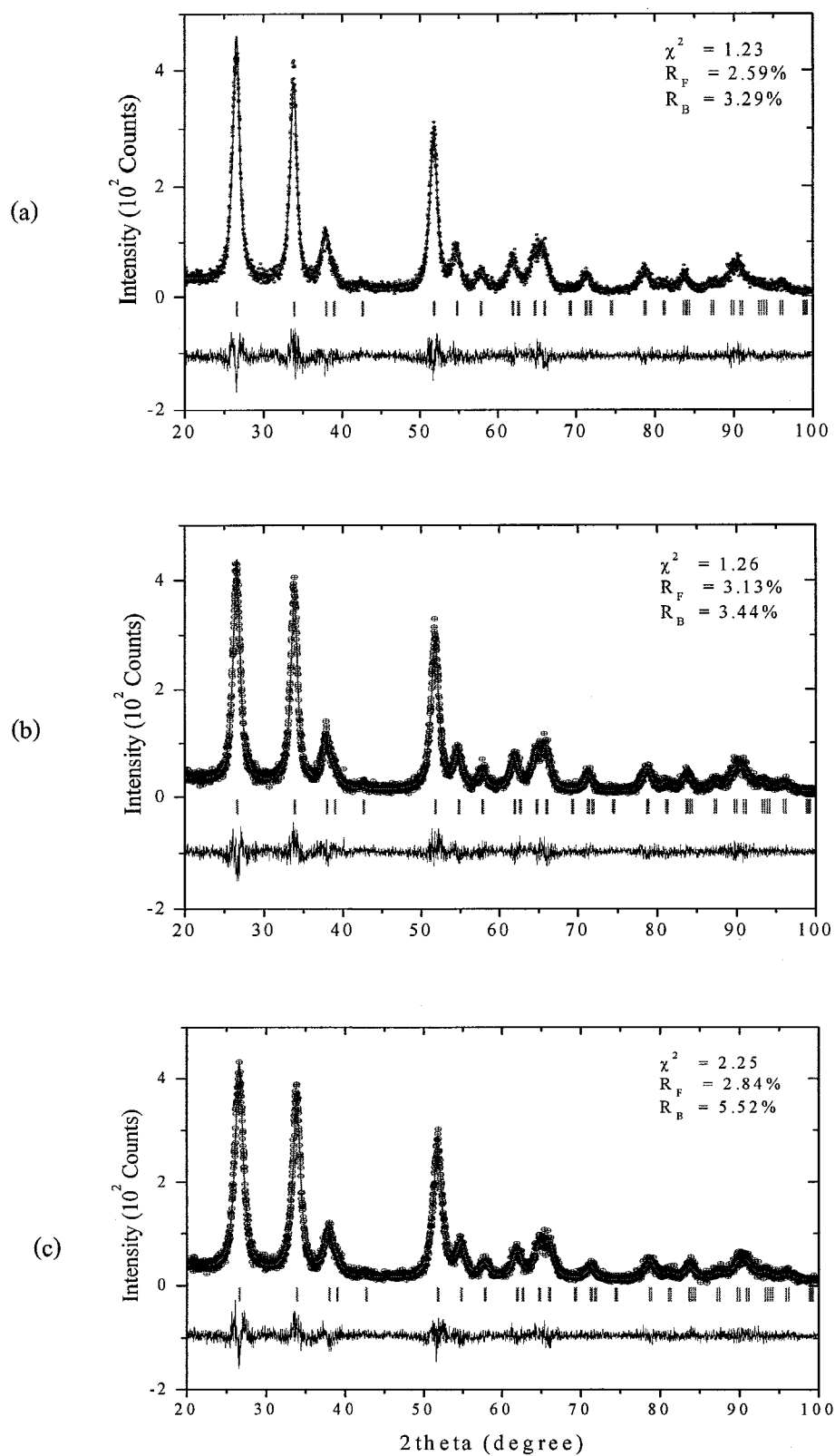


**Figure G.5** X-ray diffractograms of the  $\text{Sn}_{1-x}\text{Fe}_x\text{O}_{2.8}$  samples calcined at 773 K; (a)  $x = 0.005$  (b)  $x = 0.010$  and (c)  $x = 0.015$ .

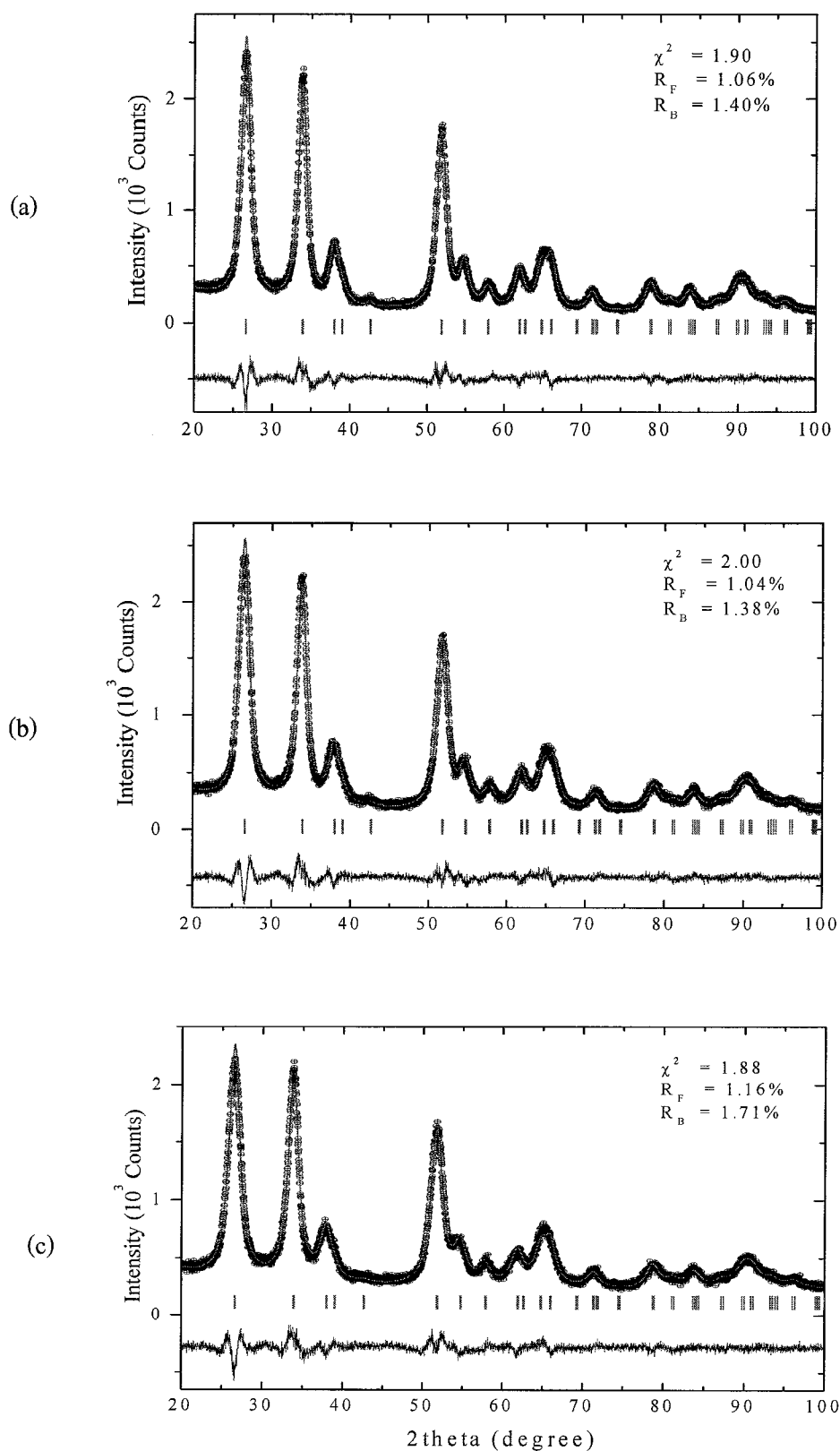


**Figure G.6** X-ray diffractograms of the  $\text{Sn}_{1-x}\text{Fe}_x\text{O}_{2.8}$  samples calcined at 773 K; (a)  $x = 0.100$  (b)  $x = 0.200$  and (c)  $x = 0.300$ .

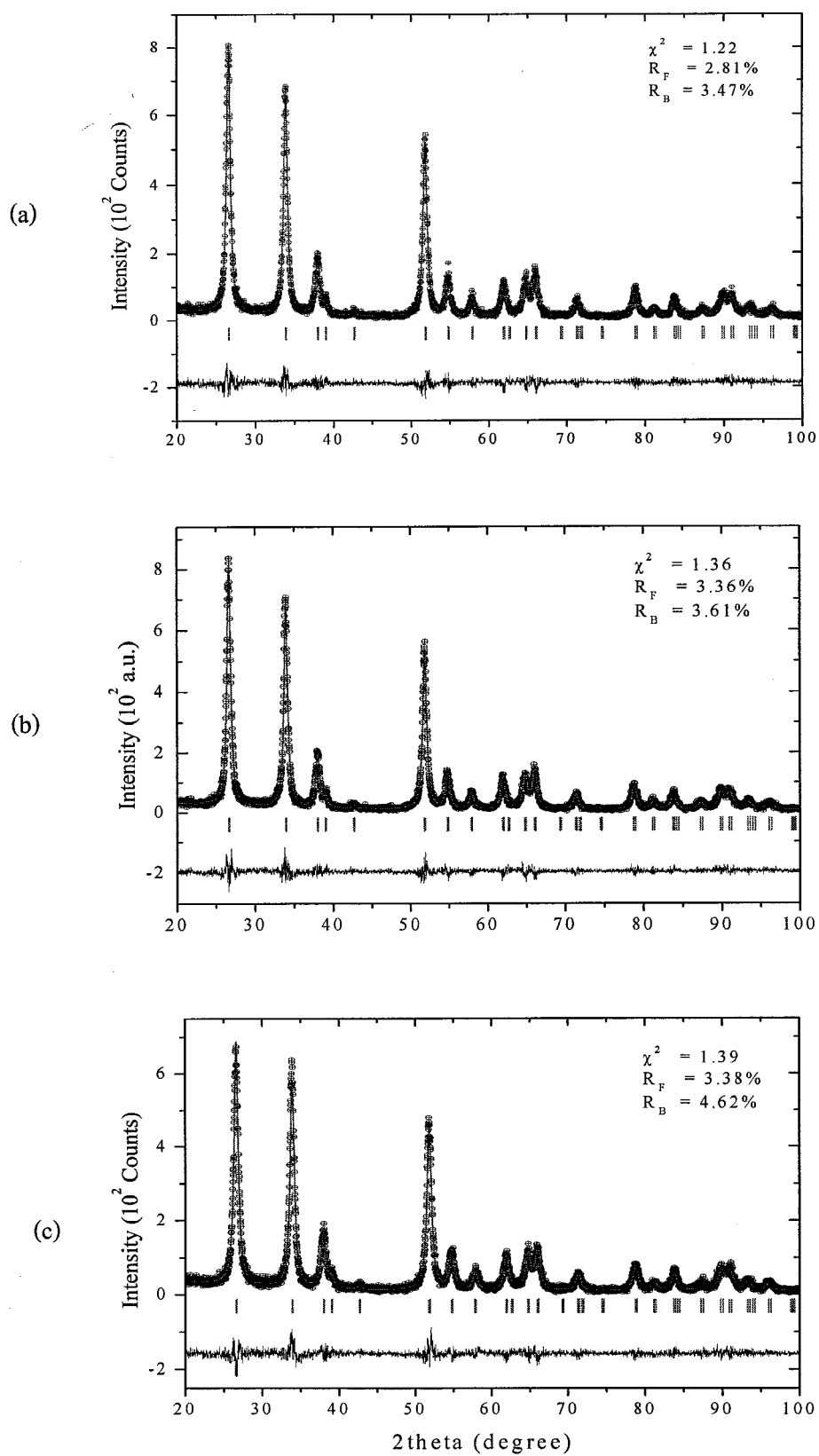


**Figure G.7** X-ray diffractograms of the  $\text{Sn}_{1-x}\text{Fe}_x\text{O}_{2.8}$  samples calcined at 873 K; (a)  $x = 0.005$  (b)  $x = 0.010$  and (c)  $x = 0.015$ .

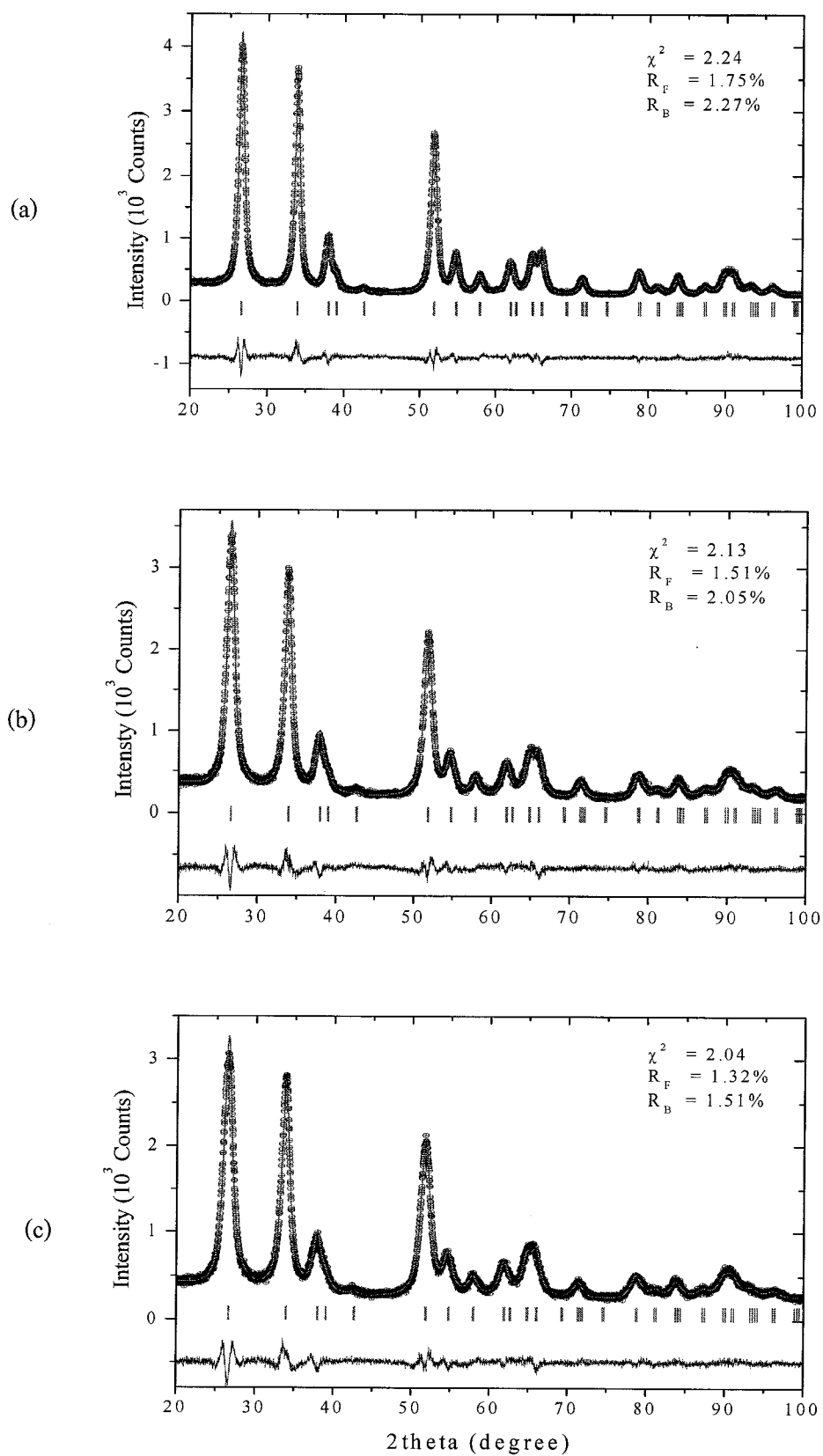


**Figure G.8** X-ray diffractograms of the  $\text{Sn}_{1-x}\text{Fe}_x\text{O}_{2.8}$  samples calcined at 873 K; (a)  $x = 0.100$  (b)  $x = 0.200$  and (c)  $x = 0.300$ .



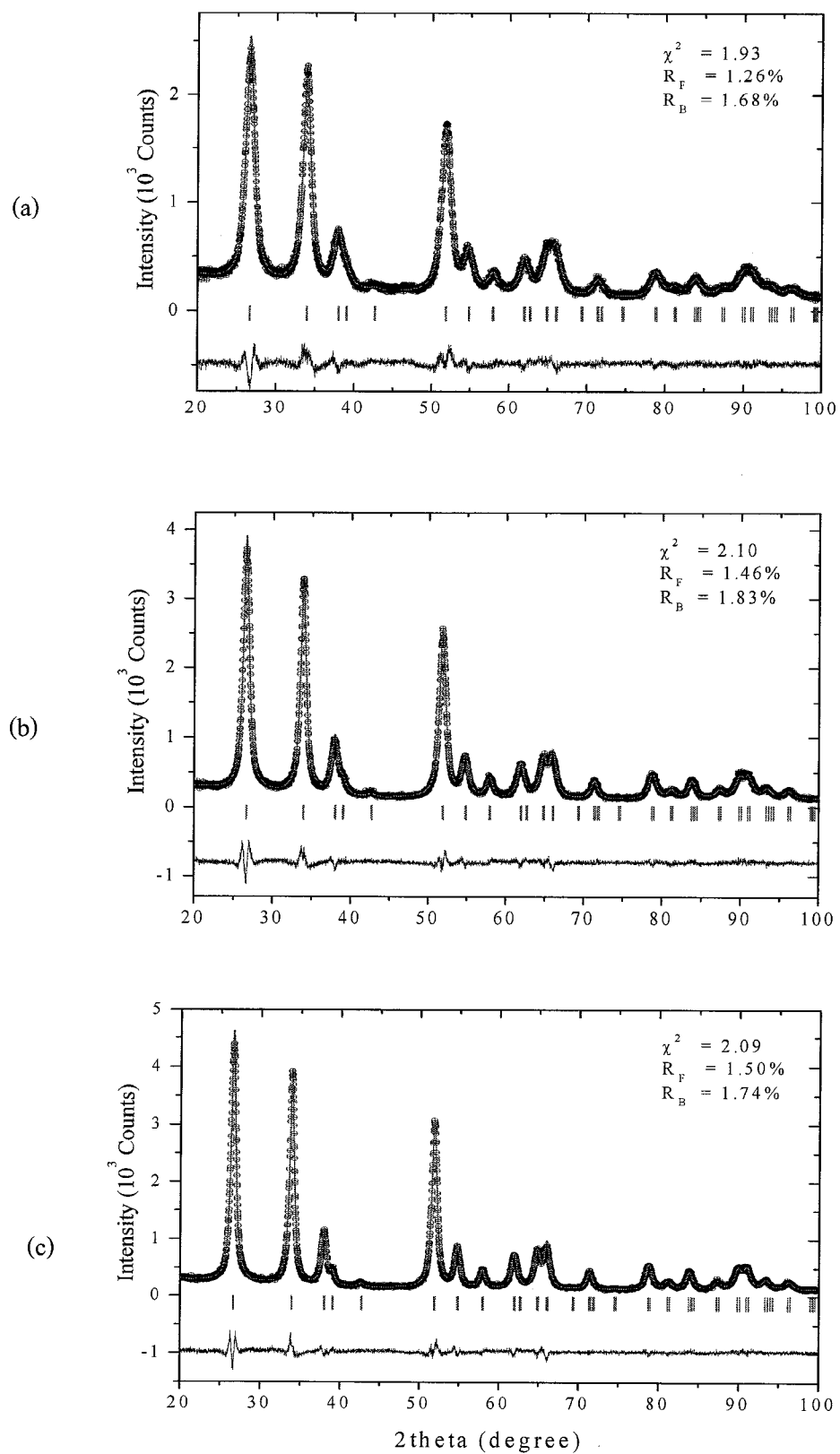


**Figure G.9** X-ray diffractograms of the  $\text{Sn}_{0.850}\text{Fe}_{0.150}\text{O}_{2.8}$  samples calcined at (a) 773 K (b) 873 K and (c) 973 K.

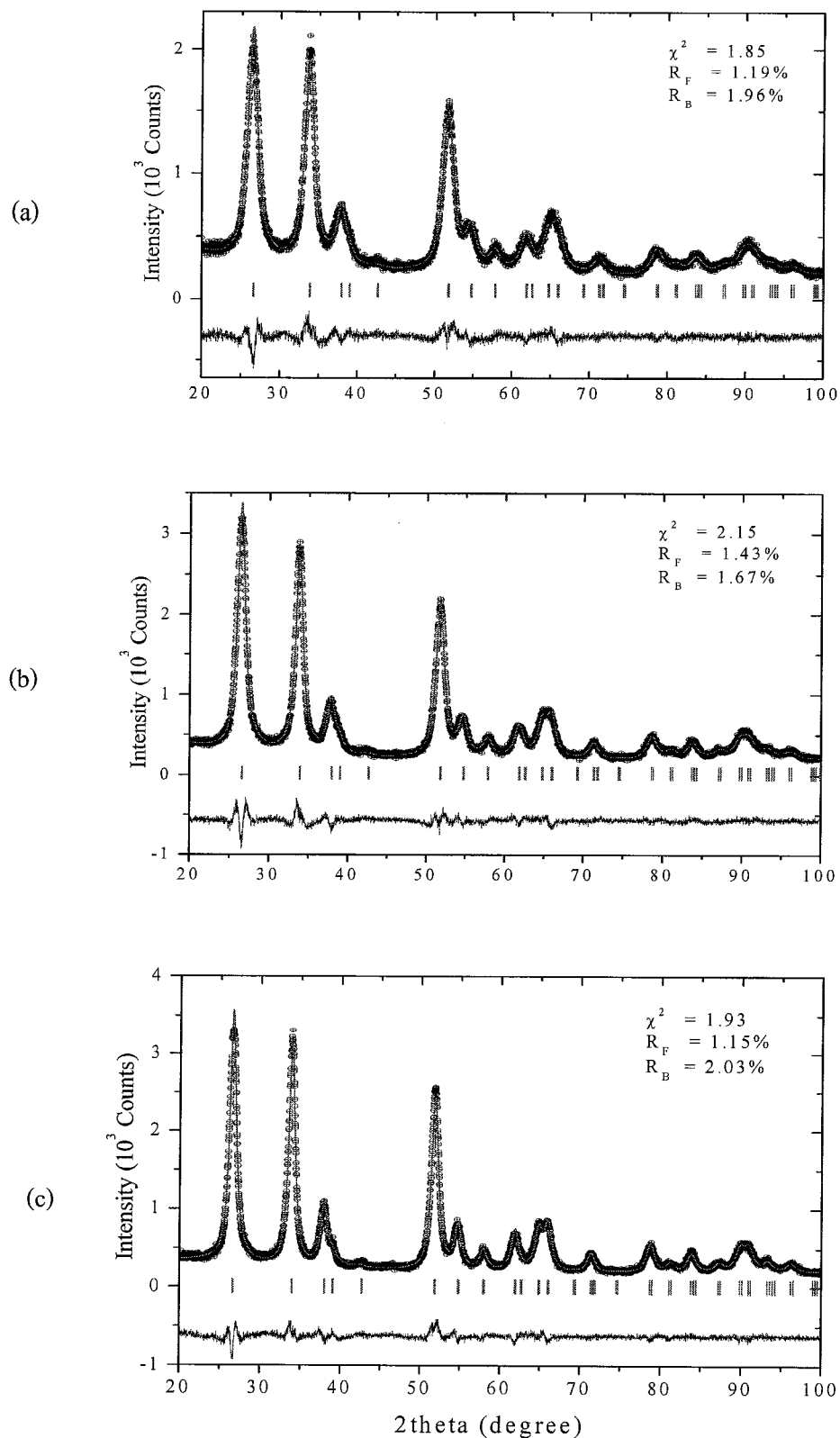


**Figure G.10** X-ray diffractograms of the  $\text{Sn}_{0.750}\text{Fe}_{0.250}\text{O}_{2-\delta}$  samples calcined at (a) 773 K (b) 873 K and (c) 973 K.

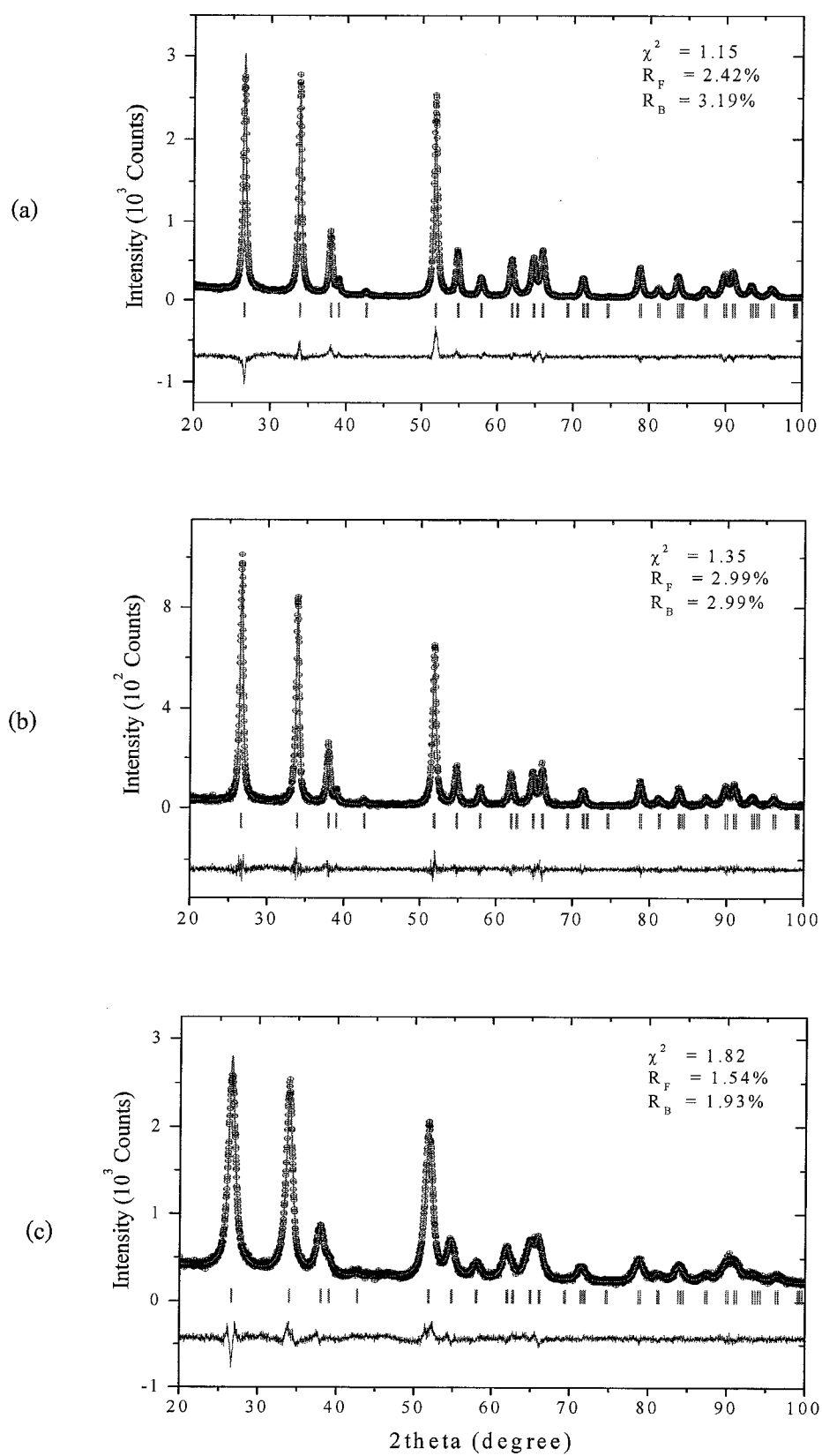


**Figure G.11** X-ray diffractograms of the  $\text{Sn}_{1-x}\text{Cr}_x\text{O}_{2.\delta}$  samples calcined at 973 K; (a)  $x = 0.005$  (b)  $x = 0.015$  and (c)  $x=0.300$ .

**APPENDIX H**  
**Magnetic Data Analysis**

### Magnetic Data Analysis

The SQUID magnetometer yields the magnetization ( $M$ ) in EMU (cgs units). In order to report the magnetization value in  $\mu_B/\text{f.u.}$ , the magnetization was calculated by using the following relationship:

$$M(\text{U}_B / \text{f.u.}) = \frac{M(\text{EMU/g}) \times \text{MW}(\text{g/mol})}{N_A \times n \times 9.30 \times 10^{-21} (\text{EMU}/\mu_B)}$$

where MW is a molecular weight of the compound.  $N_A$  is Avogadro constant ( $6.022 \times 10^{23} \text{ mol}^{-1}$ ) and  $n$  is a number of magnetic atom in the compound.

## **APPENDIX I**

**The Full Width at Half Maximum (FWHM) of the XRD Plane (110)**

**Table I.1** The Full Width at Half Maximum (FWHM) of the XRD plane (110) of  $\text{Sn}_{1-x}\text{TM}_x\text{O}_{2-\delta}$ .

| TM                 | X     | FWHM (degree) |        |        |
|--------------------|-------|---------------|--------|--------|
|                    |       | 773 K         | 873 K  | 973 K  |
| ( $\text{SnO}_2$ ) | 0.000 | 0.9252        | 0.7846 | 0.6904 |
| Co                 | 0.005 | 1.5353        | 0.9324 | 0.7308 |
|                    | 0.010 | 1.6379        | 1.0593 | 0.8424 |
|                    | 0.015 | 1.6418        | 1.0959 | 0.8717 |
| Cr                 | 0.005 | 1.6895        | 0.935  | 0.6361 |
|                    | 0.010 | 1.6185        | 0.8754 | 0.6511 |
|                    | 0.015 | 1.5695        | 0.9491 | 0.6904 |
| Fe                 | 0.005 | 1.5172        | 0.8517 | 0.6595 |
|                    | 0.010 | 1.4742        | 0.8379 | 0.6416 |
|                    | 0.015 | 1.6876        | 0.9508 | 0.6791 |
| Fe                 | 0.100 | 1.7893        | 1.1901 | 0.8958 |
|                    | 0.150 | 1.8171        | 1.2643 | 0.9987 |
|                    | 0.200 | 1.969         | 1.5205 | 1.2019 |
|                    | 0.250 | 1.9614        | 1.6152 | 1.2914 |
|                    | 0.300 | 2.0808        | 1.7316 | 1.3229 |

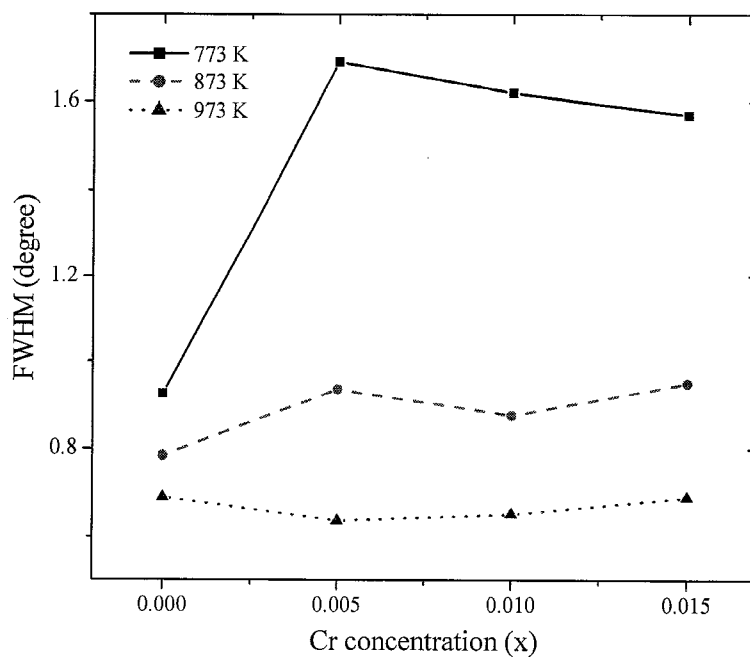


**Figure I.1** FWHM of the plane (110) of the  $\text{Sn}_{1-x}\text{Cr}_x\text{O}_{2-\delta}$  ( $x \leq 0.015$ ) samples calcined at 773, 873 and 973 K.

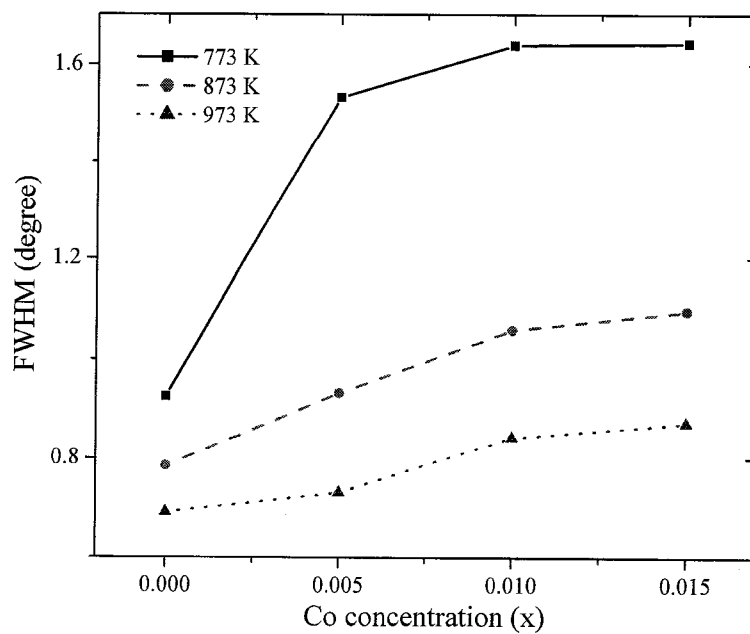


**Figure I.2** FWHM of the plane (110) of the  $\text{Sn}_{1-x}\text{Co}_x\text{O}_{2-\delta}$  ( $x \leq 0.015$ ) samples calcined at 773, 873 and 973 K.



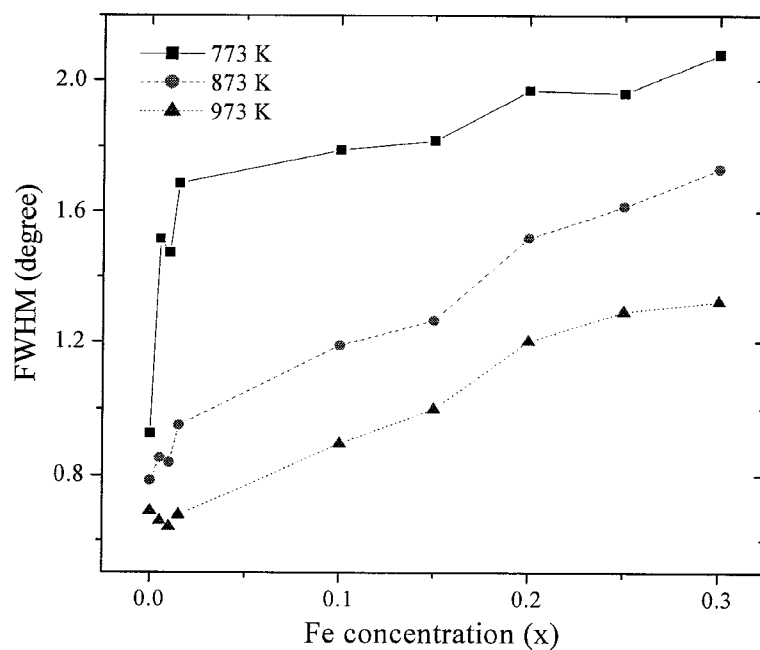


**Figure I.3** FWHM of the plane (110) of the  $\text{Sn}_{1-x}\text{Fe}_x\text{O}_{2.8}$  ( $x \leq 0.300$ ) samples calcined at 773, 873 and 973 K.

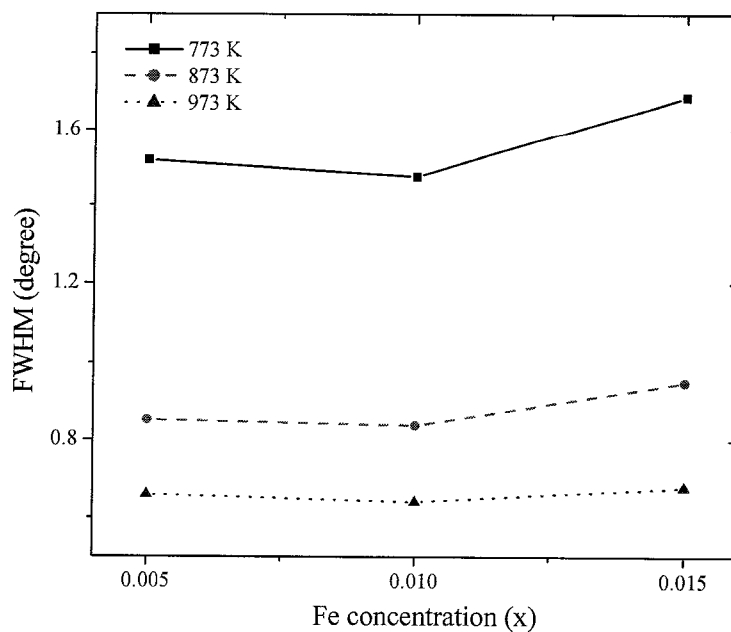


**Figure I.4** FWHM of the plane (110) of the  $\text{Sn}_{1-x}\text{Fe}_x\text{O}_{2.8}$  ( $x \leq 0.015$ ) samples calcined at 773, 873 and 973 K.